

Interfacial thermal resistance: Past, present, and future

Jie Chen^{✉*} and Xiangfan Xu^{†‡}


Center for Phononics and Thermal Energy Science, China–EU Joint Lab for Nanophononics, MOE Key Laboratory of Advanced Micro-structured Materials, School of Physics Science and Engineering, Tongji University, Shanghai 200092, China

Jun Zhou^{‡§}

Phonon Engineering Research Center of Jiangsu Province, Center for Quantum Transport and Thermal Energy Science, Institute of Physics Frontiers and Interdisciplinary Sciences, School of Physics and Technology, Nanjing Normal University, Nanjing 210023, China

Baowen Li[§]

Department of Material Science and Engineering, Department of Physics, Shenzhen Institute for Quantum Science and Engineering, Southern University of Science and Technology, Shenzhen 518055, China and Paul M. Rady Department of Mechanical Engineering and Department of Physics, University of Colorado, Boulder, Colorado 80305-0427, USA

 (published 22 April 2022)

Interfacial thermal resistance (ITR) is the main obstacle for heat flows from one material to another. Understanding ITR becomes essential for the removal of redundant heat from fast and powerful electronic and photonic devices, batteries, etc. In this review, a comprehensive examination of ITR is conducted. Particular focus is placed on the theoretical, computational, and experimental developments in the 30 years after the last review given by Swartz and Pohl in 1989. To be self-consistent, the fundamental theories, such as the acoustic mismatch model, the diffuse mismatch model, and the two-temperature model, are reviewed. The most popular computational methods, including lattice dynamics, molecular dynamics, the Green's function method, and the Boltzmann transport equation method, are discussed in detail. Various experimental tools in probing ITR, such as the time-domain thermoreflectance, the thermal bridge method, the 3ω method, and the electron-beam self-heating method, are illustrated. This review covers ITR (also known as the thermal boundary resistance or Kapitza resistance) of solid-solid, solid-liquid, and solid-gas interfaces. Such fundamental challenges as how to define the interface, temperature, etc. when the materials scale down to the nanoscale or atomic scale and the opportunities for future studies are also pointed out.

DOI: [10.1103/RevModPhys.94.025002](https://doi.org/10.1103/RevModPhys.94.025002)

CONTENTS

I. Introduction	2	c. Molecular dynamics simulation	9
II. Theories and Experimental Methods	3	d. The Boltzmann transport equation and the Monte Carlo method	12
A. Problem formulation	3	e. Other models for phonon transport	12
1. Interfacial thermal resistance	3	C. Impacts of other energy carriers	12
2. Definition of the interface region and its nearby temperature	4	D. Experimental tools	14
B. Phonon picture of interfacial thermal transport	5	1. Pump-probe thermoreflectance technique	14
1. Continuum theory	6	2. Electron-beam self-heating method	16
a. Acoustic mismatch model	6	3. Other methods	18
b. Diffuse mismatch model	6	a. 3ω method	18
2. Atomistic theory	7	b. Traditional heater-sensor method	18
a. Lattice dynamics	7	E. Summary of methods	18
b. Green's function approach	8	III. Solid-Solid Interfaces	19
		A. Phonon transport across various interfaces	19
		1. Comparison of theoretical approaches	19
		2. Validation of AMM and DMM	20
		3. Lattice mismatch	21
		4. Interfacial coupling strength	22
		5. Roughness and disorder	24
		6. Summary	25

*jie@tongji.edu.cn

†xuxiangfan@tongji.edu.cn

‡zhoujunzhou@njnu.edu.cn

§libw@sustech.edu.cn

B. Electron-phonon coupling across the metal-dielectric interface	26
1. Indirect electron-phonon coupling channel	26
2. Direct electron-phonon coupling channel	27
C. Electron contribution across the metal-metal interface	27
D. ITR for low-dimensional structures	28
1. Multilayers and superlattice	28
2. Sandwich structures with 2D or quasi-2D materials	29
3. Interfaces with nanoscale contact	30
IV. Solid-Liquid Interfaces	31
A. Solid-helium interface at cryogenic temperatures	31
1. Solid-liquid ⁴ He interface	31
2. Solid-liquid ³ He interface	32
3. Solid-liquid ³ He- ⁴ He mixture interface	33
4. Critical phenomenon	33
B. Solid-classical liquid interface at noncryogenic temperature	33
1. Interfacial bonding strength	34
2. Surface functionalization	35
3. Nanoparticle-liquid interface	37
V. Solid-Gas Interfaces	38
A. Thermal accommodation coefficient	38
B. Nanoparticle-gas interface	41
VI. Summary and Challenges	41
Acknowledgments	42
References	42

I. INTRODUCTION

When two materials with different temperatures are put into contact, heat will flow from the high-temperature one to low-temperature one. This phenomenon seems simple but is far more complicated than we thought. There are many interesting fundamental questions to be understood both from a physicist's point of view, such as how the heat carriers (phonons, electrons, etc.) are transported across the interface (boundary) between these two materials, and from an engineering application point of view, such as how to efficiently remove heat from micro-electric devices, batteries, quantum devices, etc.

This problem has attracted the attention of scientists for centuries. The first recorded discussion was from [Fourier \(1822\)](#) in the early 19th century. Fourier recognized that the quantity of heat that the solid bodies lose to their surrounding gas through the surface obeys the same principle. He used the term “external conducibility” to characterize the quantity of heat through surface per unit time per unit area per unit temperature drop. This definition is exactly the same as the modern term interfacial thermal conductance (ITC). Later [Poisson \(1835\)](#) started his study with the following continuity of the heat flux at the interface:

$$J = \kappa_1 |\nabla T|_1 = \kappa_2 |\nabla T|_2 = h_I \Delta T. \quad (1)$$

In Eq. (1) the heat flux is defined as the energy transported per unit time across unit area $J = \dot{Q}/A$, where \dot{Q} is the heat current and A is the interfacial cross-section area. κ_1 and κ_2 are the thermal conductivities of materials 1 and 2, respectively. $|\nabla T|_{1,2}$ are the moduli of the temperature gradient in materials 1 and 2 evaluated at the interface, respectively. ΔT is the temperature

jump at the interface. Thus, one can define the ITC h_I , or equivalently the interfacial thermal resistance (ITR) R_I , as

$$R_I = \frac{1}{h_I} = \frac{\Delta T}{J}. \quad (2)$$

[Poisson](#) proposed using the following coefficient as a measure of the temperature jump:

$$L_{\text{Poisson}} = \Delta T / |\nabla T|_1 = \kappa_1 / h_I, \quad (3)$$

which is widely known as the Kapitza length in modern terminology. [Smoluchowski \(1898\)](#) was the first to study both experimentally and theoretically the heat transfer through the interface between a solid and a gas. The measured values of L_{Poisson} for the glass-air interface and the glass-hydrogen interface were of the order of micrometers at a pressure of 1 atm. Correspondingly, the calculated thermal resistance can be as large as 10^{-6} – 10^{-5} m²KW⁻¹. The results can be explained using a previous theory given by [Maxwell \(1879\)](#). He assumed that a portion of gas molecules incident to the interface were in thermal equilibrium with the solid surface due to diffusive scatterings and that the rest of the molecules were scattered specularly.

The study on heat transfer through the interface between solid and liquid started as early as 1936 ([Kürti, Rollin, and Simon](#)), but it was ignored by assuming a small thermal resistance. [Keesom and Keesom \(1936\)](#) recognized that the thermal resistance at the interface was relatively considerable, but again the phenomenon was not further studied. [Kapitza \(1941\)](#) reported his measurements of the temperature drop near the boundary between liquid helium and a solid when heat flows across the boundary. More than ten years later, [Khalatnikov \(1952\)](#) and [Mazo \(1955\)](#) presented a theoretical model, an approximation to what is now known as the acoustic mismatch model (AMM), to explain that experiment. This theory was later extended to the solid-solid interface by [Little \(1959\)](#).

Since the discovery of ITR for solid-liquid helium interfaces in 1941, also known as the Kapitza resistance, the scope of research has been expanded to many other interfaces between dissimilar materials. In the past half century, there have been two comprehensive reviews published in *Reviews of Modern Physics* on ITR: one by [Pollack \(1969\)](#) and another by [Swartz and Pohl \(1989\)](#).

[Pollack \(1969\)](#) focused mainly on the Kapitza resistance, namely, the ITR between solid and liquid (mainly helium), at cryogenic temperatures. In the paper, he also discussed the AMM in detail.

20 years later, [Swartz and Pohl \(1989\)](#) published another review. Their paper reviewed the ITR on both the solid-solid interface (called the thermal boundary resistance) and the solid-liquid interface (called the Kapitza resistance). They also discussed in detail two popular theories: AMM and the diffuse mismatch model (DMM). The main message of this review is that solid-solid ITR can be explained by AMM or DMM only when $T < 30$ K. Otherwise, these two theories always deviate significantly from experimental works.

More than 30 years have passed since the review of [Swartz and Pohl \(1989\)](#). The study of ITR has been significantly extended and broadened. In particular, the research focus has

been shifted because of the fast development of semiconductor and energy industries, particularly the miniaturization of microelectronics and the emergence of nanotechnology. The faster and more powerful microelectronic devices have made the study of ITR much more relevant and urgent. There are two levels of problems regarding ITR. On the one hand, the device itself is made of many layers of materials, including semiconductors, metals, and dielectric materials. There are a large number of interfaces inside the device. On the other hand, packaging of the electronic device consists of die attach, thermal interfacial materials, and a heat spreader or sink, which form at least three different interfaces. One key point in designing these layered structures is to guarantee that the heat generated by the billions of transistors can be dissipated away efficiently so as to avoid a breakdown or a heat death. The heat dissipation problem becomes even more serious when the chip maker moves from two-dimensional (2D) to three-dimensional (3D) architecture chips (Waldrop, 2016).

With the semiconductor technology percolating to other applications, the ITR problem has been encountered in many new fields and devices, such as light emitting diodes, quantum cascade lasers, phase change memory, thermoelectric devices, wearable devices, and photovoltaic cells.

Last, the ITR plays a crucial role in the heat dissipation of batteries (Hao *et al.*, 2018; Zhu *et al.*, 2019; Feng *et al.*, 2020). The inefficient removal of heat from batteries used in smartphones and electric vehicles will not only affect the performance and reliability but also in the worst case induce a fire that could totally destroy the device and cause disastrous consequences.

Much important progress has been achieved in the last 30 years, particularly in the following areas:

- (1) On the theoretical area, in addition to the further development of AMM and DMM, there are other methods such as the two-temperature model (TTM) in which both electrons and phonons are considered.
- (2) The emergence of computational simulations. With the development of fast and powerful computers, people can perform computer simulations on the process of heat flow through the interface not only at the nanoscale level but also at the atomic level. There have been many powerful computational methods developed in this field, such as lattice dynamics (LD), molecular dynamics (MD), the Boltzmann transport equation, and the Green's function method.
- (3) More experimental tools have been developed, such as the time-domain thermoreflectance (TDTR) method, the 3ω method, the thermal bridge method, and the electron-beam (e -beam) self-heating method. In particular, the invention of the e -beam method is capable of spatially detecting thermal resistance down to 20 nm (Wang *et al.*, 2011; Liu *et al.*, 2014; Aiyiti, Bai *et al.*, 2018).
- (4) There are many novel phenomena discovered in ITR. Among many others, the discovery of asymmetric ITR is one of the most exciting (Li, Lan, and Wang, 2005). This discovery has led to the fast developing research field "thermal rectification," which is an active field in heat transfer (Li *et al.*, 2012; Wehmeyer *et al.*, 2017).
- (5) There are more data available for various interfaces, particularly the emergence of low-dimensional

materials in the past two or three decades, which has expanded the scope of research of interfacial thermal transfer.

- (6) Temperature ranges have expanded from cryogenic temperatures to much higher temperatures, including room temperature, for most of the applications of powerful electronic devices, batteries, and thermoelectric devices.

These new developments not only make a more comprehensive review highly expected and necessary but also raise a lot of new questions. In particular, when the system scales down to the nanoscale or even the atomic scale, there are three questions of primary importance to address: (i) What is the heat? (ii) What is the temperature? (iii) What is the interface? More specifically, how can one define the boundary or interface? How thick or thin is the interface? What does the temperature on the interface indicate? If the interface is only at the atomic scale or the nanoscale, then how does one define the temperature in such a small system? How does one measure the temperature at that scale? If the temperature indeed can be defined and measured, then are the temperatures on both sides of the interface the same?

There are already many reviews emphasizing different aspects of ITR study, such as the work of Monachon, Weber, and Dames (2016) on materials, that of Bezuglyj and Shklovskij (2016) on electrons' contribution, the work of Kosevich, Syrkin, and Kosevich (1997) on surface vibrational modes, that of Zhou and Zhang (2018) on different theories, and the work of Hopkins (2013) and Giri and Hopkins (2020) on solid-solid interfaces. In addition, Cahill *et al.* (2003, 2014) presented some major findings on nanoscale thermal transport.

Our review pays attention not only to the development of the theories, simulation tools, and measurement techniques but also to the underlying physics. This review is a road map for future investigations of ITR. The review gives readers a comprehensive picture of this fast developing field. It also points out future challenges in the coming years.

The review is arranged as follows: In Sec. II, we focus on the existing theories and tools for studying ITR, including various simulation methods and measurement techniques. In Secs. III, IV, and V, we review the recent advances in ITR of various kinds of interfaces, including solid-solid, solid-liquid, and solid-gas interfaces, respectively. All new phenomena or interest related to these interfaces is also highlighted in the corresponding section. Finally, in Sec. VI, we discuss upcoming challenges and point out future directions for the study of ITR.

II. THEORIES AND EXPERIMENTAL METHODS

In this section, we review the theoretical models, the simulation tools, and the experimental measurement techniques.

A. Problem formulation

1. Interfacial thermal resistance

The ITC defined by Eq. (2) has the unit $\text{W m}^{-2} \text{K}^{-1}$, which is similar to the unit of thermal conductivity $\text{W m}^{-1} \text{K}^{-1}$. The only difference is the unit length, which is not involved in

Eq. (2), as the interface is assumed to be planar. To bridge the gap, a relevant concept known as the Kapitza length is defined as

$$L_K = R_I \kappa, \quad (4)$$

where κ is the thermal conductivity of a given material. L_K measures the thickness of a given material that has the equivalent thermal resistance. This definition is the same as the Poisson coefficient L_{Poisson} defined in Eq. (3).

For macroscopic interfaces, h_I and R_I are geometry independent and do not change when the area of interface A changes. However, this is questionable when one measures h_I with the nanoscale contacting area. For instance, when two carbon nanotubes are in contact with each other, h_I is found to be strongly dependent on the contact area (Yang *et al.*, 2010). The vibrational modes are significantly affected by the geometry. At low temperatures, even the universal quantum thermal conductance due to quantum confinement can be observed (Schwab *et al.*, 2000). Therefore, for nanoscale interfacial thermal transport, h_I strongly depends on the contact area and the geometry near the interface.

2. Definition of the interface region and its nearby temperature

Interfacial atoms differ from bulk atoms in the sense that the local environment (e.g., the interatomic interaction and lattice structure) at the interface differs from that of the bulk region. In real situations, the interface formed by dissimilar materials may not be a sharp plane, as depicted in Fig. 1, due to the lattice mismatch or the dislocation of atoms. As a result, the interface must be extended to a finite region. As shown in Fig. 2, we consider here that an ideal interface plane at $z = 0$ extends to a finite thickness δ_1 and δ_2 on each side, respectively.

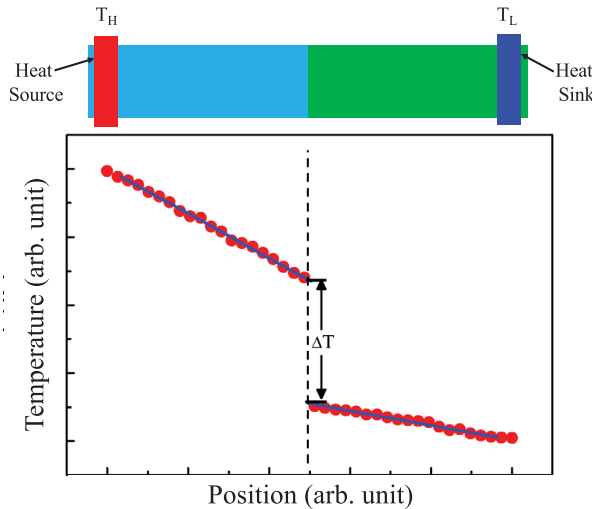


FIG. 1. Schematic diagram and temperature profile for an interface composed of two dissimilar segments. The red and blue boxes at the two ends denote the high-temperature heat source T_H and the low-temperature heat sink T_L , respectively. The dashed line in the temperature profile pinpoints the position of the interface, where an abrupt temperature discontinuity ΔT is observed.

Temperature is an equilibrium concept that characterizes a macroscopic system in thermal equilibrium. For phonons, the equilibrium distribution follows the Bose-Einstein distribution. The concept of temperature can also be extended to a nonequilibrium situation under the assumption of local thermal equilibrium. In this case, a local temperature can be defined within a certain region.

A proper definition of the interface region should consider the following two contradicting aspects. From the statistical physics point of view, the local region should be sufficiently large in order to reach local thermal equilibrium. For homogeneous systems, the phonon distribution is changed by anharmonic phonon-phonon scatterings, so the size of the local region should be larger than the phonon mean free path (MFP). Since the phonon MFP is mode dependent, one plausible way is to define an averaged MFP known as the Casimir limit (Casimir, 1938). In the case of an interface, however, the boundary may provide natural limits to the size of the local region, which also depends on the specific kind of interface. A more detailed discussion of this point can be found elsewhere (Cahill *et al.*, 2003). In atomic level simulations, the local temperature is in practice defined using the ensemble-averaged kinetic energy, which we discuss further in Sec. II.B.2.c.

On the other hand, as shown in Fig. 2, the total thermal resistance between slab 1 and slab 2 can be expressed as $\delta_1/\kappa_1 + \delta_2/\kappa_2 + R_I$, where κ_i is the thermal conductivity of material i . In principle, the choice of δ_i should be sufficiently small to ensure that $\delta_i/\kappa_i \ll R_I$. It is more important that δ_i must be less than the MFP l of the corresponding bulk materials, in order to avoid the influence of phonon scatterings from the bulk atoms.

At low temperatures, the typical value of the phonon MFP is approximately micrometers and the typical value of R_I is much larger than $10^{-6} \text{ m}^2 \text{ KW}^{-1}$. It is reasonable to choose δ_i to be of the order of micrometers; in other words, $\delta_i \approx l$. The situation is completely different at high temperatures. For example, the lowest measured value of R_I for Al/sapphire interface at 300 K is $3 \times 10^{-9} \text{ m}^2 \text{ KW}^{-1}$, as reported by Cheng *et al.* (2020). Meanwhile, the value of MFP in sapphire

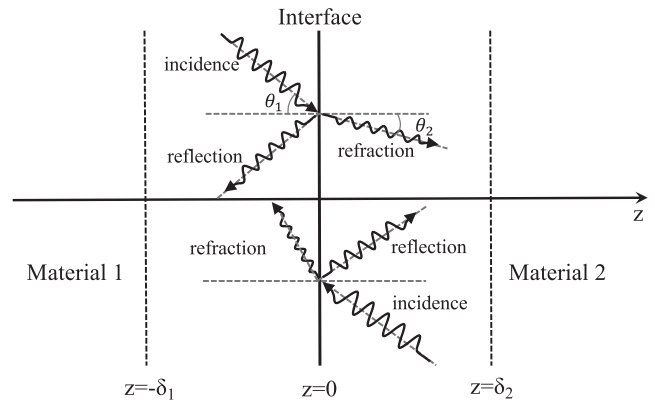


FIG. 2. Phonon reflection and refraction at an ideal interface. Vicinal slab 1 is located at $-\delta_1 < z < 0$ in material 1 and vicinal slab 2 is located at $0 < z < \delta_2$. The normal direction is along the z axis. θ_1 and θ_2 denote the incident angle and refracted angle on each side, respectively.

is between several nanometers and several hundreds of nanometers at room temperature, according to measurements by [Hu *et al.* \(2015\)](#), and the thermal conductivity of sapphire is $30 \text{ W m}^{-1} \text{ K}^{-1}$. δ_i/κ_i is then between 10^{-10} and $10^{-8} \text{ m}^2 \text{ KW}^{-1}$ if we choose $\delta_i \approx l$, which is comparable to R_I . Therefore, the value of δ_i should be smaller than a few nanometers to eliminate the error due to the thermal resistance for a slab of bulk sapphire. As previously mentioned, this choice, however, results in the breakdown of local thermal equilibrium.

Moreover, the definition of the interfacial temperature jump ΔT in Eq. (2) is also equivocal when there are heat carriers other than phonons. If material 1 is a metal and material 2 is an insulator, electrons and phonons are the major and minor heat carriers, respectively, in a metal, while phonons are the only heat carrier in an insulator. When there is a heat flux across the interface, the electrons and phonons are in nonequilibrium states. Even if one can define the local temperature of electrons (T_e) and phonons (T_{ph}) near the interface, these two local temperatures must be different. This difference results in an ill-defined local temperature on the metal side near the interface, and extra caution should be taken when treating the metal-insulator interface. In Sec. II.B, we systematically review the theories for phonon transport across the interface. The impacts of other heat carriers are discussed in Sec. II.C.

B. Phonon picture of interfacial thermal transport

In this section, we introduce the theoretical framework for treating interfacial thermal transport when phonons are the dominant heat carriers. When a phonon hits the interface, both reflection and refraction processes take place, as shown in Fig. 2. Considering that the incidence of phonons can take

place on both sides of the interface, the net heat flux is composed of two parts and can be written as

$$J = \frac{1}{V} \sum_{\mathbf{k}\lambda}^+ \hbar \omega_{\mathbf{k}\lambda} v_g^z(\mathbf{k}, \lambda) n(\omega_{\mathbf{k}\lambda}, T_1) \zeta_{1 \rightarrow 2}(\mathbf{k}, \lambda) + \frac{1}{V} \sum_{\mathbf{k}'\lambda'}^- \hbar \omega_{\mathbf{k}'\lambda'} v_g^z(\mathbf{k}', \lambda') n(\omega_{\mathbf{k}'\lambda'}, T_2) \zeta_{2 \rightarrow 1}(\mathbf{k}', \lambda'), \quad (5)$$

where V is the volume, \hbar is the reduced Planck constant, ω is the phonon frequency specified by the phonon wave vector \mathbf{k} and branch index λ , v_g^z is the phonon group velocity normal to the interface ($v_g^z = v_g \cos \theta$ for oblique incidence), n is the phonon distribution function, and ζ is the phonon transmission coefficient. Here the plus (minus) sign refers to the left-to-right (right-to-left) direction, and T_1 and T_2 are the temperatures on the left-hand and right-hand sides of the interface, respectively. A widely used approximation is to treat the distribution function of phonons incident on the interface as the following equilibrium one given by the Bose-Einstein distribution: $n(\omega_{\mathbf{k}\lambda}, T) \approx \bar{n}(\omega_{\mathbf{k}\lambda}, T) = [e^{\hbar \omega_{\mathbf{k}\lambda}/k_B T} - 1]^{-1}$, where k_B is the Boltzmann constant.

In the limit of equal temperatures on both sides ($T_1 = T_2 = T$), there is no net heat flux, rendering the following equality:

$$\sum_{\mathbf{k}\lambda}^+ \hbar \omega_{\mathbf{k}\lambda} v_g^z(\mathbf{k}, \lambda) \bar{n}(\omega_{\mathbf{k}\lambda}, T) \zeta_{1 \rightarrow 2}(\mathbf{k}, \lambda) = - \sum_{\mathbf{k}'\lambda'}^- \hbar \omega_{\mathbf{k}'\lambda'} v_g^z(\mathbf{k}', \lambda') \bar{n}(\omega_{\mathbf{k}'\lambda'}, T) \zeta_{2 \rightarrow 1}(\mathbf{k}', \lambda'). \quad (6)$$

TABLE I. Summary of main theoretical, numerical and experimental methods for the study of ITR.

Theory or method	Key point	Limit	Reference
Acoustic mismatch model (AMM)	Mismatch of acoustic impedance	Quantitative disagreement with experimental data at high temperatures	Khalatnikov (1952)
Diffuse mismatch model (DMM)	Diffusive scattering of phonons	Quantitative disagreement with experimental data at high temperatures	Swartz and Pohl (1989)
Lattice dynamics (LD)	Solve equations of motions	Require exact lattice structure of interface	Young and Maris (1989)
Molecular dynamics (MD)	Track the dynamics of each atom	Require empirical potentials	Maiti, Mahan, and Pantelides (1997)
Green's function method	Decompose the system into interface and two semi-infinite leads	Require the exact lattice structure of the interface and force constants	Wang, Wang, and Zeng (2006)
Boltzmann transport equation	Consider the boundary conditions at the interface	Empirical boundary condition	Lee, Roy, and Farmer (2011)
Pump-probe thermoreflectance technique	Ultrafast laser-based technique to study the nonequilibrium phenomena	Complex optical setup	Eesley (1983)
Electron-beam self-heating method	Electron-beam as heating source and direct measurement of ITR	Limited to 1D heterostructure	Liu <i>et al.</i> (2014)
3ω method	Measurement of three harmonic signal of heating ac current	Low accuracy	Rosenthal (1961)
Traditional heater-sensor method	One-heater and multiple-sensor setup	Limited to low temperatures	Pollack (1969)

Equation (6) can be used to further simplify the expression of the net heat flux as

$$J = \frac{1}{V} \sum_{\mathbf{k}\lambda}^+ \hbar \omega_{\mathbf{k}\lambda} v_g^z(\mathbf{k}, \lambda) \zeta_{1 \rightarrow 2}(\mathbf{k}, \lambda) [\bar{n}(\omega_{\mathbf{k}\lambda}, T_1) - \bar{n}(\omega_{\mathbf{k}\lambda}, T_2)]. \quad (7)$$

From the definition in Eq. (2), the ITC can be computed as

$$h_I(T) = \frac{1}{V} \sum_{\mathbf{k}\lambda} \hbar \omega_{\mathbf{k}\lambda} v_g^z(\mathbf{k}, \lambda) \zeta_{1 \rightarrow 2}(\mathbf{k}, \lambda) \frac{\partial \bar{n}(\omega_{\mathbf{k}\lambda}, T)}{\partial T}. \quad (8)$$

Therefore, the calculation of the ITR is simplified to calculate the phonon transmission coefficient, which can be obtained through various methods. In Sec. II.B, we review the calculations of the transmission coefficient across the interface from both the continuum and atomistic theories that are summarized in Table I. The AMM and DMM are reviewed in Sec. II.B.1. The lattice dynamics, the Green's function method, the molecular dynamics, the Boltzmann transport equation, and the Monte Carlo method are reviewed in Sec. II.B.2.

1. Continuum theory

a. Acoustic mismatch model

A straightforward simplification is to consider both materials as continuous media that are separated by an ideal plane. The details of lattice structures are neglected and the phonons can be treated as elastic waves. This treatment is known as the AMM. In this case, the continuum acoustics is applicable at low temperatures by ignoring the inelastic scattering. Snell's law was evoked to solve the reflection, refraction, and possible mode conversion of incident phonons, as shown in Fig. 2. The angles of incident and transmitted phonons obey $\sin \theta_1 / c_{1\lambda} = \sin \theta_2 / c_{2\lambda}$, where $c_{i\lambda}$ is the sound velocity in material i ($i = 1, 2$) and λ denotes the polarization (longitudinal or transverse). When $c_{1\lambda} > c_{2\lambda}$, phonons from material 1 with an arbitrary incident angle can be transmitted across the interface. In the opposite direction, however, the incident angle from material 2 must not exceed the critical angle $\arcsin(c_{2\lambda}/c_{1\lambda})$ in order to avoid the total reflection.

The transmission coefficient for the elastic wave across a plane can be determined from the continuum acoustic theory as (Little, 1959)

$$\zeta_{1 \rightarrow 2} = \frac{4Z_1 Z_2 \cos \theta_1 \cos \theta_2}{(Z_1 \cos \theta_2 + Z_2 \cos \theta_1)^2}, \quad (9)$$

where $Z_i = \rho_i c_i$ is the acoustic impedance for material i , with ρ denoting the mass density. To further simplify the calculation, the Debye model for isotropic solids is often used, i.e., $\omega = ck$. Besides, the phonon transmission will be zero when the phonon frequency is larger than the Debye frequency ω_D . By replacing the summation of wave vector in Eq. (8) with the integral of frequency in the Debye model and integrating over all incident angles, the ITR can be rewritten as

$$h_I = \frac{1}{(2\pi)^2} \sum_{\lambda} I_{1\lambda} \int_0^{\omega_D} \frac{\hbar \omega_{\lambda}^3}{c_{1\lambda}^2} \frac{\partial \bar{n}(\omega_{\lambda}, T)}{\partial T} d\omega, \quad (10)$$

in which $I_{1\lambda}$ is an integral over all the incident angles as

$$I_{1\lambda} = \int_0^{\pi/2} \zeta_{1 \rightarrow 2}(\theta_1, \lambda) \cos \theta_1 \sin \theta_1 d\theta_1. \quad (11)$$

In Eq. (11) the transmission coefficient is assumed to be dependent on the incident angle only [$\zeta_{1 \rightarrow 2}(\mathbf{k}, \lambda) = \zeta_{1 \rightarrow 2}(\theta_1, \lambda)$]. At the low-temperature limit, the integral in Eq. (10) can be solved analytically and the ITR is given by

$$R_I^{\text{AMM}} = \left[\frac{\pi^2 k_B^4}{15 \hbar^3} \sum_{\lambda} \frac{I_{1\lambda}}{c_{1\lambda}^2} \right]^{-1} T^{-3}. \quad (12)$$

The temperature dependence of $R_I^{\text{AMM}} \propto T^{-3}$ originates from the Debye's T^3 law of heat capacity at low temperatures.

The Debye model used in Eq. (10) requires accurate sound velocities and a proper Debye frequency as input parameters, which can be obtained from experimental measurements or numerical calculations. Moreover, the AMM is not applicable at high temperatures, although it works well at low temperatures because of the absence of phonon scattering. Prasher and Phelan (2001) proposed using a scattering mediated AMM to extend the AMM to high temperatures. The phonon scatterings near the interface are considered by introducing complex wave vectors, which is a typical procedure in the study of phonon attenuation. This effect leads to a larger ITR than the value predicted by the original AMM. Prasher (2009) extended the AMM to study the ITC of an interface with van der Waals contacts. The ITC was found to be proportional to the square of the adhesion energy for weak bonding. Budaev and Bogy (2010a, 2010b) improved the AMM by considering additional thermal vibrations with the Sommerfeld radiation condition.

b. Diffuse mismatch model

The AMM successfully explains the measured temperature dependence of ITR at low temperatures, although the predicted value is usually overestimated. This implies that more heat is transferred across the interface through other mechanisms. Swartz and Pohl (1987) proposed the DMM to take into account the effect of phonon scattering at the interface. In contrast to the AMM, which assumes phonon refraction and specular reflection at the interface, the DMM assumes that the incident phonons are completely scattered diffusively. In other words, the outgoing phonons have no memory of their past. As a result, the following transmission coefficient does not depend on the wave vector or the mode index:

$$\zeta_{1 \rightarrow 2}(\mathbf{k}, \lambda) = \zeta_{1 \rightarrow 2}(\omega), \quad (13a)$$

$$\zeta_{2 \rightarrow 1}(\omega) = 1 - \zeta_{1 \rightarrow 2}(\omega). \quad (13b)$$

When one uses the detailed balance and the Debye model, the transmission probability is $\zeta_{1 \rightarrow 2}(\omega) = \sum_{\lambda} c_{2\lambda}^2 / \sum_{i\lambda} c_{i\lambda}^2$. At low temperatures, the ITR is calculated as (Swartz and Pohl, 1989)

$$R_I^{\text{DMM}} = \left[\frac{\pi^2 k_B^4 (\sum_{\lambda} c_{1\lambda}^{-2}) (\sum_{\lambda'} c_{2\lambda'}^{-2})}{30 \hbar^3 \sum_{i\lambda} c_{i\lambda}^{-2}} \right]^{-1} T^{-3}. \quad (14)$$

Exact phonon dispersion was used by [Duda, Beechem *et al.* \(2010\)](#) to improve the Debye model in the calculation of the DMM. They found that the Debye model underestimates the ITR. [Beechem *et al.* \(2010\)](#) further reformulated the DMM to take into account the optical phonon modes. The contribution from the optical phonon modes was found to be important, although the group velocities of the optical modes were small. [Hopkins and Norris \(2007a\)](#) used the joint vibrational states, which are determined by phonons on both sides of the interface, to replace the phonons near the interface. [Loh, Tay, and Teo \(2010\)](#) modified the DMM by considering the effect of thermal flux on phonon transmission. Inelastic scattering was also incorporated into the DMM by [Hopkins \(2009\)](#), [Hopkins and Norris \(2009\)](#), [Duda, Hopkins *et al.* \(2010\)](#), and [Hopkins, Beechem *et al.* \(2011\)](#). The disorder effect on ITR was studied with a modified DMM by [Beechem and Hopkins \(2009\)](#).

2. Atomistic theory

Both the AMM and the DMM in Sec. II.B.1 were developed based on the continuum theories, in which the detailed atomic structures of two materials are neglected, especially for the solid-solid interfaces. In this section, four categories of numerical methods that take into account the actual atomic structures of the interface are reviewed.

a. Lattice dynamics

The lattice dynamics theory utilizes the actual atomic structures to compute the phonon properties of bulk crystals and can also be used to calculate the ITR. Various realistic factors, such as the actual phonon dispersion, the cutoff frequency, the bonding strength, and the disordered atomic structures of the interface, can all be considered in lattice dynamics calculations.

[Steinbrüchel \(1976\)](#) and [Lumpkin, Saslow, and Visscher \(1978\)](#) calculated the ITR of a one-dimensional (1D) lattice using lattice dynamics. The interface was described by a spring that connects two semi-infinite harmonic chains. The transmission coefficient was found to be a function of phonon wavelength through solving the equations of motion. [Paranjape, Arimitsu, and Krebs \(1987\)](#) extended the lattice dynamical calculation to a 3D simple cubic lattice with a unique lattice constant. The interactions between the nearest and the next nearest neighbors were considered. For simplicity, the displacement of atoms in a parallel direction was set to zero. The equations of motion for the atoms were then reduced to effectively 2D ones that were much easier to solve. The wave-vector-dependent transmission coefficient and reflection coefficient of different modes were calculated by matching the boundary conditions according to Snell's law. The lattice dynamical calculation for 3D lattices with similar lattice structures was performed by [Young and Maris \(1989\)](#). In the calculations, they defined the frequency-dependent transmission spectral density as

$$\Gamma_{\text{LD}}(\omega) = \frac{1}{V} \sum_{\mathbf{k}\lambda} v_{\vec{y}}^2(\mathbf{k}, \lambda) \zeta_{1 \rightarrow 2}(\mathbf{k}, \lambda) \delta[\omega - \omega(\mathbf{k}, \lambda)]. \quad (15)$$

$\Gamma_{\text{LD}}(\omega)$ can be obtained from the numerical results by solving the equations of motion for the atoms near the interface. The ITC in Eq. (8) then can be written in a simple form as

$$h_I = \int_0^\infty \hbar \omega \Gamma_{\text{LD}}(\omega) \frac{\partial \bar{n}(\omega, T)}{\partial T} d\omega. \quad (16)$$

It is straightforward to extend the aforementioned lattice dynamical calculations to cases with dissimilar lattices. One critical problem arises when handling dissimilar lattices: how does one match the atoms of two materials at the interface? [Pettersson and Mahan \(1990\)](#) assumed that the translational symmetry of both materials along the interface are maintained. When two materials have exactly the same lattice structure and the same lattice constant as shown in Fig. 3(a), the atoms are automatically matched and considering the interactions

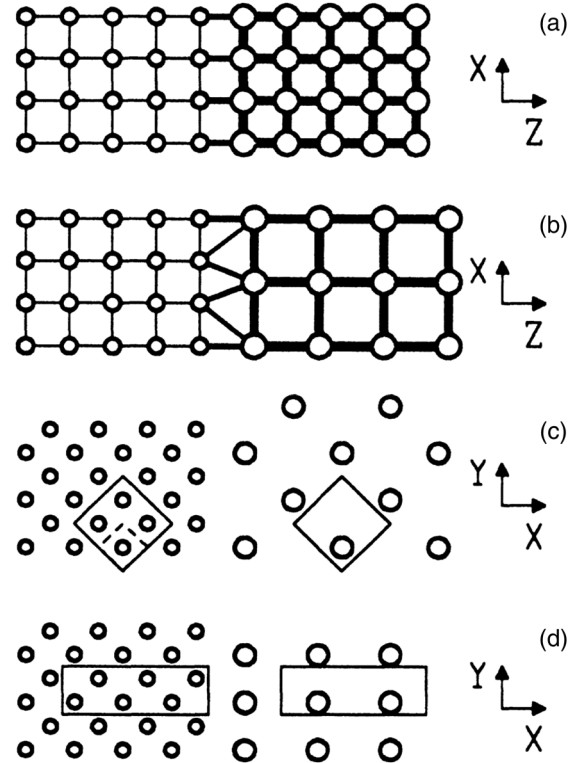


FIG. 3. Location of atoms along the x - z plane perpendicular to the interface between (a) two similar lattices and (b) two dissimilar lattices. (c) Location of atoms along the x - y plane for two dissimilar fcc lattices when the interface is parallel to the (100) plane. The atoms in material 1 are shown to the left and the atoms in material 2 are shown to the right. Surface unit cells are shown in boxes when the lattice constant of material 2 is twice the lattice constant of material 1. The surface unit cell is larger than the primitive unit cell in material 1 marked by the dashed line. (d) Location of atoms along the x - y plane for two identical fcc lattices with different crystalline orientations. The (100) plane is parallel to the interface on the left, and the (110) plane is parallel to the interface on the right. The surface unit cell is marked with boxes. From [Pettersson and Mahan, 1990](#).

between the nearest neighboring atoms results in a good approximation.

When two materials have the same lattice structure but different lattice constants as shown in Fig. 3(b), it is convenient to introduce a surface unit cell in which there is a least common multiple of the lattice constant of material 1 (a_1) and the lattice constant of material 2 (a_2). In other words, a_1 and a_2 should be commensurate. The translational symmetry of the surface unit cell along the interface is essential to reduce the complexity of the calculation. Figure 3(c) shows a typical selection of a surface unit cell for two fcc lattices, and the interface is along the (100) plane when $a_2 = 2a_1$.

In the case of real materials, it is difficult to find an exact least common multiple of two lattice constants. The same lattice structure and a small lattice mismatch can be realized in a few interfaces, such as the epitaxial Al (111)/sapphire(0001) interface (Cheng *et al.*, 2020) and the Si/Ge interface (Li and Yang, 2012a). Figure 3(d) shows the location of atoms near the interface between two identical materials with fcc lattice structures. The (100) plane of the material on the left-hand side is parallel to the interface, and the (110) plane of the material on the right-hand side is parallel to the interface. The distance along the x direction between the atoms on the right-hand side along the (110) plane is about $1.5a_1$. It is a rough approximation to choose a surface unit cell whose length along the x direction is $3a_1$. Zhao and Freund (2005) and Wang and Wang (2007) used the lattice dynamical method to calculate the ITR of the Si/Ge interface. The lattice constant of Si is 5.43 \AA , which is close to the lattice constant of Ge (5.66 \AA). They neglected this difference so as to avoid the complicated matching problem. It is clear that an imperfect selection of the surface unit cell would artificially introduce undesired stress into the system and thus affect the intrinsic value of ITR. Alkurdi, Pailhès, and Merabia (2017) improved the work of Zhao and Freund (2005) by replacing the empirical potential with the interatomic force constants obtained from *ab initio* calculations.

The disorder effect on the phonon transmission coefficient was studied by Fagas, Kozorezov, Lambert, and Wigmore (1999) and Fagas, Kozorezov, Lambert, Wigmore, Peacock *et al.* (1999). A scattering region was introduced into the lattice dynamical calculations. The atomic mass in this region is set to be random. The S matrix was used to describe the phonon transport through this scattering region. A strong frequency dependence of phonon transmission coefficient was observed, which was attributed to the phonon scatterings induced by the disorder.

b. Green's function approach

The Green's function method was originally used to calculate the ballistic transport of electrons in mesoscopic systems (Datta, 1997). Inspired by its success in electron transport, researchers have used the nonequilibrium Green's function (NEGF) method, also known as the atomistic Green's function method, to study phonon transport in nanostructures, which was independently developed by Wang, Wang, and Zeng (2006), Wang *et al.* (2007), and Zhang, Fisher, and Mingo (2007a, 2007b). It is often used to handle the ballistic transport of phonons when the anharmonic effect is negligible

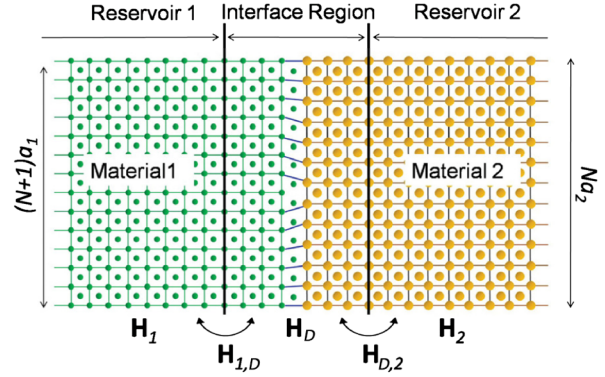


FIG. 4. Schematic diagram for the Green's function method. There are two semi-infinite leads attached to the interface region. Consequently, the Hamiltonian is divided into five parts. From Li and Yang, 2012a.

(such as at low temperatures), although the inclusion of anharmonicity in the formalism is in principle feasible (Mingo, 2006; Wang, Wang, and Zeng, 2006; Dai and Tian, 2020).

When one starts with the equilibrium atomic positions and the interatomic interaction potential, the harmonic matrix H can be written and the Green's function G is the inversion matrix of $(\omega^2 I - H)$, where I is the unit matrix. It is impossible to directly compute the matrix inversion since the dimension of matrix H is extremely large. In the Green's function method, the entire system is decomposed into three parts: a central interface region of interest and the outer two semi-infinite leads that are in contact with thermal reservoirs at different temperatures, as shown in Fig. 4. The matrix H can be divided into five parts: two semi-infinite leads H_1 and H_2 , the interface region H_D , and the interaction between the leads and the interfaces $H_{1,D}$ and $H_{D,2}$. The isolated Green's functions of two semi-infinite leads can be calculated by the decimation technique, and the isolated Green's function of the central system is calculated using direct matrix inversion. The Green's function of the entire system can be calculated by coupling the Green's function of these three isolated parts. There are nine components of the Green's function in which the most interesting component at the interface region G_D is calculated as (Wang, Wang, and Lü, 2008)

$$G_D = [\omega^2 I - H_D - \Sigma_1 - \Sigma_2]^{-1}, \quad (17)$$

where Σ_1 and Σ_2 are the self-energy matrices due to the semi-infinite leads. The energy-dependent transmission function $\Xi(\omega)$ across the interface includes both the phonon transmission probability and information about the phonon density of states (DOS) and can be obtained from the Green's function as (Wang, Wang, and Lü, 2008)

$$\Xi(\omega) = \text{Tr}[\Gamma_1 G_D \Gamma_2 G_D^\dagger]. \quad (18)$$

Γ_1 and Γ_2 are obtained as follows from the imaginary part of the self-energies (Wang, Wang, and Lü, 2008):

$$\Gamma_1 = i(\Sigma_1 - \Sigma_1^\dagger), \quad \Gamma_2 = i(\Sigma_2 - \Sigma_2^\dagger). \quad (19)$$

Finally, the ITC is written in Landauer form as (Wang, Wang, and Zeng, 2006; Zhang, Fisher, and Mingo, 2007a)

$$h_I = \frac{1}{2\pi A} \int_0^\infty \hbar\omega \frac{\partial \bar{n}(\omega, T)}{\partial T} \Xi(\omega) d\omega. \quad (20)$$

Note that Eq. (20) is actually the same as Eq. (16), yielding the equality $\Gamma_{LD}(\omega) = \Xi(\omega)/2\pi A$. Here $\Gamma_{LD}(\omega)$ has the unit of m^{-2} , while $\Xi(\omega)$ is dimensionless. More details about the Green's function method were given in the reviews by Wang, Wang, and Lü (2008) and Wang *et al.* (2014).

Zhao and Freund (2009) and Tian, Esfarjani, and Chen (2012) used this method to study the roughness effect on the ITR. The first-principles calculation was used to calculate the interatomic force constants, which are the input parameters in the Green's function method (Tian, Esfarjani, and Chen, 2012; Gu, Li, and Yang, 2015). Li and Tian (2019) further calculated the ITR across grain boundaries in silicon.

The original Green's function method calculates the total phonon transmission function. Huang, Murthy, and Fisher (2011) modified the method to study the mode-resolved phonon transmission that can distinguish the contributions from different phonon modes. Similar work was done by Ong and Zhang (2015) and Ong (2018b) using the concept of the Bloch matrix, and by Sadasivam, Waghmare, and Fisher (2017) using the Dyson equation and the Lippmann-Schwinger equation. Latour, Shulumba, and Minnich (2017) further incorporated the first-principles calculations into the computation of mode-resolved phonon transmission. Sadasivam *et al.* (2017) also combined first-principles calculations and the atomistic Green's function to calculate the ITR of metal silicide-silicon interfaces. Yang, Latour, and Minnich (2018) applied the modified method to calculate the ITR of crystalline-amorphous interfaces. Ong, Zhang, and Zhang (2016) calculated the phonon transport across strained graphene/h-BN lateral interface.

The obstacles to the wide application of the atomistic Green's function method include the lattice mismatch and anharmonicity. To avoid lattice mismatch, Zhang, Fisher, and Mingo (2007b) assumed that the lattice constants of Si and Ge are the same; i.e., strained interfaces without dislocations were considered. As a result, the translational invariance along the x - y plane is applicable to simplify the calculation. However, this assumption introduces an artificial strain to the system that affects the ITR. Li and Yang (2012a) used a large supercell along the x - y plane to eliminate the strain effect. The lattice constants of Si and Ge are 5.43 and 5.66 Å, respectively. They chose a supercell containing 25×25 unit cells of Si or 24×24 unit cells of Ge. The large size of the supercell leads to a large increase of computation complexity. A recursive method based on the Dyson equation was used to reduce the computational cost. The ITC of a lattice-mismatched interface was found to be smaller than the ITC of a lattice-matched interface.

Early works on the Green's function approach were limited to the ballistic phonon transport without consideration of the anharmonic phonon scattering. Dai and Tian (2020) took into account the inelastic phonon scattering by adding a many-body self-energy term in the calculations. Ong (2018a)

combined the atomistic Green's function method and the S matrix to include the phonon scattering effect.

c. Molecular dynamics simulation

Molecular dynamics simulation is a classical approach to simulate the thermal transport by tracking the dynamics of each atom in the system via Newton's equation of motion and the empirical interatomic interactions. It is an atomic level simulation and has many unique advantages, such as modeling realistic materials, considering complex structures and atomic level details (roughness, surface reconstruction, defect, strain, etc.), and taking into account anharmonicity to all orders. Depending on the existence of temperature bias, MD simulation can be categorized into nonequilibrium molecular dynamics (NEMD) and equilibrium molecular dynamics (EMD) simulations. In addition, it can be combined with other theories to model the thermal transport. In this section, we review the MD-based method for the prediction of ITR.

(i) NEMD simulation is a direct method to mimic the heat source and heat sink in experiment by imposing a temperature gradient on the system, as shown in Fig. 1. Two thermostats with different temperatures are applied to the two ends of the system, which leads to a heat flow from the high-temperature to the low-temperature direction. The fixed boundary condition is often used at the two ends of the simulation domain. Popular thermostat schemes (also known as heat baths) for temperature control include the Nosé-Hoover (Nosé, 1984; Hoover, 1985), Langevin (Dhar, 2008), and Berendsen (Berendsen *et al.*, 1984) methods. More details on the thermostat can be found elsewhere (Chen, Zhang, and Li, 2010b).

With an assumption of local thermal equilibrium, the local temperature T_l can be recorded in the simulation by computing the ensemble-averaged kinetic energy in each local region as

$$T_l = \frac{\langle \sum_{i=1}^N m_i \mathbf{v}_i \cdot \mathbf{v}_i \rangle}{3Nk_B}, \quad (21)$$

where N is the number of atoms in the local region, m_i and \mathbf{v}_i are the mass and velocity of the i th atom, respectively, and the bracket denotes the ensemble average. When NEMD simulation runs for a long enough time, the nonequilibrium steady-state temperature distribution in the system can be obtained, as shown in Fig. 1. The temperature discontinuity ΔT at the interface can be directly captured by NEMD simulations, which can be computed with an extrapolation of the linear temperature gradient in each segment (the solid lines in Fig. 1) toward the interface. The heat flux J is computed as the energy transported per unit time across the unit area, which can be recorded by the energy injection or extraction rate in the heat source or sink. Finally, the ITR can be computed according to Eq. (2).

In addition to the calculation of the ITR value, the theoretical method of quantifying the phonon contribution in the frequency domain was also developed based on NEMD simulations (Sääskilähti *et al.*, 2014, 2015; Zhou and Hu, 2015). If one considers an interface with atoms i and j on the left-hand and right-hand sides of the interface, respectively,

the heat flux across the interface $J_{L \rightarrow R}$ can be expressed as (Sääskilahti *et al.*, 2015, 2016; Zhou and Hu, 2015)

$$J_{L \rightarrow R} = \frac{1}{2A} \sum_{i \in L} \sum_{j \in R} \langle \mathbf{F}_{ij} \cdot (\mathbf{v}_i + \mathbf{v}_j) \rangle, \quad (22)$$

where A is the cross-section area and \mathbf{F}_{ij} is the interatomic force between two interfacial atoms. The spectral heat flux $\mathcal{J}_{L \rightarrow R}(\omega)$ can be obtained from the real part of the Fourier transform as (Sääskilahti *et al.*, 2016)

$$\mathcal{J}_{L \rightarrow R}(\omega) = \frac{2}{A} \text{Re} \sum_{i \in L} \sum_{j \in R} \int_{-\infty}^{\infty} \langle \mathbf{F}_{ij}(t) \cdot \mathbf{v}_i(0) \rangle e^{i\omega t} dt, \quad (23)$$

where t is the correlation time between the force and the velocity. The spectral ITC $g(\omega)$ can then be defined as

$$g(\omega) = \frac{|\mathcal{J}_{L \rightarrow R}(\omega)|}{\Delta T}. \quad (24)$$

In fact, this spectral method based on NEMD simulation works for both homogeneous and heterogeneous systems. For homogeneous systems, the interface is imaginary inside the simulation domain, and this method can be used to compute spectral phonon properties (Sääskilahti *et al.*, 2015; Zhou and Hu, 2015) such as the phonon mean free path and the transmission coefficient. It can recover the ballistic limit for the phonon transmission function calculated using the Green's function method, in which the anharmonic phonon-phonon interaction is often neglected, while it can also incorporate the full level of lattice anharmonicity through MD simulation in calculating the phonon transmission (Sääskilahti *et al.*, 2015). For heterogeneous systems, the interface is a real one, and this method can take into account the inelastic phonon scattering process across the solid-solid interface (Sääskilahti *et al.*, 2014), and has been widely used to study the thermal transport mechanisms across various kinds of interfaces (Giri, Braun, and Hopkins, 2016; Han, Merabia, and Müller-Plathe, 2017a, 2017b; Ramos-Alvarado and Kumar, 2017; Ma *et al.*, 2018; Hung, Hu, and Shiomi, 2019; Chen *et al.*, 2020; Peng *et al.*, 2022). Moreover, this spectral method was further developed to account for a full quantification of the inelastic contribution from the three-phonon scattering process (Zhou and Hu, 2017) and the modal thermal nonequilibrium (Feng *et al.*, 2019).

(ii) NEMD simulation can directly probe the interfacial temperature jump, and thus is widely used in the study of the interfacial heat transfer problem. To suppress the fluctuation of temperature in the nonequilibrium steady state, a large heat flux or temperature difference is often imposed to the small-scale sample in NEMD simulations. For instance, the NEMD simulations of homogeneous systems typically involve a large temperature gradient ($\sim 10^9$ K m⁻¹) that is beyond the experimental range (Schelling, Phillpot, and Koblinski, 2002a). It is not clear *a priori* whether the large temperature gradient might induce the nonlinear response of the system (Sánchez and López, 2013). On the other hand, EMD simulation can overcome this issue, as no temperature gradient is used in that simulation, and the intrinsic transport properties of the

system can be derived from the heat flux correlation function at thermal equilibrium via the fluctuation-dissipation theory.

ITC can be computed in EMD simulation from the Green-Kubo formula as (Barrat and Chiaruttini, 2003)

$$h_I = \frac{A}{k_B T^2} \int_0^{\infty} \langle J(t)J(0) \rangle dt, \quad (25)$$

where $J(t)$ is the time-dependent interfacial energy flux across the cross-section area A . Microscopically, $J(t)$ can be computed from the interfacial energy change rate as

$$J(t) = \frac{1}{A} \frac{dE_I(t)}{dt}, \quad (26)$$

where $E_I(t)$ is the total interaction energy for the interface summed over all the interfacial atoms. For a pairwise interaction at the interface, the energy flux $J(t)$ can be written as Eq. (22).

It should be noted that the Green-Kubo relation in Eq. (25) is valid only for infinitely large systems in which the heat capacities of the two materials are infinite ($C_{\text{tot}} \rightarrow \infty$). For a finite system, the ITC is related to the heat flux correlation function as (Barrat and Chiaruttini, 2003)

$$h_I e^{-wt_s} = \frac{A}{k_B T^2} \int_0^{t_s} \langle J(t)J(0) \rangle dt, \quad (27)$$

where $w = Ah_I/C_{\text{tot}}$ is a constant and t_s is the integration time. Therefore, by fitting the integral of heat flux correlation function in Eq. (27) with an exponential function, ITC can be obtained as the fitting constant in a finite time EMD simulation.

There are two stages in a typical EMD simulation. The entire system is first thermally equilibrated with the canonical [i.e., constant atom numbers, volume, and temperature (NVT)] ensemble via a constant temperature thermostat to ensure that each segment of the interface reaches thermal equilibrium. Afterward, the thermostat is withdrawn and the microcanonical ensemble [i.e., constant atom numbers, volume, and energy (NVE)] EMD simulation runs long enough for the proper decay of the correlation function, during which time the instantaneous energy flux $J(t)$ is recorded. Finally, ITR can be computed using Eq. (27) up to a finite simulation time. More details on the implementations of EMD simulation can be found elsewhere (Chen, Zhang, and Li, 2010a; McGaughey and Larkin, 2014; Liang and Hu, 2018).

(iii) In addition to the direct NEMD simulation, there is another type of nonequilibrium simulation in which the transient thermal relaxation process is recorded to extract the ITR. This method mimics the short-pulse laser excitation in experiment. After the entire system reaches thermal equilibrium at the constant temperature T_0 , one segment of the interface is instantaneously heated to a higher temperature, by either rescaling the atomic velocities or attaching to a high-temperature thermostat for a short period. The thermostat is then withdrawn, and the transient temperature difference $\Delta T(t)$ between the heated and unheated segments is recorded in the NVE ensemble. As the nonequilibrium temperature will

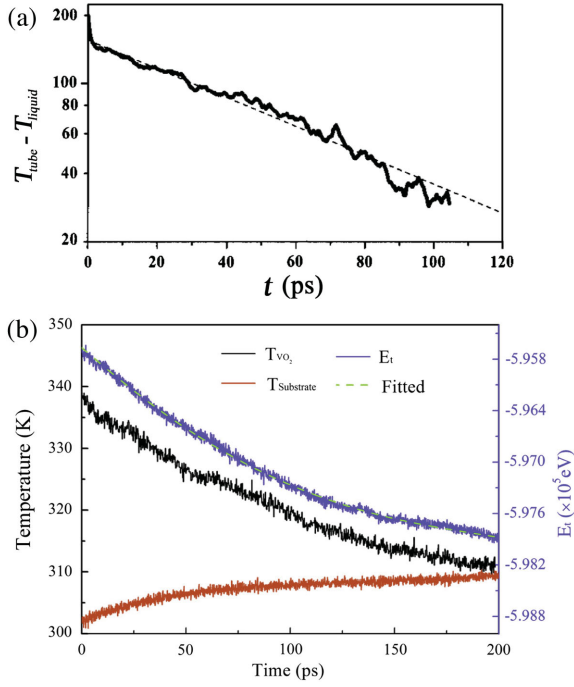


FIG. 5. Two kinds of fitting approaches used in the transient thermal relaxation simulation. (a) Fitting of the temperature difference between two segments according to the exponential decay function in Eq. (28) for a solid-liquid interface. From Shenogin *et al.*, 2004. (b) Fitting of the total energy in one segment according to the integral function in Eq. (31) for a solid-solid interface. From Wang, Zhang *et al.*, 2020.

eventually be relaxed, this method is also known as the *approach-to-equilibrium* MD simulation.

When the total ITR is much larger than the thermal resistance of each segment (i.e., there is a small Biot number), the decay of the temperature difference between the heated and unheated segments can be determined using the lumped heat capacity model as (Stoner and Maris, 1993; Huxtable *et al.*, 2003)

$$\Delta T(t) = \Delta T_0 e^{-t/\tau} \quad (28)$$

and the decay constant τ is given by

$$\tau = \frac{R_I C_{\text{eff}}}{A}, \quad (29)$$

where C_{eff} is the effective heat capacity of the hybrid system. C_{eff} can be replaced by the heat capacity of the solid segment for the solid-liquid interface (Huxtable *et al.*, 2003; Shenogin *et al.*, 2004), while it can be expressed as $C_{\text{eff}} = C_1 C_2 / (C_1 + C_2)$ for the solid-solid interface (Carlborg, Shiomi, and Maruyama, 2008), where C_1 and C_2 , respectively, are the heat capacities of the two solid segments. As shown in Fig. 5(a), the decay constant can be determined by fitting the transient temperature difference according to Eq. (28), and R_I can then be computed using Eq. (29).

In the calculation of R_I based on the lumped heat capacity model, knowledge of the effective heat capacity, which is obtained from either an additional independent simulation or the literature, is required. This problem can be overcome by

tracking the energy evolution during the relaxation process (Wang, Zhang *et al.*, 2020). In the presence of an interfacial temperature jump ΔT , the heat flux across the interface can be written as

$$J(t) = \frac{1}{A} \frac{dE_t(t)}{dt} = \frac{\Delta T(t)}{R_I}, \quad (30)$$

where E_t denotes the total energy of one segment that forms the interface. By assuming that R_I is independent of temperature within the temperature difference ΔT , we can further write Eq. (30) in the integral form as (Wang, Zhang *et al.*, 2020)

$$E_t(t) = E_0 + \frac{A}{R_I} \int_0^t \Delta T(t) dt. \quad (31)$$

Since the energy evolution $E_t(t)$ is already tracked in the MD simulation, no additional simulation is required. By fitting the energy evolution $E_t(t)$ based on Eq. (31), R_I can be obtained in this method as a fitting parameter, as shown in Fig. 5(b).

(iv) Although MD simulations can compute the value of ITR for complex realistic material systems with atomic level interfacial structures considered in the simulation, it does not provide the physics for the underlying scattering mechanism at the interface.

On the other hand, the LD theory models the lattice vibrations in terms of a series of *vibrational normal modes*, and thus provides a natural platform to study the mechanism of phonon transport across the interface. Because of the computational complexity in treating the anharmonicity (Wang, Wang, and Lü, 2008), the harmonic approximation is typically used when modeling interfaces, which can model the elastic-scattering process only at the interface (Young and Maris, 1989).

Under the harmonic approximation, the atomic vibration can be expressed as a linear combination of decoupled eigenstates called the *normal mode*, which is specified by the wave vector \mathbf{k} and branch index λ . A wave packet is the spatially localized normal mode in the coordinate space, which can be realized in simulation by setting the initial atomic displacement as (Schelling, Phillpot, and Keblinski, 2002b)

$$u_\alpha(bl, 0) = a_{\mathbf{k}\lambda} \xi_{b\alpha}(\mathbf{k}, \lambda) e^{i\mathbf{k} \cdot (\mathbf{R}_l - \mathbf{R}_0)} e^{-|\mathbf{R}_l - \mathbf{R}_0|^2 / \eta^2}, \quad (32)$$

where $u_\alpha(bl, 0)$ is the α th component of the initial displacement for the b th atom in the l th unit cell, a and ξ are the amplitude and eigenvector for a given mode (\mathbf{k}, λ) , respectively, and \mathbf{R}_l is the equilibrium position of the l th unit cell. The last term in Eq. (32) is a Gaussian envelope for localizing the wave packet at \mathbf{R}_0 , and the width of the wave packet can be controlled by the parameter η . The eigenvector can be computed by diagonalizing the dynamical matrix of the perfect bulk crystal. Based on the plane-wave solution form $\exp(i\mathbf{k} \cdot \mathbf{R} - i\omega_{\mathbf{k}\lambda} t)$, the initial atomic velocity should also be specified as $v_\alpha(bl, 0) = -i\omega_{\mathbf{k}\lambda} u_\alpha(bl, 0)$. After setting the initial atomic displacement and velocity, the propagation process of the Gaussian wave packet can be monitored using MD simulations with an *NVE* ensemble. When a wave packet

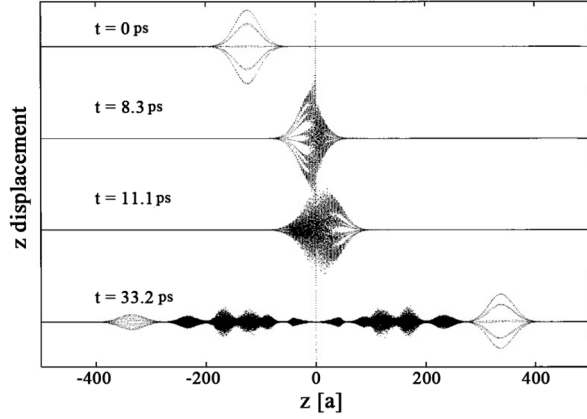


FIG. 6. Wave packet simulation of a short-wavelength LA phonon transmission process across a grain boundary located at $z = 0$. From Schelling, Phillpot, and Koblinski, 2004.

is launched on the left-hand side of the interface, the phonon transmission coefficient across the interface $\zeta_{L \rightarrow R}$ can be computed as the total energy on the right-hand side of the interface in the final stage after the scattering divided by the initial incident energy of the wave packet. Finally, the ITC can be calculated according to Eq. (8).

As shown in Fig. 6, the transmission and reflection process for the short-wavelength phonon wave packet across a grain boundary can be well modeled. In addition, mode conversion due to elastic scattering can also be captured, thereby providing physical insight into the scattering mechanism. The amplitude of each normal mode after scattering can be determined as (Schelling, Phillpot, and Koblinski, 2004)

$$a_{\mathbf{k}\lambda} = \sum_{b\alpha} \xi_{b\alpha}^*(\mathbf{k}, \lambda) u_{\alpha}(b\mathbf{l}, t_f) e^{-i\mathbf{k}\cdot\mathbf{R}\mathbf{l}}, \quad (33)$$

where $u_{\alpha}(b\mathbf{l}, t_f)$ is the atomic displacement at the final time t_f .

d. The Boltzmann transport equation and the Monte Carlo method

The phonon Boltzmann transport equation is a traditional tool for studying the heat conduction of mesoscopic systems, which is written in terms of the phonon distribution function n_{λ} for mode λ and the group velocity \mathbf{v}_g^{λ} as

$$\frac{\partial n_{\lambda}(t, \mathbf{r}, \mathbf{k})}{\partial t} + \mathbf{v}_g^{\lambda} \cdot \nabla T \frac{\partial n_{\lambda}(t, \mathbf{r}, \mathbf{k})}{\partial T} = \left. \frac{\partial n_{\lambda}(t, \mathbf{r}, \mathbf{k})}{\partial t} \right|_{\text{col}}. \quad (34)$$

In Eq. (34) $[\partial n_{\lambda}(t, \mathbf{r}, \mathbf{k})/\partial t]_{\text{col}}$ is the collision term. A proper mathematical treatment of phonon collision at the interface is essential to the calculation of ITR. Lee, Roy, and Farmer (2011) used the phonon collision rule by placing boundary nodes in the middle of the links between materials 1 and 2. The distribution function can then be numerically solved using the lattice Boltzmann method. A phonon-interface relaxation time was introduced in the calculations to characterize the scattering strength. The Monte Carlo method was also used to solve the Boltzmann transport equation. Jeng *et al.* (2008) compared random numbers between zero and unity with certain transmission probability when a phonon encounters the interface. The phonon is transmitted

through the interface if the random number is less than the transmission probability and is reflected otherwise. The gray assumption was made by Singh, Murthy, and Fisher (2011) to simplify the calculations, where the spectral-dependent scattering rate is approximated by an averaged MFP (Chen, 1998). Ran, Guo, and Wang (2018) and Ran *et al.* (2018) used an energy-based deviational phonon Boltzmann equation (Péraud and Hadjiconstantinou, 2011) to calculate the ITR. The deviational energy distribution $E_n^d = \hbar\omega[n - \bar{n}(T_{\text{eq}})]$, where T_{eq} is the referenced equilibrium temperature, was solved numerically. The transmission probability was taken from the DMM. Taking one step forward, Sun *et al.* (2019) used the first-principles method to calculate the phonon group velocity. Yang and Minnich (2017) introduced an additional specular parameter to take into account specular and diffusive transmission (reflection).

e. Other models for phonon transport

There are several other models that are not widely used and not easy to categorize. We list these models in this section.

Kozorezov *et al.* (1998) proposed a scattering mediated phonon transmission model for a nonideal solid-solid interface. The roughness and imperfection of the interface were found to result in the scattering mediated transmission for high-frequency phonons. Duda, Norris, and Hopkins (2011) developed a model in the classical limit at high temperatures. They assumed that phonons are scattered not only at the interface but also within an area near the interface. A linear temperature dependence of ITC was obtained from this model. Persson, Volokitin, and Ueba (2011) proposed a model that accounts for the strength of the interaction between solids. Van den Brink and Dekker (1996) presented a model that can be derived from the Kubo formula. Kakodkar and Feser (2015) proposed a numerical method for calculating the phonon transport based on a frequency-domain decomposition of the atomistic equation of motion. Budaev and Bogoy (2010c) developed a self-consistent acoustic model to clarify the role of acoustic waves in heat transfer across an interface. Jagannadham (2010) calculated ITR using a distribution of thermal sources present at the interface on either side.

C. Impacts of other energy carriers

In addition to phonons, there are other heat carriers in various forms of condensed matter. For example, in metals, the major heat carriers are electrons; in semiconductors, both electrons and holes are the heat carriers; in magnets, magnons are the heat carriers at low temperatures; in liquid ^3He , both the ^3He quasiparticles and the collective excitation, such as the zero sound, can also carry heat. When there are different types of heat carriers on either side of the interface, the definition of the temperature jump is questionable because of the non-equilibrium thermal states between different heat carriers, as we mentioned in Sec. II.A.2. In this section, we introduce methodology that takes the nonphonon contribution to the ITR into account.

Figure 7 illustrates the heat transfer network when material 1 has two types of heat carriers, noted as Carriers 1a and 1b.

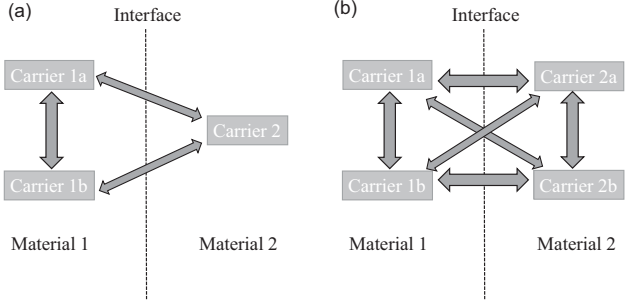


FIG. 7. Schematic diagrams of the heat transfer network at the interfaces. There are two types of heat carriers (Carriers 1a and 1b) in material 1. Material 2 has (a) one type of heat carrier (Carrier 2) and (b) two types of heat carriers (Carriers 2a and 2b).

Consider the case in which there is only one type of heat carrier in material 2, which is denoted as Carrier 2 in Fig. 7(a). When a heat current flows across the interface, there are the following two direct heat transfer channels:

$$\begin{aligned} \text{Carrier 1a} &\rightarrow \text{Carrier 2,} \\ \text{Carrier 1b} &\rightarrow \text{Carrier 2;} \end{aligned}$$

plus the two following possible indirect heat transfer channels:

$$\begin{aligned} \text{Carrier 1a} &\rightarrow \text{Carrier 1b} \rightarrow \text{Carrier 2,} \\ \text{Carrier 1b} &\rightarrow \text{Carrier 1a} \rightarrow \text{Carrier 2.} \end{aligned}$$

If material 2 also has two types of heat carriers, there are four direct and eight indirect heat transfer channels across the interface, as shown in Fig. 7(b). As a result, the overall ITR should be determined by the thermal resistance network that is analogous to the electrical series-parallel circuit. In general, the network in Fig. 7 can be extended to any interface when materials 1 and 2 have arbitrary types of carriers.

Considering a metal-nonmetal interface, we now introduce the TTM for electron-phonon coupling to discuss the detailed approach for handling the nonphonon contribution. In the TTM, both electrons and phonons contribute to the thermal transport on the metal side, and they are associated with the temperatures T_e and T_{ph} , respectively. On the nonmetal side, thermal transport is dominated by the phonon, which has the temperature T_n .

On the metal side, the temperature fields of both electrons and phonons in the TTM are modeled by the following two coupled heat diffusion equations:

$$\rho_e C_e \frac{\partial T_e}{\partial t} = \nabla \cdot (\kappa_e \nabla T_e) - G_{e-ph}(T_e - T_{ph}) + \rho_e r_e, \quad (35a)$$

$$\rho_{ph} C_{ph} \frac{\partial T_{ph}}{\partial t} = \nabla \cdot (\kappa_{ph} \nabla T_{ph}) + G_{e-ph}(T_e - T_{ph}) + \rho_{ph} r_{ph}, \quad (35b)$$

where ρ , C , and κ denote the mass density, heat capacity, and thermal conductivity, respectively. The subscripts e and ph denote the electron and phonon, respectively. G_{e-ph} is the

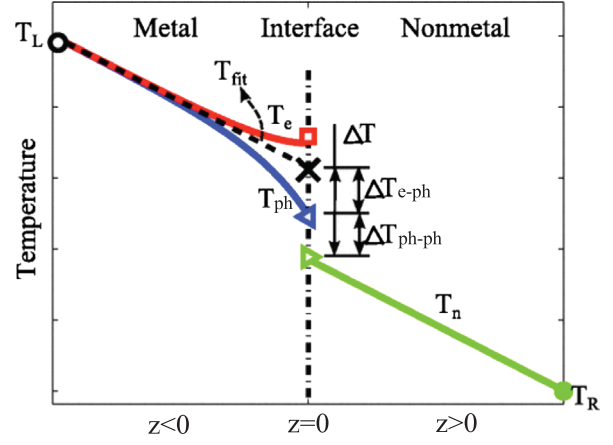


FIG. 8. Representative temperature profile for a metal-nonmetal interface in the TTM. T_e and T_{ph} denote the temperatures of electrons and phonons on the metal side ($z < 0$), respectively, while T_n is the phonon temperature in the nonmetal side ($z > 0$). T_{fit} denotes the linear fit of the temperature profile in the electron-phonon equilibrium region. The total temperature jump at the interface ($\Delta T = \Delta T_{e-ph} + \Delta T_{ph-ph}$) is composed of both an electron-phonon coupling contribution ΔT_{e-ph} and a phonon-phonon coupling contribution ΔT_{ph-ph} . From Wang, Ruan, and Roy, 2012.

electron-phonon coupling parameter defined by Kaganov, Lifshitz, and Tanatarov (1957) and Allen (1987), while r_e and r_{ph} denote the mass normalized source term for electrons and phonons, respectively. When there is no source term and one further considers a steady-state heat transport across the interface along the z direction (Fig. 2), Eq. (35) can be simplified as

$$\kappa_e \frac{d^2 T_e}{dz^2} - G_{e-ph}(T_e - T_{ph}) = 0, \quad (36a)$$

$$\kappa_{ph} \frac{d^2 T_{ph}}{dz^2} + G_{e-ph}(T_e - T_{ph}) = 0. \quad (36b)$$

Consider the case in which the metal is on the left-hand side of the interface ($z < 0$) and the nonmetal is on the right-hand side ($z > 0$), as shown in Fig. 8. In the region far from the interface ($z \rightarrow -\infty$), electrons and phonons are in thermal equilibrium. With this boundary condition, Eq. (36) can be solved analytically. Furthermore, electrons are insulated at the interface, i.e., $dT_e/dz|_{z=0} = 0$, giving rise to the following solution on the metal side ($z < 0$) (Majumdar and Reddy, 2004):

$$T_e(z) = B \left(\frac{G_{e-ph}}{\kappa_e} \ell^2 \right) e^{z/\ell} - B \left(\frac{G_{e-ph}}{\kappa_e} \ell \right) z + B', \quad (37a)$$

$$T_{ph}(z) = B \left(\frac{G_{e-ph}}{\kappa_e} \ell^2 - 1 \right) e^{z/\ell} - B \left(\frac{G_{e-ph}}{\kappa_e} \ell \right) z + B', \quad (37b)$$

where $\ell = (G_{e-ph}/\kappa_e + G_{e-ph}/\kappa_{ph})^{-1/2}$ is a characteristic length and B and B' are constants to be determined.

On the nonmetal side, Fourier's law applies and a linear temperature profile T_n is obtained. Based on the continuity of heat flux at the interface, the constants in Eq. (37) can be determined. As shown in Fig. 8, by extrapolating the linear temperature profile in the equilibrium region on the metal side toward the interface, the total temperature jump at the interface is composed of the following two parts:

$$\Delta T = T_{\text{fit}}(0) - T_n(0) = \Delta T_{e\text{-ph}} + \Delta T_{\text{ph-ph}}, \quad (38)$$

where $\Delta T_{e\text{-ph}}$ and $\Delta T_{\text{ph-ph}}$ denote the temperature drop at the interface due to electron-phonon and phonon-phonon interactions, respectively. Correspondingly, the ITC can be computed as (Majumdar and Reddy, 2004)

$$h_l = \frac{\kappa_{\text{ph}} \sqrt{G_{e\text{-ph}}(1/\kappa_e + 1/\kappa_{\text{ph}})}}{\kappa_e/(\kappa_{\text{ph}} + \kappa_e) + (\kappa_{\text{ph}}/h_{\text{ph-ph}}) \sqrt{G_{e\text{-ph}}(1/\kappa_e + 1/\kappa_{\text{ph}})}}, \quad (39)$$

where $h_{\text{ph-ph}}$ is the ITC from the phonon-phonon contribution due to $\Delta T_{\text{ph-ph}}$ at the interface. In metals, electrons are the dominant heat carriers ($\kappa_e \gg \kappa_{\text{ph}}$), so the ITR can be further simplified as

$$R_l \approx \frac{1 + \sqrt{G_{e\text{-ph}}\kappa_{\text{ph}}/h_{\text{ph-ph}}}}{\sqrt{G_{e\text{-ph}}\kappa_{\text{ph}}}} = \frac{1}{h_{e\text{-ph}}} + \frac{1}{h_{\text{ph-ph}}}, \quad (40)$$

where $h_{e\text{-ph}} = \sqrt{G_{e\text{-ph}}\kappa_{\text{ph}}}$ denotes the ITC contributed by the electron-phonon interaction due to $\Delta T_{e\text{-ph}}$.

Li *et al.* (2015), Lombard, Detcheverry, and Merabia (2015), and Wu and Luo (2015) further extended the TTM. Li *et al.* (2015) derived the following more general form of the total ITC that is equivalent to a series-parallel thermal resistor network:

$$h_l = \frac{1}{\ell/\kappa_e + 1/h_{e\text{-ph}}^{\text{direct}}} + \frac{1}{\ell/\kappa_{\text{ph}} + 1/h_{\text{ph-ph}}}. \quad (41)$$

The direct energy transfer channel from electrons in metal to phonons in nonmetal was considered by introducing a thermal conductance $h_{e\text{-ph}}^{\text{direct}}$. In the limit case of $\kappa_e \gg \kappa_{\text{ph}}$, $\ell/\kappa_{\text{ph}} \approx 1/\sqrt{\kappa_{\text{ph}}G} = 1/h_{e\text{-ph}}$ and ℓ/κ_e is negligible. Equation (41) can then be rewritten as

$$h_l \approx h_{e\text{-ph}}^{\text{direct}} + \frac{1}{1/h_{e\text{-ph}} + 1/h_{\text{ph-ph}}}. \quad (42)$$

Equation (40) can be recovered when $h_{e\text{-ph}}^{\text{direct}} = 0$.

The phonon-phonon contribution $h_{\text{ph-ph}}$ in Eq. (40) needs to be computed using other methods. Wang, Ruan, and Roy (2012) demonstrated that MD simulation can be coupled with the TTM to handle the electron-phonon coupling and compute R_l in the metal-nonmetal interface without using DMM. In their work, the heat diffusion equation for electrons in Eq. (36a) is solved iteratively with the finite difference (FD) method, and the heat diffusion process for phonons is modeled by the MD simulation.

To communicate information between two solvers (FD and MD), two additional terms are added to the equations of motion for the i th atom in the MD part following Langevin dynamics,

$$m_i \frac{\partial \mathbf{v}_i}{\partial t} = \mathbf{F}_i - \mu_i \mathbf{v}_i + \tilde{\mathbf{F}}_i, \quad (43)$$

where \mathbf{F}_i is the original force exerted on atom i according to interatomic empirical potentials and μ_i is a friction term representing the energy loss by electron-ion interaction and is given by (Duffy and Rutherford, 2007)

$$\mu_i = \frac{m_i G_{e\text{-ph}}}{3N_i k_B}, \quad (44)$$

with N_i denoting the atom number density. $\tilde{\mathbf{F}}_i$ is a random force that is related to the damping term via the fluctuation-dissipation theory and is given by (Phillips and Crozier, 2009)

$$\tilde{\mathbf{F}}_i = \sqrt{\frac{6k_B T_e \mu_i}{\Delta t}} \tilde{\mathbf{R}}, \quad (45)$$

where Δt is the time step used in the simulation, and $\tilde{\mathbf{R}}$ is a random vector with each component generated from the uniformly distributed random number between $[-1, 1]$. To provide feedback to the FD solver from MD simulation, the electron-phonon coupling term $G_{e\text{-ph}}(T_e - T_{\text{ph}})$ in Eq. (36a) is replaced by the following energy exchange term (Wang, Ruan, and Roy, 2012):

$$E_{e\text{-ph}} = (-\mu_i \mathbf{v}_i + \tilde{\mathbf{F}}_i) \cdot (\mathbf{v}_i \Delta t). \quad (46)$$

The additional terms $(-\mu_i \mathbf{v}_i + \tilde{\mathbf{F}}_i)$ in Eq. (43) due to electron-phonon coupling can equilibrate the electron and phonon subsystems to a common temperature. The force constant and electron-phonon coupling parameter can be computed from first-principles calculations (Bauer *et al.*, 1998; Esfarjani and Stokes, 2008; Sadasivam, Waghmare, and Fisher, 2015).

After getting the steady-state temperature profile shown in Fig. 8, the temperature jump at the interface ΔT can be obtained by extrapolating the linear fit line of the temperature in the electron-phonon equilibrium region in the metal side toward the interface and then subtracting T_n on the nonmetal side at the interface. The heat flux J is recorded in a MD simulation via the energy change rate in the heat bath, and finally the ITR can be computed according to Eq. (2).

D. Experimental tools

There are two types of techniques to measure ITR, i.e., the steady-state measurement (including the traditional heater-sensor method and the electron-beam self-heating method) and the transient measurement (including the differential 3 ω method and the pump-probe thermoreflectance technique).

1. Pump-probe thermoreflectance technique

In the past 30 years, the pump-probe thermoreflectance technique with an ultrafast laser has emerged as a fast, reliable,

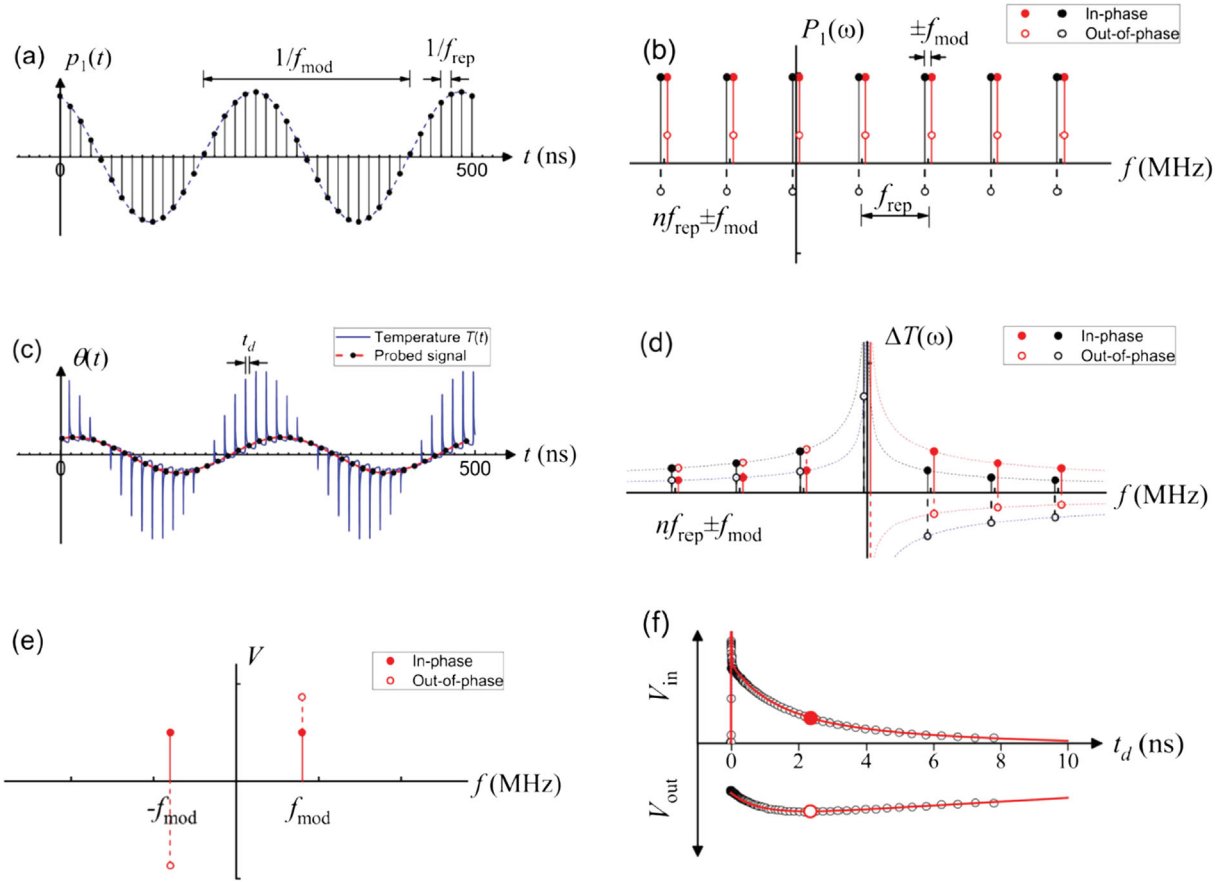


FIG. 9. Signal detection mechanism in TDTR and FDTR. (a) Modulated pump pulsed by a sine wave from electro-optic modulator in TDTR. (b) Modulated pump in FDTR. (c) Temperature signal at the sample surface (solid line) and the probe signal at a fixed delay time (t_d) in TDTR. (d) Temperature signal of the in-phase component and out-of-phase component in FDTR. (e) Signal detected by a rf lock-in amplifier. (f) V_{in} and V_{out} signal vs delay time in TDTR. From [Jiang, Qian, and Yang, 2018](#).

and powerful platform to study nonequilibrium phenomena such as electron-phonon coupling ([Elsayed-Ali *et al.*, 1987](#); [Brorson *et al.*, 1990](#); [Groeneveld, Sprik, and Lagendijk, 1992, 1995](#); [Giri *et al.*, 2015](#)), quasiballistic or coherent phonon transport ([Thomsen *et al.*, 1984](#); [Wright and Kawashima, 1992](#); [Hase *et al.*, 2005](#); [Luckyanova *et al.*, 2012](#); [Ravichandran *et al.*, 2014](#); [Vermeersch *et al.*, 2014](#)), and phonon MFP spectra ([Koh and Cahill, 2007](#); [Minnich *et al.*, 2011](#)) due to its capability to detect temperature variations at the micrometer scale with a time resolution of a picosecond. Therefore, it is possible to measure the thermal transport properties of a wide range of materials and the interfaces between them, including bulk materials, thin-film, multilayer materials, liquid, and various solid-solid interfaces.

The thermoreflectance technique was first developed in 1970s and the continuous wave (cw) laser was used for both heating and temperature sensing to measure the thermal properties of materials ([Rosencwaig and Gersho, 1976](#); [Rosencwaig, 1982](#)). [Paddock and Eesley \(1986\)](#) further developed this technique with a picosecond laser and measured the thermal diffusivity of thin films. They were followed by [Stoner *et al.* \(1992\)](#) and [Stoner and Maris \(1993\)](#), who used this technique to measure the ITR of dielectric materials (BaF₂, diamond, and sapphire) and metals, including Pb, Au, Al, Ti, etc., in the

temperature range of 50–300 K. The transient thermoreflectance technique has two variations: the TDTR and the frequency-domain thermoreflectance (FDTR) method, which are distinguished by a time delay or frequency difference between the pump laser and the probe laser [Figs. 9(a) and 9(b)].

In the TDTR measurement, a mode-locked laser with femtosecond pulses at an ~ 80 MHz repeating rate and wavelengths ranging from 632 to 1030 nm is used as the light source ([Capinski and Maris, 1996](#); [Wilson *et al.*, 2012](#)). The laser source is then split into a pump beam and a probe beam. The former is modulated by an electro-optic modulator at frequency between ~ 0.2 and ~ 20 MHz [Fig. 9(c)], while the latter will pass a delay stage via the mechanical movement that introduces an optical delay between pump and probe beams. The pump beam is used to create a small temperature rise (usually 10% of the absolute temperature or < 10 K, whichever is smaller) in the metal transducer, and the probe beam is used to detect the temperature decay rate since the optical reflectance rate of the transducer is temperature dependent. The reflected probe beam is collected by a fast photodiode detector. The radio-frequency lock-in amplifier is used to pick up both the in-phase signal (V_{in}) and the out-of-phase signal (V_{out}) at the modulated frequency with ([Barragán *et al.*, 2001](#))

$$\begin{aligned}
 V_{\text{in}} &= \text{Re}[\Delta R_f(t)] \\
 &= \frac{1}{2} \sum_{j_n=-\infty}^{\infty} [\Delta T(\omega_0 + j_n \omega_s) \\
 &\quad + \Delta T(-\omega_0 + j_n \omega_s)] \exp(i j_n \omega_s t_d), \quad (47)
 \end{aligned}$$

$$\begin{aligned}
 V_{\text{out}} &= \text{Im}[\Delta R_f(t)] \\
 &= -\frac{i}{2} \sum_{j_n=-\infty}^{\infty} [\Delta T(\omega_0 + j_n \omega_s) \\
 &\quad - \Delta T(-\omega_0 + j_n \omega_s)] \exp(i j_n \omega_s t_d), \quad (48)
 \end{aligned}$$

where ΔT is related to the thermal properties of the measured material including ITR, thermal conductivity of the substrate, etc. The ratio between the in-phase signals and out-of-phase signals $-V_{\text{in}}/V_{\text{out}}$ or $\varphi = \tan^{-1}(V_{\text{out}}/V_{\text{in}})$ versus the delay time t_d is used to fit the experimental data using a thermal transport model and to derive the thermal properties of the samples [Figs. 9(e) and 9(f)].

Cahill (2004) extended the 1D heat diffusion equation into three dimensions to fit the experimental data, while Schmidt, Chen, and Chen (2008) extended the approach to 3D and anisotropic thermal conduction. For example, based on Fourier's law of heat conduction, the solution of the heat diffusion equation in cylindrical coordinates for a multilayered system can be written as

$$C \frac{\partial T}{\partial t} = \frac{\eta_a \kappa_z}{r} \frac{\partial}{\partial r} \left(r \frac{\partial T}{\partial r} \right) + \kappa_z \frac{\partial^2 T}{\partial z^2}, \quad (49)$$

where κ_r , κ_z , and C are, respectively, the in-plane thermal conductivity, cross-plane thermal conductivity, and volumetric heat capacity and $\eta_a = \kappa_r/\kappa_z$ is the anisotropic parameter. The complicated thermal model enables the TDTR method to obtain thermal properties or free fitting parameters including heat capacity, in-plane thermal conductivity, cross-plane thermal conductivity, and ITR. Some parameters (such as C) can be measured separately to reduce the unknown fitting parameters. The uncertainties of multiple free fitting parameters can be determined by a Jacobian matrix-based equation (Monachon, Weber, and Dames, 2016; Yang, Ziade, and Schmidt, 2016). The results show that the uncertainty in determining ITR, for example, the GaN/Al interface, is approximately 5% with modulated frequencies of both 1 and 10 MHz (Jiang, Qian, and Yang, 2018).

The typical thickness of a transducer is approximately 50–100 nm in TDTR and FDTR. Assuming that the ITC between the transducer and the sample underneath is $h_I = 100 \text{ MW m}^{-2} \text{ K}^{-1}$, the thermal relaxation time τ_G is estimated to be $\sim 1.5 \text{ ns}$ according to $\tau_G = h_s C / h_I$, where $h_s = 60 \text{ nm}$ and $C = 2.5 \text{ MJ m}^{-3} \text{ K}^{-1}$ are the thickness and heat capacity of the metal transducer, respectively. To access timescales down to $\sim 100 \text{ ps}$ in high thermal conductivity materials and to increase the sensitivity for measuring high ITC by reducing the modulation frequency and cooling time of the transducer, the transducer with a thickness of less than 10 nm is needed, rather than 50–100 nm. To this end, a new temperature sensing technique, i.e., the time-resolved

magneto-optic Kerr effect (TR-MOKE), was invented with a much thinner magnetic transducer film (Liu, Choi, and Cahill, 2014; Chen *et al.*, 2016; Kimling *et al.*, 2017). Instead of temperature-dependent thermoreflectance, TR-MOKE utilizes the temperature-dependent Kerr rotation of polar light to detect the temperature response from the magnetic transducer, which includes Co/Pt, Co/Pd, CoFe/Pt, TbFe, etc. A magnetic transducer with a thickness down to 4.2 nm was used with the TR-MOKE method by Kimling *et al.* (2017). The smaller thermal mass of the transducer offers a better sensitivity to the ITC measurement.

FDTR is the other domain of the thermoreflectance technique, where the reflected signal is collected as a function of the modulation frequency of the pump beam (Schmidt, 2008; Schmidt, Cheaito, and Chiesa, 2009; Malen *et al.*, 2011), in contrast to the optical delay of the arrival time between the pump beam and the probe beam in TDTR. FDTR is much easier since it can use a cw laser and avoid a complex mechanical delay stage. Alternatively, by fixing the location of the delay stage, a TDTR setup can be used as FDTR (Fig. 9) (Schmidt, Cheaito, and Chiesa, 2009). The results can be transformed between two domains. The thermal transport model of cw FDTR is similar to that of TDTR, and V_{in} and V_{out} can still be given by Eqs. (47) and (48) by setting j_n to zero. Furthermore, Wei *et al.* (2013) and Braun *et al.* (2018) used dual-frequency time-domain thermoreflectance, which combines TDTR and FDTR, to measure the thermal conductivity and volumetric heat capacity simultaneously. This approach is extended to incorporate the TDTR phase over a range of frequencies suitable for FDTR, and thus can combine the advantages of multifrequency TDTR and FDTR for thermal measurements with a better sensitivity than the single domain method.

In principle, the cw laser can be modulated at any frequency. However, it faces a practical problem due to the bad signal-to-noise ratio at high frequency. To overcome this problem, Regner, Majumdar, and Malen (2013) implemented a heterodyne technique, i.e., broadband frequency-domain thermoreflectance, to extend the frequency from 20 to 200 MHz. This extension in frequency enables the FDTR with a new capability to study phonon MFP spectra of materials (Regner, Majumdar, and Malen, 2013; Regner *et al.*, 2013) in a manner similar to that found in frequency-dependent TDTR.

2. Electron-beam self-heating method

The electron-beam self-heating method introduced by Wang *et al.* (2011) and Liu *et al.* (2014) provides a direct measurement of the ITR of a 1D heterostructure (Liu *et al.*, 2014; Zhao, Liu *et al.*, 2020), the thermal contact resistance (Wang *et al.*, 2011; Aiyiti, Bai *et al.*, 2018), and hence the intrinsic thermal conductivity of 1D and 2D materials (Aiyiti, Bai *et al.*, 2018; Wang, Chen *et al.*, 2020). This method is a modified thermal bridge method and the measurement setup is mounted inside the scanning electron microscope (SEM) chamber. Therefore, before discussing the electron-beam self-heating method, we introduce the thermal bridge method.

The thermal bridge method was invented by Kim *et al.* (2001) to measure the thermal conduction of an individual carbon nanotube. Complicated fabricating processes including

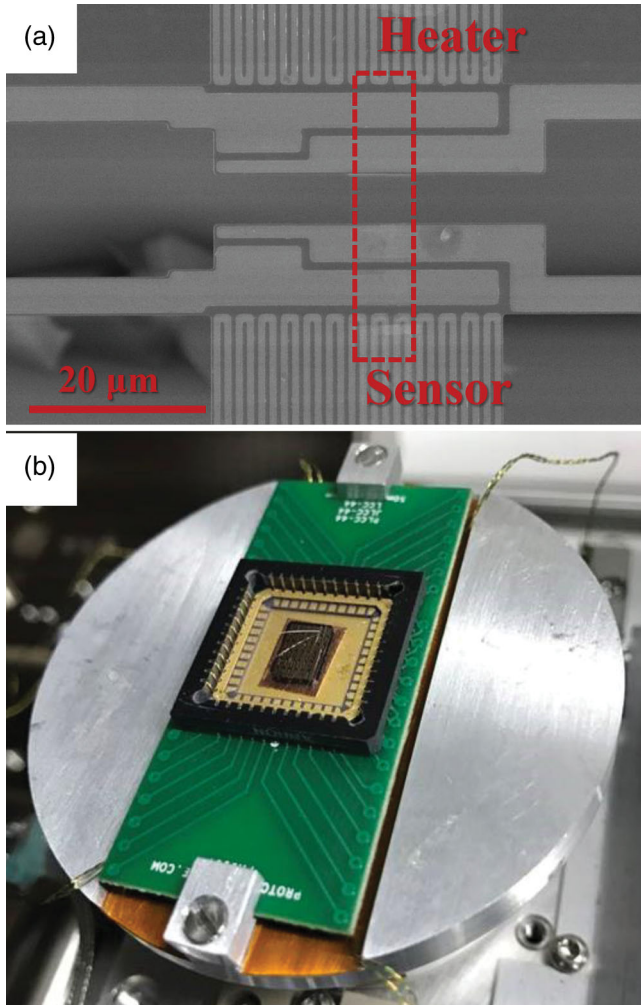


FIG. 10. (a) Scanning electron microscope (SEM) image of suspended MEMS devices. The red rectangle indicates the 2D materials that are ready to measure. The scale bar is $20 \mu\text{m}$. (b) Measurement stage (electron-beam self-heating method) and chip carrier adapted inside the SEM sample holder in Tongji University.

thermal evaporation, electron-beam lithography, and dry or wet etching were used to fabricate suspended microelectromechanical systems (MEMSs) that are suitable for thermal property measurement (Kim *et al.*, 2001; Shi *et al.*, 2003). A nanomanipulation system or drop casting method is used to suspend nanoscale materials onto the MEMS such that the temperature variation and heat flow could be detected at the microscale or nanoscale.

Figure 10(a) is the SEM image of the MEMS device. The MEMS consists of two low-strain SiN_x membranes, each of which is suspended by five or six long beams, with the length ranging from 400 to $600 \mu\text{m}$ and a metallic resistive coil prepatterned on top of each SiN_x membrane and beam, which can serve as either a heater (R_h) or a temperature sensor (R_s) depending on the direction of the heat flow. The sample to be measured thermally contacts these two membranes and is electrically isolated from the resistive foil. To measure the thermal conductivity, an ac current combined with a dc current is applied to one SiN_x membrane, while another ac current

with the same amplitude is applied to the other membrane. The dc current is used to apply microwatt joule heat to the heater and increase its temperature (T_h), while the ac current is used to measure the electric resistance R_h and R_s , corresponding to T_h and T_s , respectively. The joule heat at the heater is conducted by both the suspended beams and the suspended sample and gradually increases the temperature of the heater and sensor. When the MEMS is at the steady state, the thermal conductance of sample σ_s and the suspended SiN_x beams σ_l can be obtained from $\sigma_l = (Q_h + Q_l)/(\Delta T_h + \Delta T_s)$ and $\sigma_s = \Delta T_s \sigma_l / (\Delta T_h - \Delta T_s)$, where Q_h , Q_l , ΔT_h , and ΔT_s are the heating power on the heater, the heating power on one SiN_x beam, and the temperature rise at R_h and R_s , respectively.

This thermal bridge method is considered as one of the most successful techniques for measuring the thermal conductivity and thermopower of the nanotubes (Chang *et al.*, 2006; Peng *et al.*, 2006), nanowires (Hochbaum *et al.*, 2008; Dong *et al.*, 2018, 2020), 2D materials, and thin films (Pettes *et al.*, 2011; Xu *et al.*, 2014; Lee *et al.*, 2015; Wang, Guo *et al.*, 2016; Aiyiti *et al.*, 2018; Aiyiti, Bai *et al.*, 2018; Zhao *et al.*, 2018), despite several bottlenecks and challenges (Xu, Chen, and Li, 2016; Fu *et al.*, 2020; Wu, Tang, and Xu, 2020). The main challenge lies in the thermal contact resistance R_c at the two ends of the samples, i.e., the thermal contact resistance between metal electrodes and samples, which is unavoidably contained in the measured total thermal resistance. Therefore, a number of samples with different lengths should be measured to extrapolate R_c (Aiyiti, Bai *et al.*, 2018; Guo, Huang *et al.*, 2019; Wang, Liang *et al.*, 2020). Alternatively, a new method, the electron-beam self-heating technique, is used to measure R_c and ITR in 1D and 2D systems.

Compared to the TDTR, which measures the ITR of the 2D interface, the electron-beam self-heating technique is the only technique to date to measure the ITR of a heterostructure in one dimension. This method is upgraded from the thermal bridge method, and the measurement setup is mounted inside the SEM chamber during the thermal measurement [Fig. 10(b)]. Unlike the thermal bridge method, in which R_h and R_s act as the heating source and temperature sensor, both membranes in the electron-beam self-heating method are temperature sensors and the moving focused high-energy electron-beam acts as the heating source. Unlike in the method for measuring R_c using different samples with different lengths (Guo, Huang *et al.*, 2019; Wu *et al.*, 2021), the electron beam scans along the length of the sample and the high energy of the electrons is absorbed locally and therefore heats the local spot. The local heat spreads toward the two membranes and increases their temperatures.

One can assume that the focused electron beam moves from left to right [Figs. 11(a) and 11(b)], and the measured thermal resistance $R(x)$ based on Fourier's law, from the left to the heating spot, is given by $R(x) = R_b \{[\alpha_0 - \alpha_i(x)]/[1 + \alpha_i(x)]\}$, where $\alpha_0 = \Delta T_{L0}/\Delta T_{R0}$ and $\alpha_i = \Delta T_L/\Delta T_R$, R_b is the thermal resistance of the six beams, and x is the distance from the left membrane to the heating spot. ΔT_L and ΔT_R are the measured temperature rises. ΔT_{L0} and ΔT_{R0} are the temperature rises of the two membranes measured using the thermal bridge method under arbitrary joule heating power and without electron-beam scanning. The thermal conductivity of the samples can be calculated as $\kappa = 1/[(dR/dx)A]$, where A is the cross-section

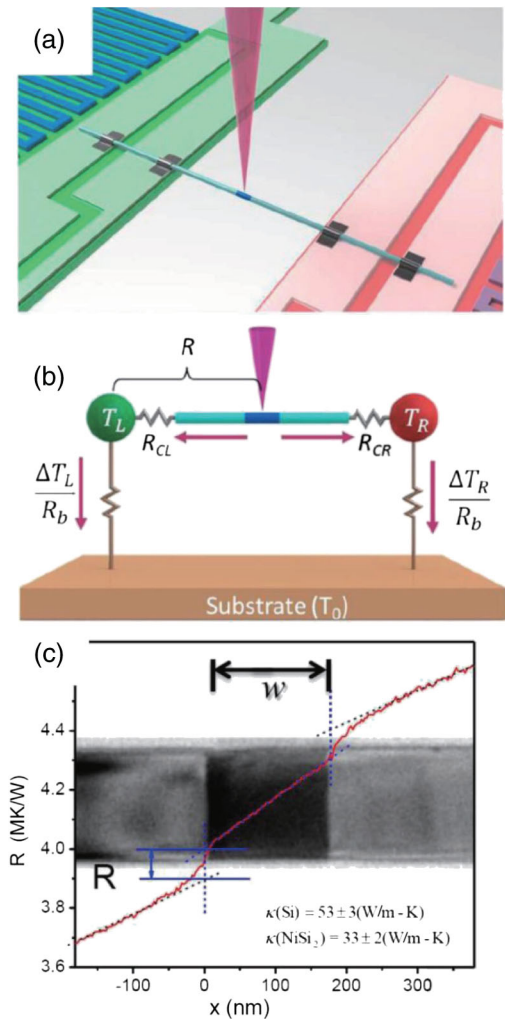


FIG. 11. Electron-beam self-heating method. (a) Schematic and (b) equivalent thermal resistance circuit of electron-beam self-heating method. (c) Measured $R(x)$ when the electron beam is scanned across a metal-semiconductor interface and a sudden jump, representing ITR, is observed. From Liu *et al.*, 2014.

area of the samples. When the focused electron beam is scanning across an interface, a sudden change of $R(x)$ can be detected that refers to the ITR at the interface [Fig. 11(c)].

The electron-beam self-heating method is considered as the only technique thus far that can directly measure the ITR of a 1D heterostructure. However, this technique is limited to thick samples in which there are relatively long paths for the focused electron beam to go through and more atoms and electrons available to interact with each other (Aiyiti, Bai *et al.*, 2018; Yuan *et al.*, 2020). The energy loss of the incident electrons comes mainly from the inelastic scattering between the incident electrons and the atomic electrons surrounding the nucleus, which is dependent on the incident electron energy and the distance traveled, i.e., the thickness of the sample, indicating that a thicker sample holds a better signal-to-noise ratio. This is because the limited absorbed energy will lead to a low-temperature increase at two sensors and make it difficult to acquire the reasonable signal.

3. Other methods

a. 3ω method

The 3ω method has been widely used for measuring the thermal conductivity of bulk materials, the cross-plane thermal conductivity of thin films, and the ITR (Lee and Cahill, 1997; Cahill, Bullen, and Lee, 2000; Alvarez-Quintana and Rodríguez-Viejo, 2008; Jin *et al.*, 2011). This technique uses a microfabricated metal strip, which is deposited on the sample surface, as both the heating source and the temperature sensor (Cahill, 1990; Dames, 2013). An ac current with a frequency ω is used for heating, while the third harmonic voltage measured provides information about the thermal properties. The differential 3ω method that compares a pair of measurements with and without the interface should be used (Chen *et al.*, 2009). A series of samples with different unit thicknesses are measured to separate the block units and their interfaces. The measurement sensitivity is limited by the thermal penetration depth $d_{th} \sim \kappa t_c / C^{0.5}$, where t_c is the transient heating timescale. Therefore, the measurement sensitivity in 3ω method is 2 to 3 orders of magnitude lower than that in the pump-probe thermoreflectance method since the heating frequency in the 3ω method is below ~ 100 kHz, which is in sharp contrast to the 0.2–200 MHz results for TDTR and FDTR (Regner, Majumdar, and Malen, 2013).

b. Traditional heater-sensor method

This method uses one heater to create the temperature gradient and several sensors to measure the temperature jump across the interface. This method is successful in studying ITR, especially at low temperatures, and has made tremendous contributions to this field during the 20th century (Pollack, 1969; Swartz and Pohl, 1989). It requires the material on each side of the interface to be highly conductive and the ITR to be high, suggesting that this method is limited to low temperatures, or even cryogenic temperatures, where the MFP is comparable to the sample dimension (Schmidt and Umlauf, 1976; Swartz and Pohl, 1989). One or multiple thermometers are mounted on each side of interface and the measured temperature is extrapolated to the interface. This method requires a careful thermometer placement to avoid artifacts due to phonon-thermometer scatterings. In pure metals, electrons dominate the thermal transport and the phonon scattering at the thermometers will not affect the temperature measurement; therefore, the location of a thermometer is not critical. However, the position of the thermometer is critical if one side of the interface is dielectric since the phonon MFP is often affected by the condition of the dielectric sample surface (Swartz and Pohl, 1989).

E. Summary of methods

In this section, we review various theoretical, computational, and experimental methods in the study of ITR, as summarized in Table I. Tremendous progress has been made in the last 30 years with both theoretical and experimental approaches. The rapid development of supercomputers makes large-scale numerical simulations possible, although the size of simulation is still restricted by the computer memory.

New numerical methods are highly desired. The utilization of microfabrication and nanofabrication techniques and an ultra-fast laser significantly improves the precision and reliability of ITR measurements, especially for the solid-solid interface. The developments of low-temperature techniques in the 1960s and 1970s, particularly the commercialization of the dilution refrigerator, stimulated the research of Kapitza resistance at temperatures far below 1 K. Measurement methods of ITR in solid-liquid helium interfaces were covered in previous reviews (Pollack, 1969; Swartz and Pohl, 1989) and thus are not addressed in this review.

III. SOLID-SOLID INTERFACES

The ITR of solid-solid interfaces is of great importance in electronics and thermal engineering. Both theoretical methods and experimental tools have been improved tremendously in the last 30 years, as we discussed in Sec. II. The study of interfaces has been extended from macroscopic length to nanoscale. ITC is crucial for heat transfer in nanoscale structures when the phonon MFP is comparable to the size of the nanostructures. In the meantime, the underlying physical mechanisms for the electron-electron, electron-phonon, and phonon-phonon couplings at the interfaces are complicated. The ITC across both macroscopic and nanoscale interfaces is basically related to the atomic properties of the materials on two sides of the interface, i.e., structure, defects, pressure, bonding, etc.

Section III.A reviews the phonon transport across various solid-solid interfaces. The electron-phonon coupling at metal-dielectric interface is discussed in Sec. III.B. The contribution of electrons at metal-metal interfaces is discussed in Sec. III.C. The interfaces with nanostructures are discussed in Sec. III.D.

A. Phonon transport across various interfaces

In this section, we focus our discussion on various impact factors for phonon-phonon transport across various solid-solid interfaces including the dielectric-dielectric, metal-dielectric, and metal-metal interfaces.

1. Comparison of theoretical approaches

Hopkins *et al.* (2009) studied the phonon transmission in a 1D atomic chain for the Si/Ge system. For a homogeneous 1D chain, they found that both AMM and NEGF calculations give identical results. However, the phonon transmission function differs for the Si/Ge atomic junction. The wave nature of phonon transport and interference across the atomic junction are captured by NEGF calculations in terms of the multiple oscillation feature of the transmission coefficient, which is absent in the results from AMM theory. Such a difference suggests that AMM theory neglects the multiple reflections and does not account for the phase coherence of phonon waves at multiple interfaces.

Landry and McGaughey (2009) compared the ITR for the Si/Ge interface predicted by the NEGF formalism and NEMD simulations. In the NEGF formalism, two kinds of phonon distributions are considered in the calculation of ITR: R_E for the equilibrium Bose-Einstein distribution and R_{NE} the non-equilibrium bulklike distribution obtained by solving the

phonon Boltzmann transport equation. Their calculation results reveal that NEGF results of R_E for the Si/Ge interface is in good agreement with the MD result at low temperatures, where the interface scattering is elastic, while R_{NE} is 40% – 60% lower than the MD result. The ITR predicted by DMM is between R_E and R_{NE} . The underestimation of R_{NE} is attributed to the bulk phonon distribution used in the calculation, which might not be accurate at the interface.

Using a series of mass-mismatched Lennard-Jones (LJ) solids as examples, Merabia and Termentzidis (2012) compared EMD and NEMD simulations for computing the ITR of the solid-solid interface. They found that these two MD methods give intrinsically different values of ITR as they probe different energy transmission coefficients. In EMD simulation, the transmission is primarily governed by the mismatch of DOS between two solids, which is consistent with the classical DMM theory. In contrast, results from NEMD simulations are consistent with the nonequilibrium generalization of AMM theory. In their study, h_I computed with NEMD simulations is 5 times that of the result computed with EMD simulations. This begs the question of the consistency between EMD and NEMD simulations in studying thermal transport across the solid-solid interface.

In MD simulations, the finite size effect is a crucial factor in the calculation of ITR, which has been widely studied in the literature (Li, Lan, and Wang, 2005; Carlborg, Shiomi, and Maruyama, 2008; Chen, Zhang, and Li, 2012; Merabia and Termentzidis, 2012; Jones *et al.*, 2013; Liang and Koblinski, 2014a; Liang, Sasikumar, and Koblinski, 2014; Zhang, Ouyang, Cheng *et al.*, 2020; Ren *et al.*, 2021). Based on the solid-solid interface formed by two mass-mismatched LJ solids, Merabia and Termentzidis (2012) computed the ITC with system length varying up to approximately 100 unit cells using both NEMD and EMD simulations. They found that h_I computed with the EMD method decreases with system length, while the size effect of h_I computed with the NEMD method is less significant.

Jones *et al.* (2013) studied the more realistic Al/GaN interface with NEMD simulations, and extended the system length up to 0.17 μm and the simulation time up to 100 ns in order to establish a reliable trend. Their NEMD simulation results revealed that the ITR is insensitive to the cross-section area, but proportional to the inverse of system length as $R_I \propto 1/L$. This linear trend is similar to the size-dependent thermal resistivity of homogeneous material observed in NEMD simulations (Schelling, Phillpot, and Koblinski, 2002a; Sellan *et al.*, 2010). By extrapolating this linear trend toward infinite length ($1/L \rightarrow 0$), a size-independent R_I can be obtained in NEMD simulations.

Using the GaN/AlN interface, Liang, Sasikumar, and Koblinski (2014) further investigated the origin of the linear trend $R_I \propto 1/L$ observed in NEMD simulations. They found that, when the system length is short, the specular reflection of ballistic phonons at the smooth external surface leads to the reduction of the effective phonon transmission coefficient across the interface, causing a large R_I value at small system sizes. They further demonstrated that a strong size effect with a smooth surface can be removed by attaching a rough external surface to both sides of the interface, rendering a size-independent R_I that is equivalent to the extrapolation of a

linear trend with a smooth surface toward the infinite length limit. In other words, by attaching a rough external surface, a reliable, size-independent R_I value can be obtained in NEMD simulations with a much smaller computational cost.

By comparing the length-dependent R_I between epitaxial and nonepitaxial interfaces in NEMD simulations, Liang and Koblinski (2014a) demonstrated that the opposite conclusion, regarding which interface has larger R_I , can be drawn at different system lengths, which highlights the importance of properly treating the finite size effect in NEMD simulations. Moreover, Liang and Koblinski (2014a) also explored the size effect of R_I in EMD simulations. They found that oscillations exist in the integral of the autocorrelation function due to the echoes of phonon reflection from the external smooth surface, which can be removed by attaching a rough external surface. By fitting the initial part of the integral without echoes based on Eq. (27), a size-independent R_I can be extracted from EMD simulations, and the use of a rough external surface also can help to reduce the computational cost. Their simulation results show that the size-independent R_I obtained from EMD simulations is consistent with the extrapolated R_I value ($L \rightarrow \infty$) from NEMD simulations. Therefore, EMD and NEMD simulations can provide consistent predictions of R_I when the finite size effect is properly treated. More details on the finite size effect of R_I in MD simulation can be found elsewhere (Liang and Hu, 2018).

2. Validation of AMM and DMM

Experiments have shown that the characteristics of interface is critical in determining the ITR and phonon modes at interface, which somehow causes the deviation from AMM at cryogenic temperature. For example, studies on the indium-sapphire interface (Neeper and Dillinger, 1964; Wolfmeyer, Fox, and Dillinger, 1970; Papk and Narahara, 1971; Schmidt and Umlauf, 1976), prepared by either vapor deposition or ultrasonic soldering, showed that the measured ITR for different samples varied significantly, depending on the details of the sample preparation process and the corresponding interfacial conditions. Similar results were also observed in the lead-sapphire interface (Nitsche and Schumann, 1980) and the aluminum-sapphire interface (Sahling *et al.*, 1981). This is because the AMM does not consider the atomic structure of the interface, so the AMM is no longer able to predict ITR even at cryogenic temperatures. For details of interface condition affecting ITR and validation of the AMM, please see Secs. III.A.4 and III.A.5.

Matsumoto, Reynolds, and Anderson (1977) polished epoxy-metal interfaces to ensure perfect physical contact and found that the ITR measured at the epoxy-metal interface agreed well with the AMM below 100 mK. Later Swartz and Pohl (1987) reported a measurement of the solid-solid ITR on a metal-dielectric interface with the temperature between 1 and 300 K, from which the ITR was found to be in agreement with the prediction of the AMM below $T = 30$ K with ITR following T^{-3} behavior. Above 30 K, ITR deviated from the AMM and was attributed to the possible disordered layers near the interface. However, recent results indicated that the

assumption of specular transmission could break down even for a perfect interface above 30 K (Costescu, Wall, and Cahill, 2003). The AMM does not work for interfaces with imperfection, defect, and disorders, even for temperatures as low as 1 K, and the DMM is more appreciated (Neeper and Dillinger, 1964; Wolfmeyer, Fox, and Dillinger, 1970; Swartz and Pohl, 1989).

The DMM somehow provides good agreement between the experimental results and theory (Freedman *et al.*, 2016; Jeong *et al.*, 2016), although this model can provide only mode-averaged ITC and cannot provide details on vibration interactions and comprehensive insight into the experiment data. By varying the phonon's cutoff frequency in the film while keeping the same substrate, Cheaito *et al.* (2015a) managed to mimic the accumulation function of the ITC and provided the framework to extract an averaged frequency-dependent phonon transmissivity. This method provides a platform for analyzing the spectral phononic contribution to the ITC. Hua *et al.* (2017) presented the experiment, by measuring the phonon transmission coefficient in the Al/Si interface, to demonstrate the failure of the DMM. This experiment highlights the phonon mode contribution to the ITR. This is a new and unique method for analyzing TDTR data, as previous works could provide only a phonon mode-averaged ITR. Figure 12 shows the spectrally resolved heat flux extracted from the TDTR data. At frequencies below 4 THz, their results demonstrated that these low-frequency phonon modes contribute more to heat flux than that in the DMM due to an underestimated phonon transmission coefficient in the DMM. In other words, the DMM cannot fully capture the long-wavelength contribution to ITR. However, the phonon contribution above 4 THz is overestimated in the DMM. Therefore, their results showed that, due to an overestimated contribution at high frequency and an underestimated contribution at low frequency, the agreement between the mode-averaged calculation from the DMM and the experimental result on the metal-dielectric interface is probably coincidental.

Stevens, Smith, and Norris (2005) plotted the relation between ITC, calculated using the DMM, and the Debye

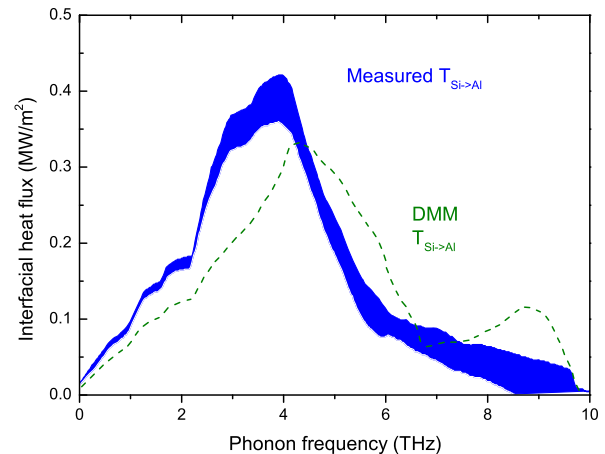


FIG. 12. Spectral heat flux from experiment and the DMM across the interface. From Hua *et al.*, 2017.

temperature, in which the DMM was shown to either overestimate or underestimate ITC in some experimental results, depending on the Debye temperature on both sides of the interface. They proposed that the ratio of the Debye temperature gives a quantitative criterion of the different phonon states on the two sides of the interface. However, studies on ITC in the literature to date have indicated that quantities of materials such as sound velocity, Debye temperature, and elastic modulus should not be used to directly calculate ITC; for more details please see Sec. III.A.6. Furthermore, this discrepancy is also probably due to substrate damage or poor interface quality, as previously suggested (Swartz and Pohl, 1989; Stoner and Maris, 1993), while Costescu, Wall, and Cahill (2003) found that substrate damage and poor contact are not the issue in interfaces with low mismatch materials. Huberman and Overhauser (1994) and Lu, Wang, and Ruan (2016) stressed that the coupling of electrons on the metal side and phonons on the dielectric side cannot be ignored, while Lyeo and Cahill (2006) and Hohensee, Wilson, and Cahill (2015) concluded that the electron-phonon coupling at the interface does not contribute significantly to the thermal transport at the interface. The contribution of electron-phonon coupling is discussed in Sec. III.B. Zhong *et al.* (2021) pointed out that both the elastic modulus and the atomic mass should be matched simultaneously to obtain the ITC, indicating that the local phonon DOS (Duda *et al.*, 2012) and coordination number density (Zhong *et al.*, 2021) should also be considered and that quantities of materials such as the sound velocity, the Debye temperature, and the elastic modulus alone are not enough to calculate the ITC.

Inelastic scattering is another important factor that should be considered in theory, especially at high temperatures (Sääskilähti *et al.*, 2014). If only the elastic-scattering process is considered, i.e., a phonon from one side of the interface with a frequency ω can be scattered only into a phonon mode with the same frequency on the other side, the ITC predicted by the DMM will be a constant at high temperatures, near or exceeding the lower Debye temperature of interfacial materials, since the Debye temperature is proportional to the phonon cutoff frequency. However, Stoner and Maris (1993) found that the ITC in the Pb/diamond interface is more than 1 order of magnitude higher than the radiation limit, which is the maximum ITC for thermal transport by the elastic process involving two phonons, i.e., one phonon on each side of the interface. Lyeo and Cahill (2006) found that for Pb or Bi on hydrogen-terminated diamond, the measured ITC exceeds the radiation limit and increases almost linearly with increasing temperature in the range $50 < T < 400$ K. Similar results were also found in various interfaces, such as Al/Al₂O₃ (Stoner *et al.*, 1992; Stoner and Maris, 1993), Ti/Al₂O₃ (Stoner *et al.*, 1992), Rh/Al₂O₃ (Swartz and Pohl, 1987), TiN/MgO (Costescu, Wall, and Cahill, 2003), GST/ZnS:SiO₂ (Kim *et al.*, 2000), Al/O/Si (Cahill, Bullen, and Lee, 2000), and Au/Si (Dechaumphai *et al.*, 2014). To reduce such a discrepancy, the inelastic-scattering process should be incorporated into the DMM (Hopkins, 2009; Hopkins and Norris, 2009; Duda, Hopkins *et al.*, 2010; Hopkins, Beechem *et al.*, 2011). For instance, Hopkins (2009) developed the DMM to account for the inelastic-scattering process involving multiple phonons

in the calculation of ITC between two solids. For five different interfaces, Hopkins (2009) demonstrated that the calculation results of ITC by the developed new model show better agreement in value and trend with the experimental data than the traditional DMM, which assumes elastic scattering only.

3. Lattice mismatch

For realistic interfaces composed of dissimilar materials, lattice mismatch typically exists at the interface due to the different lattice constants and lattice structures of the two materials. To avoid lattice mismatch, simplifications are often used, such as the use of two LJ solids with only mass mismatch (Merabia and Termentzidis, 2012) or imposition of the same lattice constant even for dissimilar materials (Landry and McGaughey, 2009; Liang, Sasikumar, and Koblinski, 2014; Polanco and Lindsay, 2019), which will cause unrelaxed strain at the interface. Therefore, the strain effect is important for interfacial thermal transport. By using the NEGF and first-principles calculations, Chen, Huang, and Kumar (2013) studied the phonon transmission in the Cu/graphene/Cu sandwiched heterostructure. They found that a small tensile strain of $\sim 1.6\%$ to graphene lattice can result in a substantial increase in h_I of $\sim 59\%$ because of the significantly enhanced interaction between Cu and graphene. Ong, Zhang, and Zhang (2016) found that the application of longitudinal tensile strain to a single-layer graphene-hexagonal boron nitride lateral heterostructure can result in a substantial enhancement in h_I of 25% at room temperature, mainly due to the improved alignment of the flexural acoustic phonon branches, despite the reduction in phonon group velocity for longitudinal acoustic and transverse acoustic branches. In addition, Liu *et al.* (2018) studied the effect of tensile strain on thermal transport across a graphene-phosphorene in-plane heterojunction using NEMD simulations. They found that the h_I of an armchair heterojunction abnormally increases with the tensile strain, while the zigzag heterojunction exhibits the opposite trend. This is because the application of strain results in the shift of the vibrational DOS spectrum in each segment (Chen, Walther, and Koumoutsakos, 2014), causing the increase and decrease in the overlap of the DOS spectrum between the two segments (Liu *et al.*, 2018).

To handle the lattice mismatch at a realistic interface, Li and Yang (2012a) proposed integrating MD simulations with the NEGF method to study the phonon transmission across a lattice-mismatched interface. MD simulation is used to simulate the reconstruction of the atomic structure near the interface, while the recursive NEGF method is then used to compute the frequency-dependent phonon transmission coefficient. The calculation results of Li and Yang (2012a) for the Si/Ge interface show that the lattice mismatch leads to an increase of lattice disorder and a decrease of adhesion energy, which in turn suppress the phonon transmission coefficient and thus reduce h_I across the lattice-mismatched interface. With the integration with MD simulation, their approach can also be applied to studying other complex effects involving interface reconstruction such as defect and disorder.

4. Interfacial coupling strength

The interaction strength between two solids is another important factor governing the interfacial thermal transport. This has been systematically studied based on the 1D atomic chain model, which is helpful for understanding the heat conduction mechanisms across solid-solid interfaces. For two harmonic chains coupled with a harmonic spring, Zhang *et al.* (2011) demonstrated via NEGF calculations that with the increase of interfacial coupling strength, the ITC first increases and then decreases. They found that a maximum ITC can be achieved when the interfacial spring constant is equal to the harmonic average of two spring constants in the semi-infinite atomic chains. When the nonlinear interaction to the interface is introduced, the effective harmonic coupling constant at the interface is proportional to the nonlinear interaction strength, and maximum ITC occurs when the effective harmonic coupling constant is equal to the harmonic average of the two spring constants (Zhang, Thingna *et al.*, 2013). Lu, Xiong *et al.* (2020) further considered two nonlinear chains coupled with a harmonic spring and found via NEGF calculations that an optimized interfacial coupling strength, which corresponds to a minimum ITR, agrees qualitatively with the effective linear coefficient derived from the self-consistent phonon theory and effective phonon theory when the nonlinearity in the atomic chain is weak.

For realistic materials, Mao *et al.* (2013) studied phonon thermal transport across a variety of graphene-metal interfaces based on the NEGF method and first-principles calculations. Their calculation results revealed that, compared to the physisorbed interface, the chemisorbed interface generally has a lower ITR due to stronger interfacial bonding and smaller interlayer separation, which is consistent with the experimental result (Schmidt *et al.*, 2010). Moreover, the different bonding strength at the interface also results in the distinct length dependence of the ITR (Chen, Zhang, and Li, 2012). In addition, Jin *et al.* (2012) studied the ITC of interfaces involving organic semiconductors. Their measurement results show that the ITC of the organic-inorganic interface scales with the bonding strength, which is further supported by MD simulation. In comparison, they further showed that the ITC of the organic-organic interface is not sensitive to the bonding strength, due to the large overlap of the phonon DOS in the low-frequency regime.

There are some counterintuitive effects that have a complex impact on thermal transport across solid-solid interfaces. In homogeneous dielectric materials, thermal conductivity is proportional to the phonon MFP, and thus those mechanisms that cause the scattering of phonons, such as anharmonicity, defect, and roughness, will lead to a reduction of lattice thermal conductivity. However, this is not the case for interfacial thermal transport.

Take the anharmonic phonon-phonon interaction, for instance. Landry and McGaughey (2009) found via NEMD simulations that the ITR at the Si/Ge interface decreases when the temperature increases above 400 K. In other words, heat transport across the Si/Ge interface is enhanced at high temperatures. Similar behavior has been found in the 1D atomic chain model in which the ITC increases with an increase in the nonlinear interaction strength for a weak

linearly coupled interface (Zhang, Thingna *et al.*, 2013). This is the complete opposite of the case of crystalline materials, whose thermal conductivity typically decreases with an increasing temperature due to the enhanced phonon-phonon scattering at high temperatures (Chen, Zhang, and Li, 2010c; Wei, Wang *et al.*, 2014; Feng, Lindsay, and Ruan, 2017; Aiyiti *et al.*, 2018). By decomposing the spectral heat flux into elastic and inelastic contributions, Sääskilähti *et al.* (2014) demonstrated explicitly in a mass-mismatched solid-solid interface via NEMD simulation that inelastic phonon scatterings arising from the anharmonic interaction actually facilitate the heat transport across the interface. Their simulation results showed that high-frequency phonons above the cutoff frequency of the heavy-mass solid segment make a negligible contribution to the spectral ITC at low temperatures, as they cannot be transmitted across the interface via elastic scattering (i.e., there is the same frequency at both sides). However, their contribution to the spectral ITC is enhanced with an increasing temperature, as these high-frequency modes can be transmitted at high temperatures by evanescent modes across the interface due to the inelastic three-phonon scattering process. As a result, the total ITC increases with temperature, and the contribution of inelastic scattering also increases and becomes non-negligible at high temperatures. The same enhancement effect of the ITC by the anharmonic phonon-phonon interaction was also reported in the Si/CoSi₂ interface using NEGF calculations (Sadasivam *et al.*, 2017), and in the graphene/h-BN interface with MD simulations (Ren *et al.*, 2021).

An insertion layer and ion implantation provide another effective approach by altering, or more precisely matching, the phonon vibrational DOS between the two materials composing the interface (Stevens, Zhigilei, and Norris, 2007; English *et al.*, 2012; Duda *et al.*, 2013; Jeong *et al.*, 2016; Polanco *et al.*, 2017; Yalamarthy *et al.*, 2018; Rastgarkafshgarkolaei *et al.*, 2019). Materials with Debye temperatures similar to the substrate with strong adhesion are potential candidates (Stevens, Smith, and Norris, 2005; English *et al.*, 2012). For example, Gorham *et al.* (2014) demonstrated that ion irradiation of a native oxide interface across the Al/native oxide/Si interface by creating a region with an average vibrational mode of the two materials composing the interface can increase the ITC due to the change in the acoustic impedance of the surface. Their experiments demonstrated that under specific conditions a defected interface can have a lower ITR than a more perfect interface (Hopkins, 2013). By inserting few-nanometer Ca_{0.5}Sr_{0.5}TiO₃ in the CaTiO₃/SiTiO₃ interface, Giri *et al.* (2021) emphasized the importance of the vibrational matching across interfaces. With this perfectly phonon-matched insertion layer, phonons with a long wavelength transport ballistically across the interface with the ITR remaining constant when the thickness of the Ca_{0.5}Sr_{0.5}TiO₃ insertion layer changing from a monolayer to 10 nm. Duda *et al.* (2013) observed an enhancement of the ITC by a factor of 4 at room temperature through the inclusion of a Ti adhesion layer in the Au/Si interface. Later Jeong *et al.* (2016) carried out a similar experiment on the Au/sapphire interface using Cu and Cr as adhesion layers. The experiment demonstrates that an adhesion layer of Cu or Cr with 1 nm of thickness is sufficient to improve the ITC by a factor of 2 or 4,

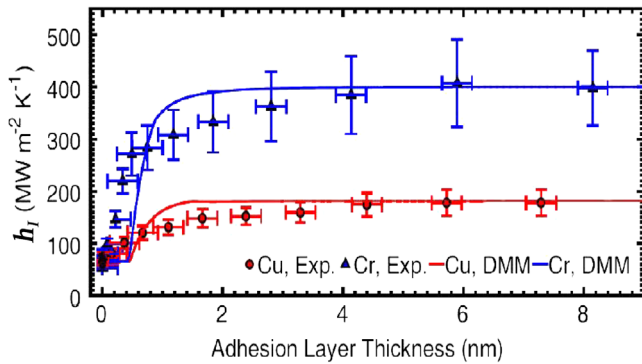


FIG. 13. Experimental results of ITC with increasing adhesion layer thickness in a Au/sapphire interface. The solid lines indicate the results predicted by the DMM. From Jeong *et al.*, 2016.

respectively (Fig. 13). The calculated ITC using the DMM at 300 K shows a plateau for an adhesion layer thicker than 2 nm, which agrees well with the experiment. Note that special care needs to be taken to reduce possible oxidization when inserting these metal layers since chemical reactions of metal impede phonon transport across the interface (Freedy *et al.*, 2018, 2020; Olson *et al.*, 2018; Aller *et al.*, 2019). On the other hand, Freedy *et al.* (2019) reported that, when the inserted oxidized layer is thin enough, this thin oxidized layer can be used to enhance electronic properties and has no negative impact on thermal transport across the Ti/TiO_x/MoS₂ interface. The fact that the DMM model can capture the experiment results indicates that the phonon-phonon interaction is a dominant mechanism in increasing the ITC, rather than the enhancement of electron-phonon coupling on the metal side of the interface; see Sec. III.B for more discussions and debates.

Using near-equilibrium plasma-enhanced chemical vapor deposition, Liu *et al.* (2019) realized direct conformal growth of 2D hexagonal boron nitride on the SiO₂/Si substrate, from which the WSe₂/BN/SiO₂ interface can be studied. The thermal dissipation efficiency can be greatly improved compared to that in the WSe₂/SiO₂ interface since boron nitride provides a bridge for the vibrational spectrum across the interface. MD simulation results suggest that, due to the broadened vibrational frequency distribution (Lindsay and Broido, 2011), the 2D BN layer works as an external material that can better fit the vibrational spectrum between the SiO₂ substrate and the WSe₂ layer. Therefore, the insertion of the 2D BN layer can reduce the ITR, regardless of the substrate roughness. Similar results were also reported for the graphene/BN/SiO₂ interface, where Liu *et al.* (2020) demonstrated that ITR decreases by more than 77%, while the saturated power density of graphene FETs increases by twofold to threefold when the BN layer is inserted into the graphene/SiO₂ layer.

The vibrational overlap and interfacial bond strength between the organic self-assembled monolayer (SAM) molecules and the substrates have been leveraged to tune the ITC. Losego *et al.* (2012) used a combination of TDTR and the picosecond acoustic technique to link the changes in bonding strength with ITC at the Au/SAM interfaces. A correlation between bonding and ITC at the atomic level is demonstrated by gradually changing interfacial interaction from a weak van

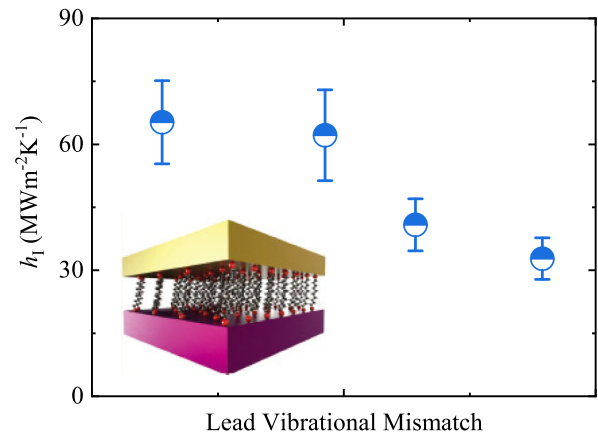


FIG. 14. Measured ITC vs vibrational mismatch between metals in a metal-SAM-metal junction. From Majumdar *et al.*, 2015.

der Waals interaction to covalent bonding via the SAM between Au and quartz. An enhancement of 80% is observed. Similar results were also demonstrated by Majumdar, Malen, and McGaughey (2017) in the Au/C₁₀S₂:C₁₁S/Au interface by changing the bonding. They further presented a measurement of the ITC in the SAM junction between two metal leads (Au, Ag, Pt, or Pd) with mismatched phonon spectra, as shown in Fig. 14 (Majumdar *et al.*, 2015). The ITC obtained from FDTR is $\sim 65 \pm 7 \text{ MW m}^{-2} \text{K}^{-1}$ in a fully matched Au/SAM/Au junction and decreases with the decreasing lead vibrational mismatch to $\sim 36 \pm 3 \text{ MW m}^{-2} \text{K}^{-1}$ in the Au/SAM/Pd junction. O'Brien *et al.* (2013) used a strongly bonding organic nanomolecular monolayer (NML) and obtained a fourfold increase in ITC that is as high as $430 \text{ MW m}^{-2} \text{K}^{-1}$ in the Cu/SiO₂ system. MD simulation indicates that this enhancement is due to strong NML–silicon and NML–Cu bonds that facilitate efficient heat transfer at the interface. Furthermore, the large NML vibrational DOS at low frequencies $< 2 \text{ THz}$ forms a broad band and vibrational overlap between that in SiO₂ and that in metal Cu, which leads to efficient phonon transmission. These results underscore the importance of interfacial bond strength and vibrational mismatch as an effective tool to describe and tailor the ITC in a variety of material systems.

Interfacial stiffness of the bonding between two materials plays an important role in controlling the ITC via the application of static pressure or the change of the interfacial chemical bonding strength (Collins, Chen, and Chen, 2010; Shen *et al.*, 2011; Kaur *et al.*, 2014; Giri *et al.*, 2019). In general, the spring constant that holds the atom to its equilibrium position changes by applying static pressure, which can be reflected by the shift of the maximum phonon frequency. The calculations demonstrate that the increase of maximum frequency (Giri *et al.*, 2019) and the group velocities (Giri and Hopkins, 2017) under high static pressure can both contribute to the heat transfer across the interfaces. A series of works have demonstrated the ability to tune phonon transmission coefficient and tune the ITC by mechanical strain via high pressure (Hsieh *et al.*, 2009, 2011; Hohensee, Wilson, and Cahill, 2015; Wilson *et al.*, 2015) (Fig. 15). For instance, Hsieh *et al.* (2011) measured the pressure-dependent ITC of a clean Al/SiC interface and a modified Al/SiC interface with

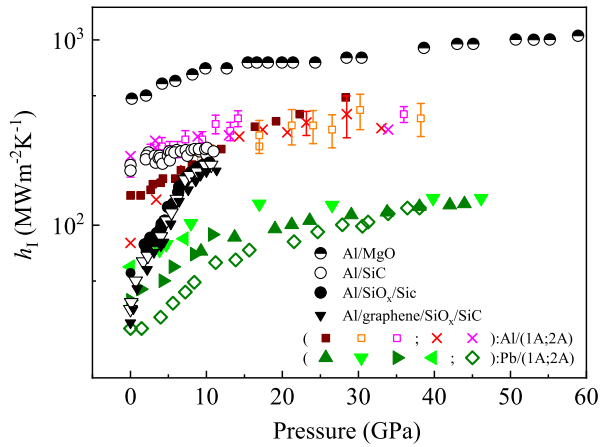


FIG. 15. Measured ITC vs pressure. From Hsieh *et al.*, 2009, 2011, and Wilson *et al.*, 2015.

weak bonding insertion layers. A weak pressure dependence was observed in the clean interface, while in interfaces with graphene or SiO₂ insertion the ITC increases linearly with pressure by nearly 1 order of magnitude. This linear increase is believed to be related to the increase of the averaged transmission coefficient. With high pressures (i.e., > 8 GPa), these weak interfaces with insertion layers approach the high ITC value of a strongly bonded and clean Al/SiC interface. Wilson *et al.* (2015) characterized the ITC of two strongly bonded interfaces, SrRuO₃/SiTiO₃ at ambient pressure and Al/MgO at high pressure up to 60 GPa, and found that both interfaces have unusually high ITC values that are highest in the metal-dielectric interface. The measured ITC in the Al/MgO interface under 60 GPa is approximately 1.1 GW m⁻² K⁻¹, which is 40% of the maximum ITC predicted by the DMM in this system. These works demonstrate that weak interfacial bonding can severely impede interfacial heat flow by lowering the probability of a phonon being transmitted to the other side of interface. Hohensee, Wilson, and Cahill (2015) carried out an experiment between metals and diamond and found that high pressure can significantly extend the metal phonon DOS to higher frequencies and overlap with that in diamond, resulting in pressure-dependent ITC. The measured ITC increases weakly and saturates to similar values at high pressure. They argued that inelastic scattering at the interface could be important. For more discussions of inelastic scattering, please see Sec. III.A.2.

Surface functionalization provides an alternative approach to tailor the ITC. Foley *et al.* (2015) functionalized graphene with oxygen, fluorine, and nitrogen groups with a low-energy electron-beam plasma to tune the heat transfer at the Au/graphene interface. The oxygen and nitrogen groups can effectively improve the ITC by as much as 40% due to the increase of surface energy, which is similar to the results observed by Zhang, Zhao *et al.* (2013) and Zhang *et al.* (2017). Functionalization molecules at graphite surface are also found to show distinct interfacial thermal transport behaviors on the graphite/SiO₂ interface, due to the enhanced phonon transmission, that was supported by the MD simulation (Han *et al.*, 2016). Hopkins *et al.* (2012) metalized plasma-functionalized graphene and measured the ITC at the

Al/graphene/SiO₂ interface. The adsorbates on the graphene surface are found to influence the ITC of Al/SiO₂ by nearly twofold due to changes in the bonding strength between Al and graphene (Han *et al.*, 2016). A similar effect is also observed in the Al/graphene/SiC interface under static pressure (Hsieh *et al.*, 2011).

5. Roughness and disorder

A perfect interface is rare in the real world. Therefore, it is important to understand the influences of surface disorder on the interfacial modes that modulate the electron-phonon and phonon-phonon interactions at the interface.

Roughness typically reduces the thermal conductivity in crystalline materials (Hochbaum *et al.*, 2008; Evans, Hu, and Koblinski, 2010). The imperfection at the interface (such as roughness or atomic mixing) could alter the ITC by changing the vibration properties at the interface (Zhou *et al.*, 2013; Liang, Sasikumar, and Koblinski, 2014; Freedman *et al.*, 2016).

Pernot *et al.* (2010) demonstrated that the ITC can be reduced by controlling interface roughness through quantum-dot implanting. By engineering a set of individual phonon-scattering nanodot barriers, they managed to accurately control the thermal conductivity of single-crystal SiGe superlattice and the ITR between layers. ITR is observed to increase from 2.5×10^{-9} to 4×10^{-9} m² KW⁻¹ with an increasing layer thickness from ~3.5 to ~13 nm. Similarly, Hopkins, Duda *et al.* (2011) synthesized a series of Ge_xSi_{1-x} quantum dots by epitaxial self-assembly on the Si surface and found that quantum dots with a root mean square (rms) roughness larger than 4 nm reduce the ITC at the Si interface by a factor of 1.6 due to localized phonon attenuation beyond vibrationally mismatched interface. Chemical etching provides another effective way to control surface roughness, although precise control is not possible. Hopkins, Phinney *et al.* (2010) and Duda and Hopkins (2012) carried out chemical etching before metal thin-film deposition and systematically demonstrated variation of the ITC by manipulation roughness on the Al/Si interface. Figure 16 plots the room-temperature ITC as a function of rms roughness while comparing the experimental data with the aforementioned roughness DMM model. The ITC has a similar relationship with rms roughness regardless of the preparation process, either chemical etching or quantum-dot roughening.

Recent experimental works have demonstrated that specifically designed nanopillar arrays with a characteristic size ranging from ~100 nm to ~1 μm can enhance ITC by increasing contact areas, which is in sharp contrast to nanostructures with a roughness of several nanometers (Zhou *et al.*, 2013; Liang, Sasikumar, and Koblinski, 2014; Freedman *et al.*, 2016). By implanting Si nanopillars into the Al/Si interface, Lee *et al.* (2016) observed an enhancement of ~88% in ITC measured with TDTR. Park, Kodama *et al.* (2017) and Park, Sood *et al.* (2017) carried out a similar experiment on the Al/SiO₂ interface by interdigitating Al pillars with a characteristic length ranging from 100 to 800 nm. They showed that the effective ITC of a thin layer with a thickness of ~65 nm increases with a decreased pillar-to-pillar distance and the ITC can be tailored up to twofold.

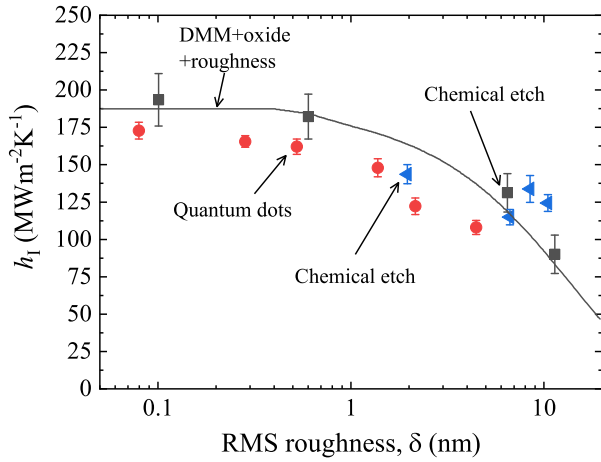


FIG. 16. Room-temperature ITC predicted by DMM (solid line) and measured by experiment for the Al/Si interface or $\text{Ge}_x\text{Si}_{1-x}/\text{Si}$ interface with the quantum-dot nanostructure as a function of roughness rms. From Hopkins, Phinney *et al.*, 2010, Hopkins, Duda *et al.*, 2011, and Duda and Hopkins, 2012.

By using the NEGF method and first-principles calculations, Tian, Esfarjani, and Chen (2012) demonstrated that interfacial roughness can be used to enhance the ITC at the Si/Ge interface. In their work, the roughness is introduced by randomly exchanging Si and Ge atoms in regions near the interface with a certain thickness so that a mixture layer of Si/Ge near the interface is formed. They showed through the DOS analysis that the mixture layer actually serves to bridge the frequency gap between Si and Ge, causing a large overlap in DOS compared to the abrupt interface. As a result, the phonon transmission coefficient can be enhanced for the intermediate frequency phonons, thereby giving rise to the enhanced ITC when the interfacial roughness is small. Similar enhancement of the ITC induced by roughness has also been reported in other theoretical works with different approaches (Kazan, 2009; Merabia and Termentzidis, 2014; Hahn, Puligheddu, and Colombo, 2015; Jia *et al.*, 2016). In contrast to the overlapping DOS that increases phonon transmission, a further increase in the thickness of the mixture layer reduces the phonon transmission due to the diffusive scattering. Because of these two competing mechanisms, the NEGF calculation results revealed that there is an optimal roughness thickness with maximum ITC. A similar nonmonotonic dependence of ITC on the roughness thickness has also been reported with MD simulations (Hahn, Puligheddu, and Colombo, 2015). A discussion of the effect of vibrational overlapping and the phonon frequency bridge by insertion layer and ion implantation can be found in Sec. III.A.4.

The mixture layer of Tian, Esfarjani, and Chen (2012) actually gave rise to the localized interfacial modes that facilitate the heat conduction across the solid-solid interface. These interfacial modes can also be induced by defect or disorder at the interface. For instance, Liu, Zhang, and Zhang (2016) found via NEMD simulations that topological defects at graphene-hexagonal boron nitride interface can enhance the ITC. By analyzing the stress field and the vibrational DOS, they found that the topological defects result in a nonuniform stress distribution, which softens the abrupt change in the

stress field at the interface and gives rise to interfacial modes that have more overlap in the DOS than in the abrupt interface. This mechanism is the same as the roughness induced enhancement of ITC reported by Tian, Esfarjani, and Chen (2012). A similar effect for enhanced ITC via interfacial defect was also reported in a recent study on amorphous interface by Giri *et al.* (2018) in which an ultrahigh ITC approaching $1 \text{ GW m}^{-2} \text{ K}^{-1}$ was discovered for the amorphous interface. More discussion of thermal transport across the amorphous interface can be found in a recent review by Giri and Hopkins (2020).

6. Summary

The underlying mechanism of phonon transport that determines the ITC of the solid-solid interface is still an open question. There is no generic theory that can explain all experimental observations simultaneously. The main discrepancies between the current theories and experiments are as follows:

- (i) The measured values of ITC at room temperature are in a narrow range: approximately from 10 to $800 \text{ MW m}^{-2} \text{ K}^{-1}$. In contrast, the AMM and DMM give a much wider range. For the lower bound of ITC, a typical example is the Pb/diamond interface. The Debye temperature of Pb is 20 times smaller than the Debye temperature of diamond. Such a large difference results in a small value of the calculated ITC below $2.5 \text{ MW m}^{-2} \text{ K}^{-1}$. It is 1 order of magnitude smaller than the measured value of 31 or $60 \text{ MW m}^{-2} \text{ K}^{-1}$ (Stoner *et al.*, 1992; Hohensee, Wilson, and Cahill, 2015). Stoner and Maris (1993) pointed out that inelastic phonon scattering due to anharmonicity provided additional channels for heat transfer. As a result, strong temperature dependence should be obtained. However, the temperature dependence of ITC at room temperature is weak. Therefore, the importance of inelastic phonon scattering on the lower limit of ITC is questionable. For the upper bound value, the measured value can hardly exceed $1 \text{ GW m}^{-2} \text{ K}^{-1}$. By choosing a unit transmission probability, Wilson *et al.* (2015) gave a rough estimation of the upper limit as follows:

$$h_I^{\max} = \frac{1}{4} \sum_{\lambda} \int v_g(\mathbf{k}, \lambda) c_{\omega_{\lambda}} d\omega_{\lambda}, \quad (50)$$

where $c_{\omega_{\lambda}}$ is the heat capacity per frequency. Its value is of the order of $\text{GW m}^{-2} \text{ K}^{-1}$ and is linearly correlated with $v_D C_V$, where v_D is the Debye velocity and C_V is the volumetric heat capacity (Wilson *et al.*, 2015). Typical values of $v_D C_V$ are in the range of $5\text{--}20 \text{ GW m}^{-2} \text{ K}^{-1}$, which is 1 to 2 orders of magnitude larger than the measured ITC. Wilson *et al.* (2015) pointed out that h_I^{\max} can be approached by fabricating clean and strongly bonded interfaces. The question is, can one really achieve h_I^{\max} even though the interface is perfect and strongly bonded? If not, is

there another theoretical upper bound that is below h_I^{\max} ?

- (ii) The key parameters determining the ITC are sound velocities in both the AMM and the DMM. Besides sound velocity, which parameters are decisive? Stevens, Smith, and Norris (2005) tried to compare the ITC and the Debye temperature ratio of two materials. The ITC was found to be weakly related to the Debye temperature ratio, but no conclusive trend was found. This was confirmed by the MD simulations of Duda *et al.* (2012). A qualitatively positive relation between ITC and the ratio of the elastic modulus between the two materials was proposed by Giri and Hopkins (2020). They claimed that this is due to a better overlap in the vibrational DOS of the materials. However, this argument was challenged by their own experimental results (Koh *et al.*, 2020). The room-temperature ITC values of Co/sapphire, Ru/sapphire, and Al/sapphire interfaces are close, although the ratios of the Young's modulus are 0.53, 0.73, and 0.175, respectively. Zhong *et al.* (2021) pointed out that the elastic modulus and the atomic mass should be simultaneously matched to obtain a large ITC. An energy transfer coefficient Γ_{et} is introduced to characterize the matching of both the atomic masses and the elastic modulus. Figure 17 shows that the values of Γ_{et} for Co/sapphire, Ru/sapphire, and Al/sapphire interfaces are close, which explains the experimental results well (Koh *et al.*, 2020). To sum up, studies in the literature on ITC thus far indicate that quantities of materials such as sound velocity, Debye temperature, and elastic modulus are not enough to calculate ITC. Local information about the interface should be considered, such as the local phonon DOS (Duda *et al.*, 2012) and the interfacial coordination number density (Zhong *et al.*, 2021).
- (iii) In bulk amorphous materials, disordered atomic structures should lead to a low thermal conductivity that is in the range of $0.1 - 1 \text{ W m}^{-1} \text{ K}^{-1}$. However, the ITC between two amorphous solids was found to be larger than that between two crystalline solids

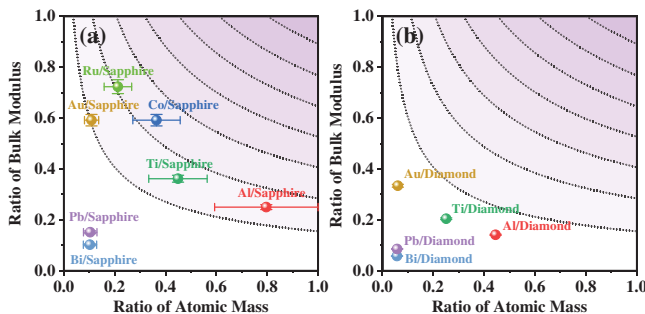


FIG. 17. Ratio of bulk modulus and ratio of atomic mass for (a) metal-sapphire interfaces and (b) metal-diamond interfaces. The contour lines are the guides for the eye. From Zhong *et al.*, 2021.

(Fong *et al.*, 2016; Kimling *et al.*, 2017; Giri *et al.*, 2018). This feature implies that disorder is helpful for improving energy transfer at the interface. Zhong *et al.* (2021) proposed a model considering the interface as a thin layer of amorphous material. They introduced a quantity termed interfacial coordination number density (n_c) to characterize the energy transfer channels per unit area (Xi *et al.*, 2020). The calculated n_c of the interface between two amorphous solids is larger than the interface between two crystalline solids. This finding successfully explains why the amorphous interface can lead to large ITC.

B. Electron-phonon coupling across the metal-dielectric interface

The most common interface with multiple heat carriers is the metal-dielectric interface. Both electrons and phonons are heat carriers in a metal, while there are only phonons in dielectrics. A thermal resistance network such as that shown in Fig. 7(a) should be considered; in the figure, Carriers 1a and 1b are an electron and a phonon in a metal, respectively, and Carrier 2 is a phonon in a dielectric. Energy transfer between Carriers 1b and 2 is determined by the phonon transport across the metal-dielectric interface, which was discussed in Sec. III.A. The energy transfer channel Carrier 1a \rightarrow Carrier 2 is determined by the electron-phonon coupling across the interface. The indirect energy transfer channels Carrier 1a \rightarrow Carrier 1b \rightarrow Carrier 2 or Carrier 1b \rightarrow Carrier 1a \rightarrow Carrier 2 are determined mainly by the electron-phonon coupling inside the metal.

The effect of conducting electrons on ITC across metal-liquid interfaces was reviewed by Swartz and Pohl (1989). The role of electron-phonon coupling in ITC across metal-dielectric interfaces was reviewed by Shi, Tang *et al.* (2018). We review the electron-phonon coupling inside a metal as an indirect channel and the electron-phonon coupling across an interface as a direct channel in this section. A detailed theory was presented in Sec. II.C.

1. Indirect electron-phonon coupling channel

The effect of electron-phonon coupling within a metal side on the ITR was studied by Majumdar and Reddy (2004). Additional thermal resistance was found in series with the thermal resistance of phonons. In the TTM, this thermal resistance was calculated as $R_{e-ph} = 1/h_{e-ph} = (G_{e-ph}\kappa_{ph})^{-1/2}$, as shown in Eq. (40). The typical value of R_{e-ph} at room temperature was found to be $10^{-8} \text{ m}^2 \text{ KW}^{-1}$, which is comparable to the value of the measured ITR of the metal-dielectric interface. Therefore, the contribution from the indirect heat transfer channel should not be ignored in metal-dielectric interfaces. In contrast, this additional thermal resistance is negligible in metal-liquid interfaces because the ITR of the metal-liquid interface is much larger. Singh, Seong, and Sinha (2013) used Fermi's golden rule to calculate the thermal resistance due to electron-phonon coupling in the metal where the deformation potential was considered. The amplitude of the deformation potential was obtained by fitting the electrical conductivity of the bulk metal. Sadasivam,

Waghmare, and Fisher (2015, 2017) used the first-principles method to calculate the phonon linewidth due to electron-phonon scattering in bulk metal silicide. The spectral Eliashberg function, which quantifies the strength of the electron-phonon coupling, was computed from the phonon linewidth. Further studies showed that the electron-phonon coupling constant can be changed by the chemistry of the interface (Hopkins and Norris, 2007b; Hopkins, Kassebaum, and Norris, 2009; Guo *et al.*, 2012; Zhou *et al.*, 2019; Lu, Wang *et al.*, 2020; Olson *et al.*, 2021).

2. Direct electron-phonon coupling channel

The contribution from the direct heat transfer channel due to electron-phonon coupling at the interface was proposed experimentally in the metal-liquid helium interface (Challis, Cheeke, and Bates, 1968). The electrons in the metal are suggested to interact with the surface wave that is generated by the incident phonons from the liquid side (Pollack, 1969). This coupling could provide a channel in addition to heat transfer across the interface. In other words, the thermal resistance due to this channel (R_{e-ph}^{direct}) is parallel to the phonon transport. Schmidt and Umlauf (1976) measured the ITR of the indium-sapphire interface and found a sudden reduction in ITR when indium changed from the superconducting state to the normal state by applying a magnetic field. The reduction was caused by electrons. At a higher magnetic field when indium is in normal state, a weak magnetic field dependence of ITR appears and is believed to be connected with the strong magnetic field dependence of ITR at the gallium-helium interface (Wagner, Kollarits, and Yaqub, 1974).

Theoretically, Huberman and Overhauser (1994) calculated the electron-phonon coupling at the metal-insulator interface when the joint vibrational modes near the interface were considered. They assumed that the electrons in metal are free and that the joint modes decay exponentially with the distance from the interface, where the decay length is twice of the phonon MFP. The calculated R_{e-ph}^{direct} of the Pb/diamond interface was $3.2 \times 10^{-8} \text{ m}^2 \text{ KW}^{-1}$. This value is close to the experimentally measured one and is much smaller than the calculated thermal resistance of the phonon transport. Lu, Wang, and Ruan (2016) modified Huberman and Overhauser's model by restricting the electron-phonon coupling in an interfacial reconstruction region. Sergeev (1998) proposed a model for calculating ITR due to the inelastic electron-boundary scattering in the same way as the inelastic electron-impurity scattering. R_{e-ph}^{direct} was found to be proportional to the electron-phonon relaxation time. Mahan (2009) proposed another electron-phonon coupling mechanism via the image charges of the vibrating ions. This model is applicable when the nonmetal is a polar crystal such as the ionic crystal. Zhang, Lü *et al.* (2013) used the nonequilibrium Green's function method to study the direct coupling between the electrons in metals and phonons in insulator by considering a simple 1D lattice model. Giri, Foley, and Hopkins (2014) used Fermi's golden rule to calculate the ITC. Sadasivam, Waghmare, and Fisher (2015, 2017) used the first-principles method to calculate the direct electron-phonon coupling strength at metal silicide-silicon interfaces. The phonon linewidth and local Eliashberg function of electron-

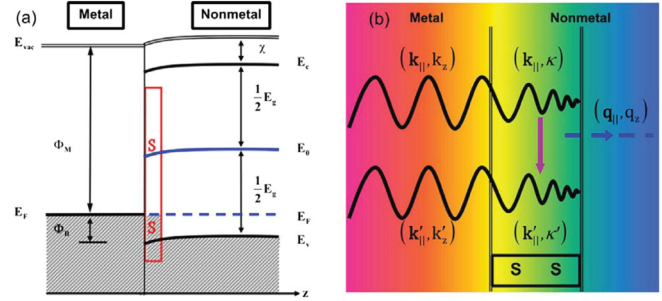


FIG. 18. (a) Schematic of the band structure and surface states at the metal-dielectric interface. (b) Phonon emission at the interface due to the surface states. From Lu *et al.*, 2016.

phonon coupling in a properly selected Si/CoSi₂ supercell was calculated. Lu *et al.* (2016) pointed out that the evanescent wave function of electrons in the metal would extend into the dielectric and form surface electron states, as shown in Fig. 18. The values of the ITR of various metal-diamond interfaces due to the electron-phonon coupling between the electrons in surface states and phonons in nonmetals were found to be in a narrow range. This finding was attributed to the pinning of the Fermi level at the interface, which successfully explains the experimental results for Au/Al₂O₃ interfaces (Zhang, Yan *et al.*, 2020) and the results for Al/BiFeO₃ interfaces (Zang *et al.*, 2022) by changing the surface charge density.

The importance of electron-phonon coupling to the ITR of the solid-solid interface is still under debate due to the lack of conclusive experimental evidence. Lyeo and Cahill (2006) measured the metal-dielectric interface with metal side to be Bi and Pb and found that the ITR values are similar. They concluded that the direct coupling of the electrons in the metal to the phonons in the dielectric substrate makes a negligible contribution to the thermal transport at the interfaces. Their results showed that thermal transport at these interfaces is driven by the phonon-phonon interaction since Bi and Pb have similar Debye temperatures but different electronic heat capacities (2 orders of magnitude in difference) near the Fermi surfaces. This finding is supported by various calculations of phonon-phonon scattering (Hopkins, 2009; Hopkins, Duda, and Norris, 2011). Singh, Seong, and Sinha (2013) also showed that electron-phonon coupling is not a major contributor to thermal transport across metal-dielectric interfaces.

C. Electron contribution across the metal-metal interface

The ITC of metal-metal interfaces was found to be much larger than that of other interfaces. Clemens, Eesley, and Paddock (1988) used the time-resolved thermoreflectance method to measure the ITC of Ni/Ti and Ni/Zr interfaces. The measured values are 0.53 and 0.43 GW m⁻² K⁻¹, respectively. Figure 19 shows the measured temperature-dependent ITC of Pt/Cu, Pt/Au, Al/Cu, Pd/Ir, and Cu/Nb interfaces (Gundrum, Cahill, and Averback, 2005; Wang and Cahill, 2012; Wilson and Cahill, 2012; Cheaito *et al.*, 2015b). The largest reported value was $14 \pm 3 \text{ GW m}^{-2} \text{ K}^{-1}$ at room temperature across the Pd/Ir interface. This is the direct consequence of electronic thermal transport. In contrast to the

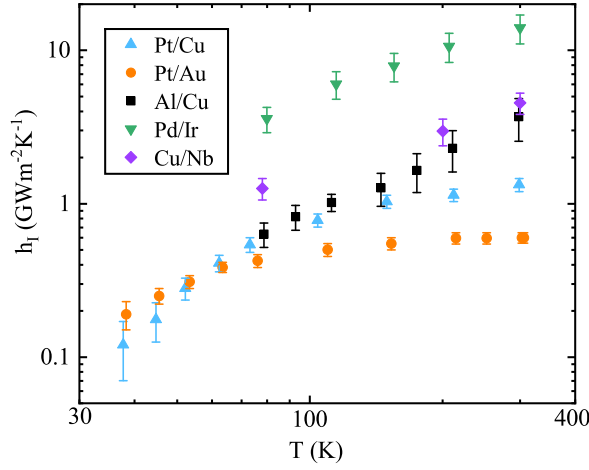


FIG. 19. The experimentally measured ITC of Pt/Cu, Pt/Au, Al/Cu, Cu/Nb, and Pd/Cr interfaces. The data are adapted from Gundrum, Cahill, and Averback (2005), Wang and Cahill (2012), Wilson and Cahill (2012), and Cheaito *et al.* (2015b).

metal-dielectric and dielectric-dielectric interfaces, the major heat carriers on both sides of the metal-metal interface are electrons. The heat current across the interface is dominated by the transmission of electrons rather than phonons. High-energy electrons near the Fermi level can easily pass through the potential barrier at the interface, while low-energy electrons are strongly reflected. The electron transmission differs significantly from the phonon transmission. Many factors that can cause notable phonon scattering, such as the surface roughness, disorder, and lattice imperfection, are not able to strongly affect the transmission of high-energy electrons (Gundrum, Cahill, and Averback, 2005; Cancellieri *et al.*, 2020).

The electronic ITC can be written as (Hopkins, Beechem *et al.*, 2010)

$$h_{I,e} = \frac{1}{4} \int_0^\infty (\varepsilon - \varepsilon_{F,1}) D_1(\varepsilon) \frac{\partial f_1(\varepsilon)}{\partial T} v_{e,1} \zeta_{e,1 \rightarrow 2}(\varepsilon) d\varepsilon, \quad (51)$$

where ε is the electron energy, $\varepsilon_{F,i}$ is the Fermi energy of the metallic material i ($i = 1, 2$), D_i is the electron DOS, $f_i(\varepsilon)$ is the electron distribution function, $v_{e,i}$ is the electron velocity, and $\zeta_{e,1 \rightarrow 2}(\varepsilon)$ is the energy-dependent electron transmission coefficient. In analogy with the DMM of phonons, Gundrum, Cahill, and Averback (2005) proposed a DMM for electron transport at interfaces by assuming that all incident electrons on the interface are diffusively and elastically scattered, while the energies of the electrons are conserved. The electron transmission coefficient is (Hopkins, Beechem *et al.*, 2010)

$$\zeta_{e,1 \rightarrow 2}(\varepsilon) = \frac{D_2(\varepsilon)[1 - f_2(\varepsilon)]v_2(\varepsilon)}{D_1(\varepsilon)f_1(\varepsilon)v_1(\varepsilon) + D_2(\varepsilon)[1 - f_2(\varepsilon)]v_2(\varepsilon)}. \quad (52)$$

At low temperatures, Eq. (52) near the Fermi energy can be simplified as $\zeta_{e,1 \rightarrow 2}(\varepsilon_F) = D_2(\varepsilon_F)v_{F,2}/[D_1(\varepsilon_F)v_{F,1} + D_2(\varepsilon_F)v_{F,2}]$, where $v_{F,i}$ is the Fermi velocity. With this simplification, the integral in Eq. (51) can be calculated analytically as follows:

$$h_{I,e} = \frac{1}{4} \frac{p_{e,1}v_{F,1}p_{e,2}v_{F,2}}{p_{e,1}v_{F,1} + p_{e,2}v_{F,2}} T. \quad (53)$$

In Eq. (53) $p_{e,i} = \pi^2 k_B^2 D_i(\varepsilon_F)/3$ is the constant of the electron heat capacity at low temperatures. The linear dependence of the ITC on the temperature agrees qualitatively well with the experimental data in Fig. 19.

Mahan and Bartkowiak (1999) studied the relation between the ITC and the electrical resistance by considering electron tunneling through a thin potential barrier at the interface. The ITC of electrons is obtained as

$$h_{I,e} = \left(\frac{\pi^2 k_B^2}{3e^2} - S_I^2 \right) \sigma_I T, \quad (54)$$

where $S_I = (\pi^2 k_B/3e) \sqrt{2m_e d^2/U_0 \hbar^2 k_B T}$ is the boundary Seebeck coefficient, and $\sigma_I = (e^2 m_e / 2\pi^2 \hbar^3) \times \sqrt{U_0 \hbar^2 / 2m_e d^2} \mathcal{T}$ is the specific electrical conductance. U_0 and d are the height and width of the potential barrier, respectively. \mathcal{T} is the tunneling probability of electrons near the Fermi energy. Equation (54) reveals the boundary form of the Wiedemann-Franz law $h_{I,e} = \mathcal{L} \sigma_I T$, with \mathcal{L} the boundary Lorenz number. The numerically calculated value of \mathcal{L} was found to be $10^{-9} - 10^{-8} \text{ W } \Omega \text{ K}^{-2}$, a value that depends on the height and width of the potential barrier (Shi, Dong *et al.*, 2018). This finding provides a simple way to roughly estimate the ITC from the electrical conductance, which is much easier to measure.

D. ITR for low-dimensional structures

The fast development of novel low-dimensional materials raised more challenges and questions for ITR. Figure 20 shows four different categories of interfaces with low-dimensional structures: (a) multilayers and superlattices (Sec. III.D.1), (b) sandwich structures with a 2D (or quasi-2D) thin layer (Sec. III.D.2), (c) nanoscale contact between two 1D nanowires or two nanotubes, and (d) 1D heterostructures inside a single nanowire (Sec. III.D.3). The ITC of these four cases are reviewed in this section.

1. Multilayers and superlattice

In multilayer structures such as those in Fig. 20(a), intuitively the contribution from interfaces to the overall thermal resistance is the sum of individual ITR. This is valid when the separations between adjacent interfaces d_i , i.e., the thickness of layers, are large enough to eliminate the interplay between the interfaces. Typically the criterion of the separation can be determined by the phonon MFP at high temperatures, the phonon wavelength at low temperatures, or the characteristic length of electron-phonon coupling in metals. When the separation is smaller than the criterion, the interplay between the interfaces should be considered. The overall thermal resistance is then no longer the simple sum of the individual ITRs.

In superlattices, the interplay includes not only the adjacent interfaces but also all interfaces due to the periodicity. Therefore, the effective thermal conductivity could differ

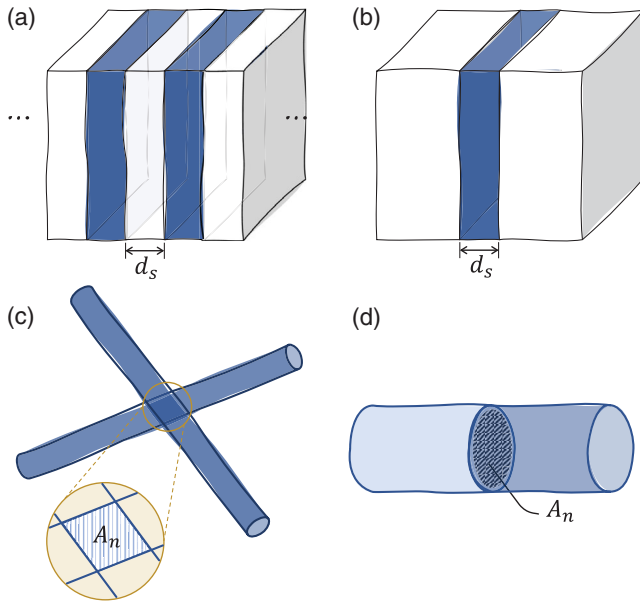


FIG. 20. Four different categories of interfaces with low-dimensional structures. (a) Multilayers and superlattices with separation distance d_s . (b) Sandwich structures with 2D (or quasi-2D) thin layers of thickness d_s . (c) Nanoscale contact between two 1D nanowires with contact area A_n . (d) One-dimensional heterostructure inside a single nanowire with cross-section area A_n .

from the intrinsic thermal conductivity and is tunable by changing the structure of the superlattice.

Wang and Li (2006) studied the effect of interfacial density on thermal conductivity. Li and Yang (2012b) and Tian, Esfarjani, and Chen (2014) studied the thermal resistance across multilayers using the Green's function method. Kazan (2011) developed a model that interpolates between the AMM and the DMM to calculate the ITC of a wurtzite-type InN/GaN superlattice. Alvarez *et al.* (2010) derived an analytical expression to calculate both in-plane and cross-plane effective thermal conductivities of superlattices. Chen and Neagu (1997), Chen (1998), and Chen and Zeng (2010) solved the phonon Boltzmann equation to calculate the effective thermal conductivity. A modified lattice dynamics model with an imaginary wave vector was proposed by Yang and Chen (2003). The existence of minimum thermal conductivity in superlattices was predicted by Simkin and Mahan (2000). Dames and Chen (2004) calculated the thermal conductivity of Si/Ge superlattice nanowires. The electron-phonon coupling effect on the thermal conductivity of metal-dielectric multilayers was studied by Ordóñez-Miranda, Alvarado-Gil, and Yang (2011).

An ideal superlattice structure has the unique features of zone folding and minigaps, and thus provides a perfect platform for studying coherent phonon transport, which has been widely studied theoretically (Simkin and Mahan, 2000; Daly and Maris, 2002; Yang and Chen, 2003; Garg and Chen, 2013; Mu *et al.*, 2015; Cheaito *et al.*, 2018; Hu *et al.*, 2018, 2019; Zhang *et al.*, 2018, 2021b, 2021c; Zhang, Hu *et al.*, 2020; Jiang *et al.*, 2021; Lu *et al.*, 2021; Peng *et al.*, 2022). When the interface is not perfect enough, the wavelike phonons can lose their phase information through the

diffusive-scattering process both at boundaries and by internal scattering processes, which makes the experimental observation extremely challenging (Lee, Cahill, and Venkatasubramanian, 1997; Capinski *et al.*, 1999; Koh *et al.*, 2009). By fixing the period thickness, the out-of-plane thermal conductivity of superlattices is found to increase linearly with the number of periods at low temperatures, suggesting a ballistic thermal transport across the superlattice (Luckyanova *et al.*, 2012; Cheaito *et al.*, 2018). Luckyanova *et al.* (2012) suggested that the ballistic thermal transport across the entire sample indicates coherent heat conduction in the superlattice structure, while Ohnishi and Shiomi (2019) argued that it is difficult to distinguish the coherent transport from the ballistic transport through this linear correlation.

A local minimum thermal conductivity in superlattices with respect to the period thickness is also regarded as a transition from diffusive to wavelike heat transport due to the competition between boundary scattering at interfaces for diffusive transport and zone folding for wavelike transport (Ohnishi and Shiomi, 2019; Chen, 2021; Zhang *et al.*, 2021a). Venkatasubramanian (2000) reported the experimental observation of the minimum thermal conductivity in $\text{Bi}_2\text{Te}_3/\text{Sb}_2\text{Te}_3$ superlattices, which was, however, interpreted as coherent backscattering of phonon waves and localization of low-frequency phonons. Ravichandran *et al.* (2014) presented evidence of the crossover from particlelike to wavelike phonon transport in epitaxial $\text{SrTiO}_3/\text{CaTiO}_3$ and $\text{SrTiO}_3/\text{BaTiO}_3$ superlattices. Similar results were also reported in Si/Ge (Chakraborty *et al.*, 2003) and GeTe/ Bi_2Te_3 superlattices (Tong *et al.*, 2017).

2. Sandwich structures with 2D or quasi-2D materials

There is one special type of system with only one or a few layers of atoms between two interfaces. It is usually called the interlayer or insertion layer. The layer is too thin to define its local temperature. One must treat the layer and the two interfaces as an entire interfacial area to define the ITR (Kosevich, 1995; Kosevich *et al.*, 2018).

The ITC across interfaces comprising 2D materials with a monolayer or multilayers [Fig. 20(b)], due to weak van der Waals interactions, is usually low. This has been intensively studied with various approaches, such as the 3ω method (Chen *et al.*, 2009; Li *et al.*, 2017; Guo, Yang *et al.*, 2019), Raman spectroscopy (Taube *et al.*, 2015; Yan *et al.*, 2016; Yalon *et al.*, 2017a, 2017b), pump-probe thermoreflectance (Koh *et al.*, 2010, 2016; Liu, Choi, and Cahill, 2014; Ong *et al.*, 2018; Brown *et al.*, 2019; Sood *et al.*, 2019; Suryavanshi *et al.*, 2019), the thermal bridge method (Pettes *et al.*, 2011; Wang, Guo *et al.*, 2016; Aiyiti *et al.*, 2018; Aiyiti, Bai *et al.*, 2018), and the resistive thermometer method (Yasaei *et al.*, 2017).

Taube *et al.* (2015) and Zhang *et al.* (2015) measured the ITC of the $\text{MoS}_2/\text{SiO}_2$ interface and found that the ITC is of the order of $0.1 - 2 \text{ MW m}^{-2} \text{ K}^{-1}$. However, this result is 1 order of magnitude lower than other measurements (Neumann *et al.*, 2019; Suryavanshi *et al.*, 2019), probably due to a poor contact condition or a non-negligible contribution of thermal resistance from the substrate. The accepted value of $\text{MoS}_2/\text{SiO}_2$ is tens of $\text{MW m}^{-2} \text{ K}^{-1}$ (Sahoo *et al.*, 2013; Yan *et al.*, 2014; Yalon *et al.*, 2017a, 2017b; Yasaei *et al.*, 2017;

Guo, Yang *et al.*, 2019; Sood *et al.*, 2019). MoS₂ and MoSe₂ act as thermal impeding layers and can lower the ITC of the Al/SiO₂ and Ti/SiO₂ interfaces by nearly 75% due to a weak van der Waals interaction (Brown *et al.*, 2019). However, the ITC of 2D materials can be greatly enhanced via static pressure (Hsieh *et al.*, 2011), electrostatic force (Koh *et al.*, 2016), chemical functionalization (Hopkins *et al.*, 2012; Foley *et al.*, 2015; Han *et al.*, 2016; Zhang *et al.*, 2017; Zhang, Yan *et al.*, 2020), dynamics screening of the substrate (Ong *et al.*, 2013), a rotational mismatch between layers (Estrada *et al.*, 2019; Kim *et al.*, 2021; Ren *et al.*, 2021), etc.

Brown *et al.* (2019) demonstrated a high ITC across the Ti/MoSe₂/SiO₂ interface compared to the Al/MoSe₂/SiO₂ interface, highlighting the importance of using a metal for heat dissipation in devices with 2D materials. Schmidt *et al.* (2010) studied the metal-graphite interface, including Al, Au, Cr, Ti, and Al/Ti, and found that the measured ITC falls in the range of 30 – 100 MW m⁻² K⁻¹, with the highest value observed for the Ti/graphite interface. Although the DMM model fails to explain the experimental data, the work of Schmidt *et al.* (2010) also emphasized the importance of the choice of metal in determining the ITC of the metal-graphite interface.

Chen *et al.* (2009) measured the ITC between the SiO₂ and graphene sheets. They found values between 83 and 180 MW m⁻² K⁻¹ at room temperature and no clear dependence on the number of layers. On the other hand, Koh *et al.* (2010) and Yang, Ziade *et al.* (2014) found that the ITC of the graphene/SiO₂ interface is approximately 20 – 25 MW m⁻² K⁻¹, which is much lower than Ti/SiO₂ and the result observed by Chen *et al.* (2009). Koh *et al.* (2010) and Yang, Ziade *et al.* (2014) argued that contaminations or voids capped inside the interface is responsible for the low ITC and the thickness dependence (Fig. 21). Indeed, Li *et al.* (2017) found that the ITC of the *h*-BN/SiO₂ interface is approximately 62 MW m⁻² K⁻¹ for the monolayer *h*-BN/SiO₂ interface and decreases to 30 MW m⁻² K⁻¹ for 12.8-nm-thick *h*-BN in metal/*h*-BN/SiO₂ interfaces (Fig. 21). When the evidence from AFM is assembled, the results suggest that the voids and gaps between the substrate

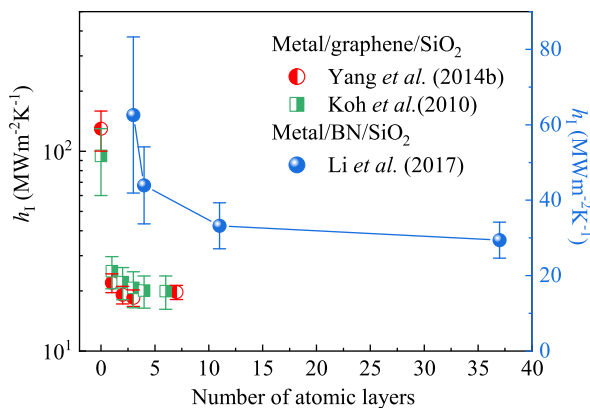


FIG. 21. Thickness-dependent ITC in metal/2D materials/SiO₂ interfaces. Data are adapted from Li *et al.* (2017). From Koh *et al.*, 2010, and Yang, Ziade *et al.*, 2014.

and thick *h*-BN flakes limit the interfacial thermal conduction and are responsible for a decreased ITC with *h*-BN thickness.

3. Interfaces with nanoscale contact

The contact area between nanostructure and substrate or between two nanostructures, such as the contact between two carbon nanotubes, is typically of the order of nm². In this circumstance, the ITR should depend on the area and the geometry of contact; for more details from a theoretical point of view, please see Sec. III.A.1.

The ITR between carbon nanotubes and various substrates, such as Cu, sapphire, and Si/SiO₂, has been studied (Maune, Chiu, and Bockrath, 2006; Son *et al.*, 2008; Gao, Qu, and Yao, 2011; Marconnet, Panzer, and Goodson, 2013). Ju, Hung, and Usui (2006) measured the ITR between a metal and a dielectric at nanoscale. The ITR between two carbon nanotubes was measured by Yang *et al.* (2010, 2014) and modeled by Zhong and Lukes (2006). More detailed discussions can be found in a review by Marconnet, Panzer, and Goodson (2013).

From an experimental point of view, the thermal bridge method provides unique advantages in measuring heat transfer through nanoscale point contact (Yang *et al.*, 2010, 2014; Xiong *et al.*, 2019; Wang, Liang *et al.*, 2020; Zhao, Fitzgerald *et al.*, 2020) that cannot be captured by other methods [Figs. 20(c) and 22(a)].

Yang *et al.* (2014) measured heat transfer through nanoscale contacts between individual multiwalled carbon nanotubes (MWCNTs) [Fig. 20(c)] and found that normalized contact thermal conductance per unit area, which can be regarded as ITC, increases linearly with the tube diameter [Fig. 22(b)], a completely unexpected trend. The AMM and the DMM failed to capture the experimental data, since the two models suggest that the ITC is dominated by the characteristic of the materials contacting each other and the morphology of the interface, rather than the size of the contact area. Yang *et al.* (2014) argued that this unexpected diameter effect is related to the large intrinsic phonon MFP in the *c* axis of the MWCNT, which is similar to that in graphite (Sadeghi, Jo, and Shi, 2013; Chen, Walther, and Koumoutsakos, 2014, 2015; 2016; Wei, Yang *et al.*, 2014; Fu *et al.*, 2020).

Zhao, Fitzgerald *et al.* (2020) measured the ITC between two Ag nanowires and found that its value is approximately 12.1 GW m⁻² K⁻¹, which falls in the range of 4 – 14 GW m⁻² K⁻¹ for the metal-metal interfaces (Gundrum, Cahill, and Averback, 2005; Wilson and Cahill, 2012). The results of Zhao, Fitzgerald *et al.* (2020) showed that the calculated Lorenz number is larger than the Sommerfeld value, which is in sharp contrast to that in the interface between two metallic films (Wilson and Cahill, 2012).

Heat carriers in amorphous materials can be classified into three types of vibration: progagons, diffusons, and locons. How these heat carriers interact with phonons at the interface between amorphous and crystalline materials is still under debate due to the lack of sufficient experimental data. The electron-beam self-heating method (Wang *et al.*, 2011) provides an opportunity to measure the amorphous-crystal interface in a 1D heterostructure. Zhao, Liu *et al.* (2020) performed an experiment on the amorphous-crystal interface in silicon nanowire [Fig. 20(d)] and found that the ITC is approximately

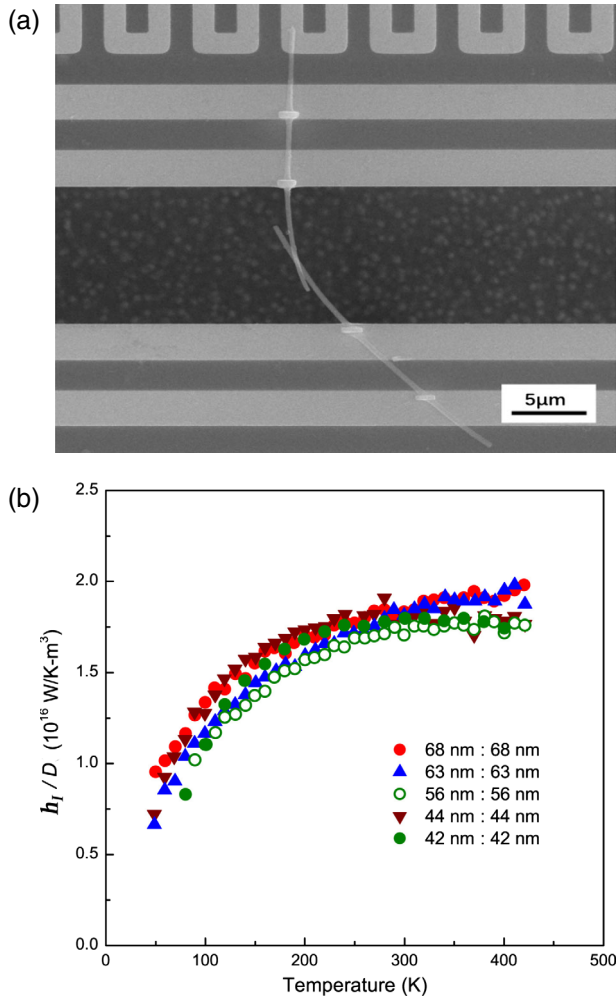


FIG. 22. (a) Nanoscale contact between two nanowires in a thermal bridge measurement. From Wang, Liang *et al.*, 2020. (b) Diameter-dependent normalized contact thermal conductance per unit area between MWCNTs. The labels denote the diameters of the two segments forming a crossed contact. From Yang *et al.*, 2014.

$130 \text{ MW m}^{-2} \text{ K}^{-1}$, which is significantly smaller than that in the amorphous-crystal interface with a macroscopic contact area.

Liu *et al.* (2014) reported the electron-beam self-heating method to profile the thermal resistance along a nanowire with a spatial resolution better than 20 nm [Fig. 11(c)]. The ITC of the Si/NiSi₂ interface embedded in Si/NiSi₂ heterostructured nanowires [Fig. 20(d)] was measured at approximately $500 \text{ MW m}^{-2} \text{ K}^{-1}$ (Fig. 23), which is larger than the value calculated using the DMM ($\sim 325 \text{ MW m}^{-2} \text{ K}^{-1}$). This discrepancy is probably due to the bulk phonon DOS used in the DMM calculation rather than the DOS of a nanowire, or due to the so-called phonon bridging effect induced by a diffusive interface. Liu *et al.* (2014) argued that the few-nanometer buffer layer, supported by TEM data, with disorders and dislocations at the interface serving as an insertion layer bridging the DOS between Si and NiSi₂, and thus enhancing the phonon transmission, which is similar to that in the metal-dielectric interface discussed in Sec. III.A.4.

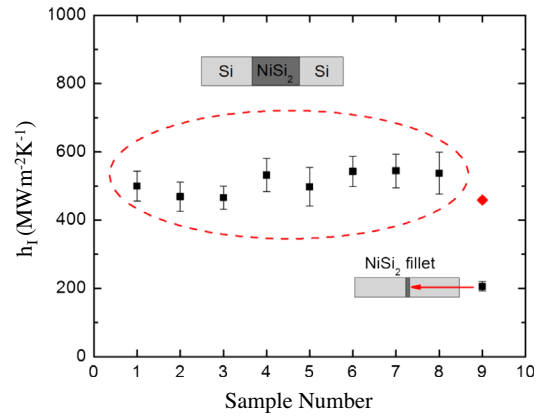


FIG. 23. ITC of the Si/NiSi₂ interfaces in a 1D heterostructure. From Liu *et al.*, 2014.

IV. SOLID-LIQUID INTERFACES

Thermal transport across the solid-liquid interface has been studied intensively since the discovery of ITR, which is also called Kapitza resistance (Kapitza, 1941). There are two main research branches in this field. Low-temperature physicists are interested in solid-helium interfaces at cryogenic temperatures. We use Kapitza resistance in this section for convenience. At high temperatures, thermal engineering scientists prefer to use the terminology of heat transfer coefficient rather than the ITC due to the strong influence of convection. In Sec. IV.B, we focus on the conduction and ignore the convection.

A. Solid-helium interface at cryogenic temperatures

The object of study in low-temperature physics is usually the solid-liquid helium interface. There are two stable isotopes of helium: ⁴He and ³He. The Kapitza resistance of the solid-liquid ⁴He interface, the solid-liquid ³He interface, and the solid/⁴He-³He mixture interface are reviewed in this section. Progress made regarding Kapitza resistance was comprehensively reviewed by Pollack (1969), Harrison (1979), Nakayama (1989), and Swartz and Pohl (1989).

1. Solid-liquid ⁴He interface

The Kapitza resistance between solid and superfluid ⁴He (helium II) was discovered by Kapitza (1941). After that, the steady-state method, the second-sound transmission measurements (Osborne, 1951), and the heat pulse technique (Marx and Eisenmenger, 1982; Bron, 1985) were widely used to measure the Kapitza resistance. The measured Kapitza resistance was found to decrease with increasing temperature approximately as T^{-3} below 0.1 K. This can be explained by phonon transport across the interface according to the AMM (Khalatnikov, 1952) in Eq. (12) and according to the DMM (Swartz and Pohl, 1989) in Eq. (14).

The calculated Kapitza resistance from both the AMM and the DMM usually deviates from the experimental data above 0.1 K due mainly to several mechanisms: (1) the formation of a boundary layer at the interface due to the van der Waals interaction between helium and the solid (Challis, Dransfeld,

and Wilks, 1961), (2) phonon attenuation due to the phonon scattering near the interface (Haug and Weiss, 1972; Perterson and Anderson, 1972, 1973), (3) surface imperfection and phonon scattering at the interface (Lapin, 1969; Sheard and Toombs, 1972a, 1972b; Weber *et al.*, 1978; Wyatt and Page, 1978), and (4) electron-phonon coupling (Little, 1959; Johnson and Little, 1963; Wagner, Kollarits, and Yaqub, 1974). These mechanisms were systematically discussed by Swartz and Pohl (1989). In the following we discuss some selected topics and recent progress.

The measured pressure dependence of the Kapitza resistance was weak, which implies the existence of a boundary layer (Challis, Dransfeld, and Wilks, 1961; Kwang, 1962; Ramiere, Amrit, and Volz, 2012). The acoustic impedance may not be essential, due to the existence of this layer when $T > 0.5$ K. The boundary layer was found to greatly enhance the phonon transmission and reduce the Kapitza resistance (Challis, Dransfeld, and Wilks, 1961).

The phonon modes on the surfaces of solids differ from the bulk phonons (Ezawa, 1971) both on a free solid surface and along a solid-helium interface. In contrast to conventional bulk phonons, which have three acoustic branches, there are five different acoustic branches including the Rayleigh modes along an interface. All these modes can contribute to the Kapitza resistance (Nakayama, 1977, 1985a, 1985b, 1986, 1989) when the tunneling of helium atoms close to the interface is coupled to these modes.

The influence of surface imperfection, including the surface roughness, oxidation, adsorbate, and contamination, is crucial to Kapitza resistance. To obtain intrinsic Kapitza resistance for an ideal interface, the sample surface must be well treated to reduce surface roughness and to remove the oxide layer and impurities (Weber *et al.*, 1978). In the presence of surface imperfection, a multiple phonon process beyond the single phonon process should be considered. Both elastic and inelastic scatterings of phonons near the interface provide additional channels for heat transfer that are not included in either the AMM or the DMM (Weber *et al.*, 1978; Wyatt and Page, 1978; Shiren, 1981; Koblinger *et al.*, 1983; Adamenko and Nemchenko, 2013). Figure 24 shows the temperature-dependent Kapitza resistance of Si/⁴He measured by Johnson and Little (1963) and Amrit (2010). The measured values differ substantially from each other due to different surface treatments (Olson and Pohl, 1994; Amrit and François, 2002). Adamenko and Fuks (1971) theoretically pointed out that the effect of surface roughness should be characterized by the ratio between the characteristic surface roughness dimension and the phonon wavelength, which is noted as σ_{SR} . They further predicted that phonons trapped by roughness introduce a new mechanism of energy transfer across the interface when the roughness height follows a Gaussian distribution and $\sigma_{SR} \approx 0.3$. This prediction was experimentally verified by Amrit (2016) and Ramiere, Volz, and Amrit (2016) through precise control of the nanoscale surface roughness.

The role of conduction electrons was discussed in Sec. II.C. Electron-phonon coupling was suggested to contribute to Kapitza resistance by Khalatnikov (1952) and Little (1959). Wagner, Kollarits, and Yaqub (1974) and Wagner and Yaqub (1975) found a strong magnetic field dependence of Kapitza resistance at the gallium/⁴He interface, and this field

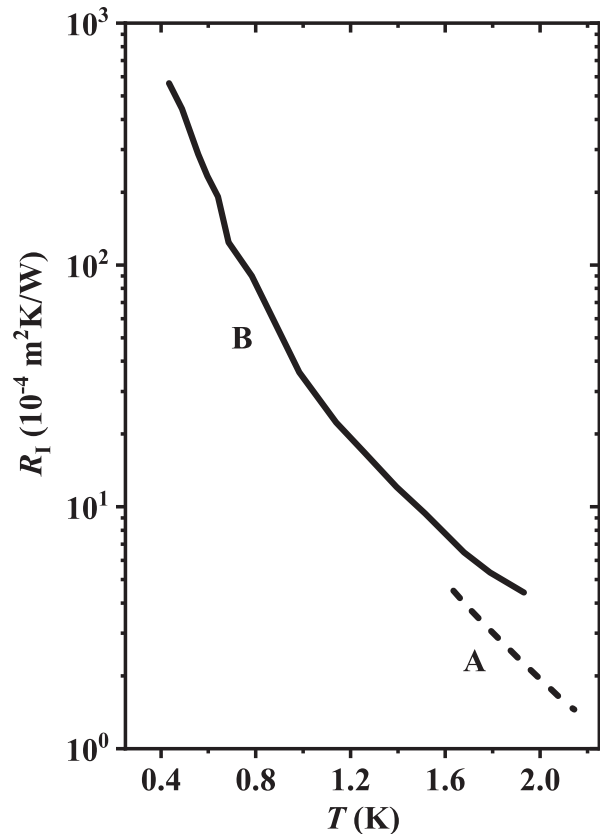


FIG. 24. Kapitza resistance of the Si/⁴He interface as a function of temperature at saturated vapor pressure. The experimental data are from Johnson and Little (1963) (dashed line A) and Amrit (2010) (solid line B).

dependence varied with the magnetic field orientation. The results showed convincing evidence that electrons contribute to ITC across metal–liquid helium interfaces.

Most of the literature focuses on the Kapitza resistance of the solid-bulk helium interface. When the thickness of the helium thin film is only a few atomic layers, some studies found that the Kapitza resistance was significantly enhanced (Mester *et al.*, 1992; Wyatt, 1992; Eggenkamp *et al.*, 1993). However, this effect was not found in other experiments (van Beelen, van der Laar, and van der Hoek, 1994; van der Hoek and van Beelen, 2001).

In addition to the contribution from phonons and electrons, the transmission and reflection of rotons across the solid-superfluid helium interface was also studied by Adamenko, Nemchenko, and Tanatarov (2008). Its contribution to the ITC was found to be as important as that of phonons when $T > 1$ K.

2. Solid-liquid ³He interface

The Kapitza resistance of the solid-liquid ³He interface could be significantly different from that of the solid-liquid ⁴He interface because ⁴He is a boson and ³He is a fermion (Nakayama, 1989). Liquid ³He is a normal liquid above 0.1 K, and the AMM can consequently be applied to the solid-liquid ³He interface. It is interesting that liquid ³He behaves like a Fermi liquid when the temperature is below 0.1 K and

becomes a superfluid when the temperature is below 3 mK. As a result, the thermal transport mechanisms could differ significantly at different temperatures. The Landau-Fermi liquid theory was employed to calculate the Kapitza resistance (Bekarevich and Khalatnikov, 1961; Gavoret, 1965; Toombs, Sheard, and Rice, 1980) when both zero-sound and single-quasiparticle excitations were included. The experimentally measured Kapitza resistance between a metal and liquid ^3He can still be explained by the AMM when $T > 30$ mK and can deviate considerably from the T^{-3} dependence when $T < 30$ mK (Andres and Sprenger, 1975; Harrison and McColl, 1977; Nishiguchi and Nakayama, 1983; Stecher *et al.*, 1990). This is attributed to the low-energy vibrational modes of solids. Nishiguchi and Nakayama (1982) considered the surface vibration of a spherical particle as a periodic perturbation to the surrounding liquid ^3He . The energy is transferred from solid particles to liquid via the excitations of ^3He . The detailed geometric structure of solids was found to be important (Nakayama, 1989). Moreover, the interaction between the oxygen impurities near the interface and ^3He nuclear spins provides an additional magnetic coupling channel that is parallel to the phonon channel (Hu *et al.*, 1996). The overall Kapitza resistance including the magnetic channel shows T^{-1} dependence when $T < 15$ mK, T^{-2} dependence when $15 \text{ mK} < T < 26$ mK, and T^{-3} dependence when $T > 26$ mK (Stecher *et al.*, 1990). The magnetic field dependence of the Kapitza resistance showed a minimum at a field strength of about 2.5 mT (Osheroff and Richardson, 1985; Hu *et al.*, 1996).

A large value of the Kapitza resistance leads to an extremely slow heat exchange rate in the millikelvin regime. Therefore, it is necessary to introduce an enlarged contact area between the solid and liquid helium using sintered metallic powder in the cooling apparatus (Wheatley, Rapp, and Johnson, 1971; Frossati *et al.*, 1977). The efficiency of the dilution refrigerator, which is currently the mainstream equipment in low-temperature physics and quantum computation, is restricted by the overall thermal resistance of the sintered silver powder heat exchanger. Both the enhancement of the specific surface area of the sintered powder and the reduction of Kapitza resistance between the metal and liquid ^3He are key problems in the design of such a heat exchanger.

3. Solid-liquid ^3He - ^4He mixture interface

The Kapitza resistance in the metal- ^3He - ^4He mixture interface is also important to the design of the dilution refrigerator (Frossati, 1978; Osheroff and Corruccini, 1981). When $T < 0.86$ K, the ^3He - ^4He mixture separates into two phases: the concentrated phase with rich ^3He and the dilute phase with rich ^4He . The dilute phase mixture is a unique Fermi liquid with tunable density and Fermi temperature. Dingus, Zhong, and Meyer (1985) found that the Kapitza resistance across a copper-dilute ^3He - ^4He mixture was sensitive to the molar concentration of ^3He interface. A larger concentration of ^3He , which results in a higher Fermi temperature of ^3He , leads to a smaller Kapitza resistance (Nakayama, 1989). As in the pure ^3He case, the sintered silver powder was also used to enlarge the specific surface area of

the heat exchanger in the dilution refrigerator (Cousins *et al.*, 1994). The measured Kapitza resistance of the sintered silver powder and the diluted ^3He - ^4He mixture at millikelvin temperatures is proportional to T^{-2} . This is due to the contribution from the magnetic coupling between the dissolved ^3He atoms in superfluid ^4He and the sinter (Nakayama, 1988).

4. Critical phenomenon

The Kapitza resistance near the superfluid transition temperature (T_λ) is anomalous. Critical behavior has been found when helium is in the superfluid phase (Duncan, Ahlers, and Steinberg, 1987; Frank *et al.*, 1988; Kuehn *et al.*, 2002) and the normal phase (Lipa and Li, 2007). The overall Kapitza resistance should consist of two parts, $R_I = R_I^0 + R_I^s$, where R_I^0 is the noncritical background and R_I^s is the critical part. R_I^s is negligible when T is far away from T_λ . When T is close to T_λ , R_I^s is found to be nonlinear and to be highly dependent on the heat flux J (Duncan, Ahlers, and Steinberg, 1987; Duncan and Ahlers, 1991). In the limit of the zero heat flux ($J \rightarrow 0$), R_I^s can be written as

$$R_I^s \propto \frac{\xi_s}{\kappa_{\text{He}}}, \quad (55)$$

where ξ_s is the characteristic length of the temperature gradient near the interface and κ_{He} is the thermal conductivity of helium. ξ_s is determined by the correlation length ξ_c , which is proportional to $t_r^{-\nu_c}$, with ν_c denoting the critical exponent. $t_r = 1 - T/T_\lambda$ and $t_r = T/T_\lambda - 1$ are the reduced temperatures for $T < T_\lambda$ and $T > T_\lambda$, respectively. From the two-fluid hydrodynamics calculations that consider both a superfluid and a normal fluid, Duncan, Ahlers, and Steinberg (1987) found that $\xi_s \sim t_r^{(1-3\nu_c)/2}$ and $\nu_c = 0.672$. Frank *et al.* (1988) provided another relation $\xi_s \sim t_r^{-\nu_c}$ based on a renormalization-group and a hydrodynamic approach (Dohm, 1985; Tam and Ahlers, 1986). A detailed renormalization-group calculation was carried out by Frank and Dohm (1989). A form similar to Eq. (55) was obtained by Grabinski and Liu (1989) using the hydrodynamic theory developed by Ginzburg and Sobyanin (1976). Olafsen and Behringer (1995) used ac rather than dc heat flux to measure the Kapitza resistance. The peak value of R_I also exhibited critical behavior as $t_r^{-0.137}$. Critical behavior of ITR has also been found in a solid- ^3He - ^4He mixture interface (Dingus, Zhong, and Meyer, 1986a, 1986b).

B. Solid-classical liquid interface at noncryogenic temperature

Understanding of thermal transport across the solid-liquid interface at noncryogenic temperatures is vital for various processes that rely on the thermal coupling between a solid and a liquid ranging from heat pipe engineering (Faghri, 2012), biological self-assembly (Kane, Deschatelets, and Whitesides, 2003), and the evaporative cooling of electronics (Lu *et al.*, 2019) to the lubrication control of liquid film in the heat-assisted magnetic recording technology (Dahl and Bogoy, 2013). Therefore, tremendous effort has been devoted to identifying the key factors that govern the interfacial heat transport across the solid-liquid interface and the associated

physical mechanisms. The ITC of the solid-liquid interface has been studied by experiments and MD simulations and is found to be tunable via the pressure effect (Pham, Barisik, and Kim, 2013; Han, Merabia, and Müller-Plathe, 2017b), surface roughness and patterning (Wang and Koblinski, 2011; Huang *et al.*, 2012; Issa and Mohamad, 2012; Zhang, Chen, and Peterson, 2014), and bonding strength and chemical functionalization (Ge, Cahill, and Braun, 2006; Shenogina *et al.*, 2009; Harikrishna, Ducker, and Huxtable, 2013; Giri and Hopkins, 2014; Giri, Braun, and Hopkins, 2016; Säskilähti *et al.*, 2016; Huang *et al.*, 2018).

1. Interfacial bonding strength

The heat transfer of vibrational energy across the solid-liquid interface is poorly understood compared to that across the solid-solid interface, partly due to the difficulties and challenges in experiments. In this regard, MD simulations have been extensively used to explore various parameter effects. For instance, Barrat and Chiaruttini (2003) used both NEMD and EMD simulations to compute the Kapitza resistance for a solid-liquid interface modeled using the LJ potential. They found that both NEMD and EMD simulations revealed that the Kapitza resistance decreases monotonically when the interfacial interaction strength between solid and liquid atoms increases from the nonwetting case to the wetting case. Based on the LJ model for the solid-liquid interface, Xue *et al.* (2003) further discovered two distinct regimes of Kapitza resistance R_I via NEMD simulations. Their simulation results revealed that in the case with weak interfacial interaction strength (corresponding to the nonwetting liquid) R_I decays exponentially with the solid-liquid interaction strength ϵ_{sl} as $R_I \propto e^{-\gamma\epsilon_{sl}}$, while a power law dependence $R_I \propto \epsilon_{sl}^{-1}$ is observed in the case with strong interaction strength (corresponding to the wetting liquid), exhibiting distinct scaling laws for R_I in different regimes. The same decreasing trend of R_I with an increase in interaction strength has been reported in studies of various solid-liquid interfaces (Kim, Beskok, and Cagin, 2008; Murad and Puri, 2008).

Moreover, Murad and Puri (2008) studied the temperature dependence of the Kapitza resistance at the Si/water interface using NEMD simulations. A decreasing trend of the Kapitza resistance with an increase in temperature was observed for three kinds of liquid phases: the liquid and vapor coexisting phase, the strictly liquid phase, and the supercritical fluid phase. In addition, Ma *et al.* (2018) found via NEMD simulations that attaching the point charge on a graphene sheet with a certain pattern can substantially reduce the Kapitza resistance in the graphene-water interface, partially due to the enhanced solid-liquid interaction via the Coulomb force. More importantly, their simulation results demonstrated that the formation of ordered water molecules similar to the ice structure in a thin layer close to the interface is another important cause for the substantially reduced Kapitza resistance, thus highlighting the significance of an ordered liquid layer in governing thermal transport across the solid-liquid interface. Furthermore, Peng *et al.* (2022) demonstrated via NEMD simulations that introducing an interfacial superlattice structure can significantly reduce the Kapitza resistance in the graphene-water interface by as much as 40%.

Although the solid-liquid interaction strength leads to a liquid density layering phenomenon at the interface and has a notable impact on R_I , Xue *et al.* (2004) found via a NEMD simulation of a 4-nm-thickness monatomic LJ liquid sandwiched between two solid slabs that thermal conductivity of the entire liquid block remains unchanged for both wetting and nonwetting cases. By dividing the liquid block into multiple layers along the thickness direction and resolving the local heat flux in each layer, Liang and Tsai (2011) later found via NEMD simulations of the Au/Ar interface that the local thermal conductivity of an interfacial liquid layer with a thickness of 1 nm (in which liquid layering takes place with a density deviating notably from the density of bulk liquid) is actually 1.6–2.5 times higher than that of the bulk liquid layer away from the interface. These studies suggest that the solid-liquid interaction strength is an important factor that controls the thermal transport across the solid-liquid interface.

Since liquid properties such as wettability are also determined by the solid-liquid interaction strength, much effort has been targeted toward establishing a general relation between the Kapitza resistance and other characteristic properties. Shenogina *et al.* (2009) studied the Kapitza resistance at a solid-water interface using NEMD simulations. The solid part is modeled by the SAM, in which a wide range of wettability from hydrophobic to hydrophilic can be realized by engineering different neutral head-group chemistry. With a variation of the water contact angle θ , their simulation results shown in Fig. 25(a) revealed that the ITC h_I is related to the contact angle as $h_I \propto 1 + \cos \theta$, which is in good agreement with the experimental data (Ge, Cahill, and Braun, 2006). Since the work of adhesion is also linearly proportional to $1 + \cos \theta$, Shenogina *et al.* (2009) demonstrated that h_I is proportional to the work of adhesion, which is a wetting property of the solid-liquid interface. Moreover, Alexeev *et al.* (2015) studied the relation between the Kapitza resistance and the liquid layering density at the graphene-water interface, as shown in Fig. 25(b). By performing extensive NEMD simulations, they found that R_I is inversely proportional to the normalized water density peak $\rho_r = \rho_{\max}/\rho_b$, where ρ_{\max} is the first density peak of the water in the layering region close to graphene and ρ_b is the bulk water density far from the interface. The local density can be computed numerically by counting the number of water molecules in each local bin. As shown in the inset of Fig. 25(b), the first density peak of the water at the interface can be tuned locally by changing the contact angle at the interface, or tuned globally by applying pressure to the entire water block.

Later Ramos-Alvarado, Kumar, and Peterson (2016) examined the universality of the relation between the ITC and the work of adhesion by calculating h_I for different Si/water interfaces via NEMD simulations. They found different linear dependences between h_I and $1 + \cos \theta$ for Si(100) and Si(111) surfaces. For a similar contact angle, h_I for a graphene-coated surface is notably lower than that for a bare Si surface. These results suggest that the relationship between the ITC and wettability (the contact angle) is not universal. To better relate with the ITC, they further proposed the following quantity, which is known as the density depletion length: $\delta = \int_0^\infty [1 - \rho_s(z)/\rho_s^b - \rho_l(z)/\rho_l^b] dz$, where $\rho_s(z)$ and $\rho_l(z)$

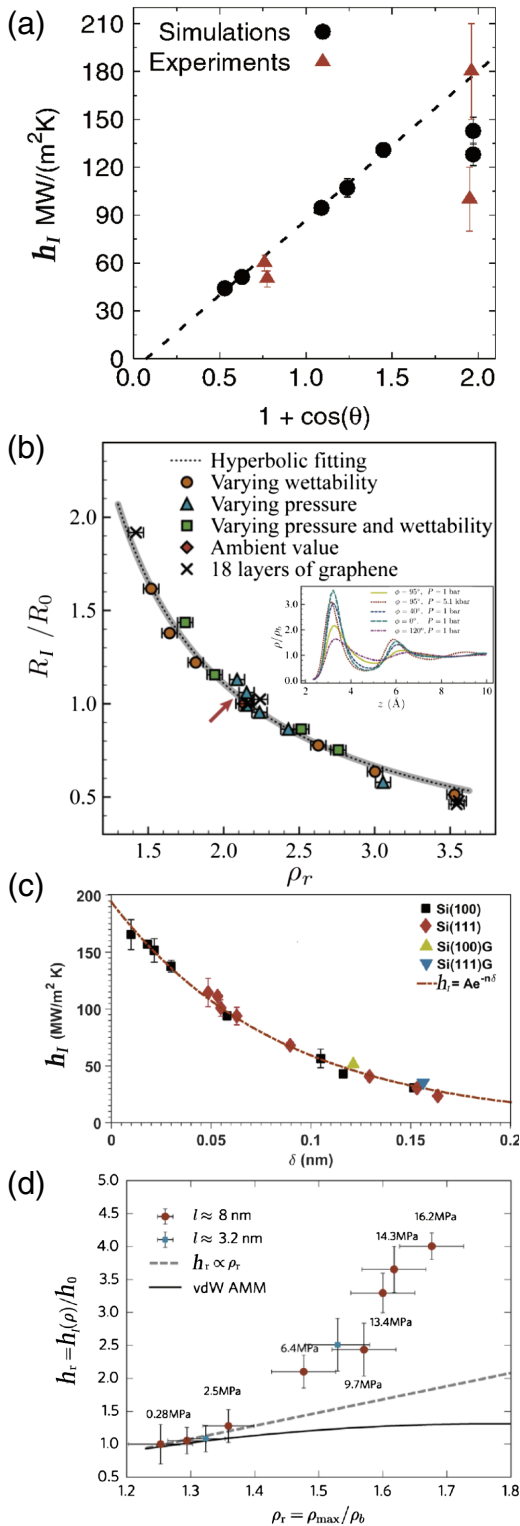


FIG. 25. Relationship between the interfacial thermal transport and characteristic quantities at the solid-liquid interface. (a) ITC of the SAM-water interface as a function of $1 + \cos \theta$. From Shenogina *et al.*, 2009. (b) Normalized ITR of the graphene-water interface vs the reduced water density peak ρ_r . From Alexeev *et al.*, 2015. (c) ITC for various Si/water interfaces vs the density depletion length δ . From Ramos-Alvarado, Kumar, and Peterson, 2016. (d) Normalized ITC of the *n*-perfluorohexane/Au interface G_r vs the reduced water density peak ρ_r at different pressure values. From Han, Merabia, and Müller-Plathe, 2017b.

are, respectively, the density of the solid and liquid along the thickness direction and ρ_s^b and ρ_l^b are the corresponding bulk densities. Based on this quantity, their simulation results for different interfaces, shown in Fig. 25(c), all collapse into a universal relation as $h_I \propto e^{-n\delta}$. Furthermore, Han, Merabia, and Müller-Plathe (2017b) performed NEMD simulations of *n*-perfluorohexane on a Au substrate to study the pressure dependence of h_I . As shown in Fig. 25(d), a linear dependence $h_I \propto \rho_r$ was observed in their study at low pressure, which is consistent with the findings of Alexeev *et al.* (2015) and the AMM for a van der Waals contact (Prasher, 2009). However, a notable deviation from this linear dependence is observed at high pressure due to a non-negligible contribution to the interfacial heat flux from the second density peak in the liquid layering region at high pressure.

2. Surface functionalization

In addition to a variation of the interfacial coupling strength that might not change the interfacial structure, surface functionalization might be the most popular strategy used to enhance the thermal transport across the solid-liquid interface. Shenogin *et al.* (2006) found via EMD simulations that heat transport from the fullerene molecules to the octane liquid involves two processes: the energy flow from high-frequency to low-frequency modes within the solid fullerene, followed by the energy flow from the low-frequency modes in the solid to the liquid. By covalently attaching organic alkane chains to the carbon atoms on the fullerene, they found that the thermal relaxation rate for both processes can be dramatically enhanced, leading to a reduced Kapitza resistance. A similar improvement effect via surface functionalization has also been reported in other kinds of solid-liquid interfaces (Goicochea *et al.*, 2011; Hannah *et al.*, 2015; Wei and Luo, 2019).

Surface functionalization from hydrophobicity to hydrophilicity provides relatively easy access for studying the adhesion effect in the solid-liquid interface. Ge, Cahill, and Braun (2006) found a dramatic change in ITC upon inserting a monolayer SAM molecule into the solid-liquid interface. The measured ITC is $\sim 60 \text{ MW m}^{-2} \text{ K}^{-1}$ on the hydrophobic SAM and $\sim 180 \text{ MW m}^{-2} \text{ K}^{-1}$ on the hydrophilic SAM, managing to tailor the ITC by nearly threefold. Similar results were confirmed by Harikrishna, Ducker, and Huxtable (2013) and Tian, Marconnet, and Chen (2015). The measured ITC is found to increase with either the thermodynamic work of adhesion (Harikrishna, Ducker, and Huxtable, 2013; Giri and Hopkins, 2014) along the solid-liquid interface or the liquid droplet contact angle in air (Shenogina *et al.*, 2009) [Fig. 25 (a)], which can be related to each other. Harikrishna, Ducker, and Huxtable (2013) emphasized that the observed correlation between the work of adhesion and the ITC does not necessarily imply a general mechanism, and further argued that the change in ITC should depend on an overlap of vibrational DOS between the two sides of the interface similar to that observed in solid-solid interfaces; see Sec. III.A.4 for more details. This argument was later confirmed by a MD simulation (Giri and Hopkins, 2014; Sääskilähti *et al.*, 2016) in which a spectral distribution of the heat current across the interface is delivered, thereby providing a detailed picture of the contributions coming from different vibrational modes to

the solid-liquid heat transfer. Sääskilahti *et al.* (2016) suggested that only the out-of-plane vibration contributes to energy transfer when the solid-liquid interaction is weak (i.e., hydrophobicity), while in hydrophilic interfaces with strong coupling the transverse vibrations are involved in the energy transfer. This strong interaction can further extend the high frequencies to the cutoff frequency of the solid, hence enabling faster heat transfer. Furthermore, Huang *et al.* (2018) claimed that the electrostatic interaction between functional groups of SAMs and liquid provides a molecular level energy-transport mechanism for understanding the enhanced ITC produced by stronger interfacial adhesion energy.

More complex surface functionalization was considered by Acharya *et al.* (2012) in NEMD simulations via the introduction of both hydrophobic ($-\text{CF}_3$) and hydrophilic ($-\text{OH}$) headgroups into the SAM/water interface. Their simulation results revealed that h_l increased monotonically with an increasing fraction of hydrophilic headgroups up to 100%, which is as expected since the increasing hydrophilic fraction makes the surface more wet. However, when the fraction of $-\text{OH}$ headgroups is larger than 75%, the corresponding SAM surface is already completely wet ($\cos \theta = 1$), suggesting that wettability or work of adhesion is not a universal parameter that determines the thermal transport across a solid-liquid interface. This conclusion is consistent with the findings of Ramos-Alvarado, Kumar, and Peterson (2016). By analyzing the density distribution, Acharya *et al.* (2012) further found that the overlap of water and SAM density profiles increases with an increasing $-\text{OH}$ headgroup fraction, which causes the hydrogen bonding between the water molecules and the $-\text{OH}$ headgroups and thus results in the intercalated water layer at the interface. A similar enhancement in interfacial heat dissipation due to an intercalated water layer was also found at the cell membrane–water interface (Wang, Qin *et al.*, 2016).

As with the enhanced thermal transport across a solid-solid interface caused by surface roughness discussed in Sec. III.A.5, MD simulations (Shibahara and Takeuchi, 2009; Acharya *et al.*, 2012; Surblys *et al.*, 2019) revealed that the apparent ITC normalized by the regular cross-sectional area at the solid-liquid interface can be enhanced by increasing the nanoscale roughness due to the increased contact area between the solid and liquid. However, when the inherent ITC normalized by the solvent-accessible surface area is considered, only small and subtle variations are observed (Acharya *et al.*, 2012). This is because the introduction of nanoscale roughness can result in an increase of hydrophobicity (Mittal and Hummer, 2010), causing a complex effect of nanoscale roughness on the heat dissipation across the solid-liquid interface, that is sensitive to the details of the roughness (Acharya *et al.*, 2012).

Microscopic mode-level heat transport mechanisms across the solid-liquid interface have been uncovered with MD simulations. Upon analyzing the vibrational DOS in a MD simulation, Caplan, Giri, and Hopkins (2014) discussed the detailed mode coupling mechanisms at a LJ solid-liquid interface under different solid-liquid interaction strength conditions. Compared to the bulk DOS of a solid atom [the shaded region in Fig. 26(a)], the DOS of an interfacial solid atom with a weak interaction strength shifts [black line in Fig. 26(a)] to the lower frequency, and the DOS amplitude for

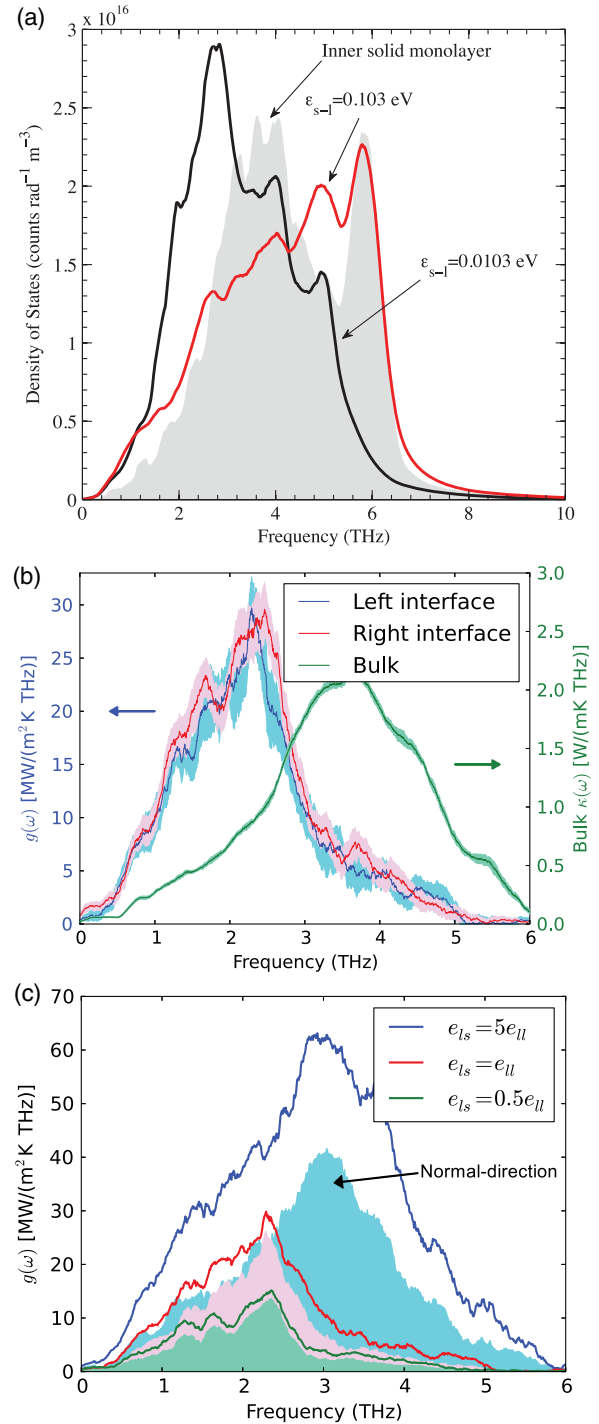


FIG. 26. Spectral analysis for the vibrational modes of a solid-liquid interface. (a) Vibrational DOS of the solid monolayer at a LJ solid-liquid interface with weak (black line, $\epsilon = 0.0103 \text{ eV}$) and strong (red line, $\epsilon = 0.103 \text{ eV}$) solid-liquid interaction strength. The gray shaded region shows the bulk DOS of an inner solid monolayer for comparison. From Caplan, Giri, and Hopkins, 2014. (b) Spectral ITC $g(\omega)$ at a LJ solid-liquid interface (left axis) with the interfacial interaction strength $e_{ls} = e_{ll}$ and the spectral thermal conductivity $\kappa(\omega)$ of the bulk solid (right axis). From Sääskilahti *et al.*, 2016. (c) Spectral ITC $g(\omega)$ at the left solid-liquid interface with various interfacial interaction strengths e_{ls} . The shaded regions denote the contribution to the total $g(\omega)$ in the direction normal to the interface. From Sääskilahti *et al.*, 2016.

the transverse (in-plane) mode (~ 2.8 THz) is not suppressed by the solid-liquid interaction, indicating that transverse modes in a solid are decoupled to the liquid when the interaction strength is weak (the hydrophobic interface). In this case, the DOS of the interfacial solid atom behaves like a free surface, except that the frequencies are redshifted. A redshift of the interfacial DOS spectrum similar to that of the bulk case was also reported in more complex solid-liquid interfaces such as the Si/water interface (Ramos-Alvarado, Kumar, and Peterson, 2016). In contrast, transverse modes of interfacial solid atoms at the hydrophilic interface [i.e., the strong interaction strength denoted by the red line in Fig. 26(a)] are notably suppressed compared to the bulk DOS, suggesting that transverse modes in the solid are strongly coupled to the liquid at the hydrophilic interface.

To understand the transport behavior of an individual mode across the solid-liquid interface, Sääskilähti *et al.* (2016) developed a spectral heat flux method by computing the force-velocity correlation function of interfacial atoms across the solid-liquid interface. As shown in Fig. 26(b), their calculation results for a LJ solid-liquid interface revealed that the spectral ITC $g(\omega)$ defined in Eq. (24) at the solid-liquid interface exhibits a redshift in frequency compared to the spectral thermal conductivity of the bulk solid. This behavior is similar to the frequency shift of the DOS at a free surface compared to the bulk DOS (Caplan, Giri, and Hopkins, 2014). Moreover, high-frequency modes with frequencies higher than 5 THz that contribute to bulk thermal conductivity do not contribute to solid-liquid energy transfer, indicating the decoupling of these high-frequency modes in the solid to the liquid.

By comparing the out-of-plane (normal-direction) component to the total $g(\omega)$, Sääskilähti *et al.* (2016) further studied the role of the in-plane (transverse) mode of solid in solid-liquid heat transport. As shown in Fig. 26(c), for the weak interaction strength ($e_{ls} = 0.5e_{ll}$, nonwetting) case the x component and the total $g(\omega)$ almost overlap with each other, indicating the negligible contribution from the in-plane mode of the solid to interfacial heat transport. In other words, the in-plane modes in the solid are completely decoupled from the liquid in the nonwetting case so that they do not participate in the heat transport across the solid-liquid interface. This picture is consistent with the free-slip boundary condition at a hydrophobic interface (weak interaction strength), which means that liquid atoms can flow freely along the surface, giving rise to a DOS spectrum of interfacial solid atoms similar to the free surface observed by Caplan, Giri, and Hopkins (2014). The situation is significantly different for the strong interaction strength ($e_{ls} = 5e_{ll}$, wetting) case, where the x component is notably lower than the total $g(\omega)$ over the entire frequency range. This difference suggests that the in-plane modes of solids contribute significantly to the interfacial heat transport, which is also consistent with the role of transverse modes at the hydrophilic interface revealed by a DOS analysis (Caplan, Giri, and Hopkins, 2014) and increased contribution of transverse modes with increasing interaction strength (Giri, Braun, and Hopkins, 2016). This is because the strong solid-liquid interaction is essentially equivalent to the no-slip boundary condition, which forces the liquid atoms to follow the motion of the solid atoms and thus enhances the interfacial heat transport. Moreover, the

contribution from high-frequency modes above 5 THz to the ITC is no longer negligible in the strong interaction strength case. An enhanced contribution of high-frequency modes similar to that of the ITC was also reported for the solid-liquid interface between Au and $n\text{-C}_6\text{F}_{14}$ with increasing pressure (Han, Merabia, and Müller-Plathe, 2017b).

With knowledge of the role of transverse modes under different interaction strength conditions and the corresponding previously mentioned boundary condition, Caplan, Giri, and Hopkins (2014) developed an analytical model for the calculation of ITC across the interface between the solid and the classical liquid. Their model is based on the phonon theory of liquid thermodynamics and the DMM and is free of any fitting parameters. The results of ITC for hydrophobic and hydrophilic Al/water and Au/water interfaces predicted by their model agree well with the experimental measurement given by Ge, Cahill, and Braun (2006).

The interface between hard and soft materials is an important kind of solid-liquid interface. Based on MD simulations, Zhang *et al.* (2016) studied the impact of hydrogen bonds on the thermal transport across the hard-soft material interface. In their study, Au is chosen as the hard material, and four types of organic liquids with different polarizations are selected as the soft materials. To form the hydrogen bond with the organic liquids, the Au surface is functionalized with three kinds of self-assembled monolayers. Their simulation results revealed that stronger hydrogen bonds can pull the organic molecules closer to the interface, which shortens the intermolecular distances and thus enhances the intermolecular force across the interface. This stronger interfacial force results in a larger interfacial heat flux, and thus a higher ITC.

3. Nanoparticle-liquid interface

For sufficiently small particles such as nanoparticles, ITC of the interface between a particle and a liquid plays a critical role in the thermal decay of a particle that is heated by a laser pulse (Hartland, 2011). Early experiments by Hu and Hartland (2002, 2003), Mohamed *et al.* (2000), Link *et al.* (2003), and Plech *et al.* (2004) using time-resolved optical pump-probe spectroscopy observed a direct relation between the size of the nanoparticles and the cooling rate. Hu and Hartland (2002, 2003) examined the thermal relaxation of gold nanoparticles with different sizes in water and found that the relaxation time scales as the square of the surface-to-volume ratio. They failed to fit the data using analytical solution to the heat diffusion equation and the discrepancy is a factor of 2. The cooling time constant obtained from the calculations is faster than that obtained from experiments, and they argued that this is due to the non-negligible ITR between the nanoparticle and the liquid, which was later experimentally confirmed by directly measuring the ITC from various groups (Wilson *et al.*, 2002; Huxtable *et al.*, 2003; Wu *et al.*, 2016; Green *et al.*, 2018). The experimental result of Hu and Hartland (2002) suggested an ITC of $\sim 110 \pm 20 \text{ MW m}^{-2} \text{ K}^{-1}$ by fitting the decay time for cooling versus the particle size (Vardeman and Gezelter, 2008), which is consistent with the ITC between the Au nanoparticle and water ($\sim 105 \pm 15 \text{ MW m}^{-2} \text{ K}^{-1}$) measured by Plech *et al.* (2004).

Wilson *et al.* (2002) and Ge, Cahill, and Braun (2004) carried out an experiment on suspensions of 3–10 nm diameter Au, Pt, and AuPd nanoparticles in a liquid and found that, for 5 nm nanoparticles, the ITC for an organic solvent such as toluene is $\sim 50 \text{ MW m}^{-2} \text{ K}^{-1}$. The same particle in water gives $\sim 600 \text{ MW m}^{-2} \text{ K}^{-1}$, which is similar to the reported values in solid-solid interfaces. Ge, Cahill, and Braun (2004) found that the measured ITC in the AuPd/liquid interface changes from ~ 100 to $\sim 300 \text{ MW m}^{-2} \text{ K}^{-1}$, depending on the organic group of the liquid (Park *et al.*, 2012).

Some MD simulations have shown that the ITC of the interface between nanoparticles and the liquid can be modified using various approaches, including the chain length and solvent penetration (Stocker and Gezelter, 2013; Stocker, Neidhart, and Gezelter, 2016; Wu *et al.*, 2016), the density of the polymer coating (Ju, Palpant, and Chalopin, 2017), interface bonding (Merabia, Lombard, and Alkurdi, 2016; Li *et al.*, 2020), etc.

V. SOLID-GAS INTERFACES

The ITR of solid-gas interfaces has not attracted much attention even though it was discovered before the ITR of solid-liquid and solid-solid interfaces.

Based on the theory of Maxwell (1879), Knudsen (1911) introduced a modern term *thermal accommodation coefficient* (or *energy accommodation coefficient*) to characterize the heat exchange and temperature jump at the solid-rarefied gas interface:

$$\varepsilon_{\text{ac}} = \frac{T_f - T_g}{T_s - T_g}, \quad (56)$$

where T_f is the effective temperature of a scattered gas, T_s is the temperature of a solid, and T_g is the temperature of an incident gas. $T_s - T_g = \Delta T$ is the temperature jump. A fraction of gas molecules ε_{ac} is in thermal equilibrium with the solid, while a fraction of gas molecules $1 - \varepsilon_{\text{ac}}$ is assumed to be reflected specularly. Clearly ε_{ac} depends on both T_g and T_s . To simplify the problem, it is convenient to define the equilibrium thermal accommodation coefficient when $T_s \rightarrow T_g$. The heat flux flows across the interface must be the same as the energy loss rate per unit area:

$$\frac{\dot{Q}}{A} = \left(c_{g,v} + \frac{k_B}{2} \right) I_g (T_f - T_g). \quad (57)$$

In Eq. (57) $c_{g,v}$ is the heat capacity of the gas molecule, which is $3k_B/2$ for monatomic gas. An additional $k_B/2$ value comes from the fact that molecules with a larger velocity reach the interface more quickly than molecules with a smaller velocity. $I_g = P/\sqrt{2\pi m_g k_B T_g}$ is the molecular gas intensity where m_g is the mass of molecule and P is the pressure. The ITR can then be obtained as (Goodman, 1974; Quimby and Yen, 1981)

$$R_I = \frac{\sqrt{2\pi m_g k_B T_g}}{\varepsilon_{\text{ac}} (c_{g,v} + k_B/2) P}. \quad (58)$$

Equation (58) shows that the ITR is proportional to the root mean square velocity ($v_{\text{rms}} = \sqrt{3k_B T_g/m_g}$) of the gas molecules and is inversely proportional to the pressure. The only nontrivial physical quantity in Eq. (58) is the thermal accommodation coefficient. Once the thermal accommodation coefficient is known, one can easily calculate the ITR at a given temperature, pressure, and type of gas. Even complete accommodation ($\varepsilon_{\text{ac}} = 1$) would inevitably result in a nonzero ITR. Incomplete accommodation ($0 < \varepsilon_{\text{ac}} < 1$) leads to a larger value of ITR. Therefore, it is impossible to eliminate the temperature jump at the solid-gas interface by thermalizing all of the incident gas molecules.

A. Thermal accommodation coefficient

We point out that the ITR along the solid-rarefied gas interface is mainly determined by the thermal accommodation coefficient. The field of the thermal accommodation coefficient, or the energy accommodation coefficient, is an independent academic discipline that started in the 1870s. It is of great importance to astronautical engineering and thermal engineering. In this section, we give an introduction to the thermal accommodation coefficient. Please see Goodman (1974, 1980) and Goodman and Wachman (1976) for more details.

Baule (1914) gave a simple theory of the thermal accommodation coefficient by considering the surface atoms and gas atoms as hard spheres. The energy transfer due to the collision between a gas atom and a surface atom is calculated. The thermal accommodation coefficient was found to be a monotonic function of mass ratio $\mu_{gs} = m_g/m_s$, where m_s is the mass of the solid atom at the interface. After averaging over the incident angles, one can obtain the Baule formula as

$$\varepsilon_{\text{ac}} = 2 \frac{\mu_{gs}}{(1 + \mu_{gs})^2}. \quad (59)$$

Later Goodman (1967) modified the prefactor of the Baule formula to 2.4 based on more accurate calculations. Along with the hard-sphere model, a comprehensive classical model for the interaction of a gas atom with solid lattice was given by Goodman (1962, 1963). Fan and Manson (2010) used the classical mechanical theory to include both direct-scattering and trapping-desorption processes. Quantum-mechanical methods were developed by considering the interactions between gas molecules and the phonons of solids (Jackson and Mott, 1932; Devonshire, 1937; Goodman and Gillerlain, 1972). In addition, the first-principles method (Pinki and Sundaram, 2020) and the Boltzmann transport equations (Singh *et al.*, 2009) were also used to calculate ε_{ac} .

Figure 27(a) shows the measured thermal accommodation coefficient as a function of temperature for five inert gases on tungsten when the temperature jump at the interface is small. The value of the thermal accommodation coefficient usually varies from 0.01 to 1. Heavier molecules typically possess a larger value of thermal accommodation coefficient, according to Eq. (59). Figure 27(b) shows the calculated ITR from Eq. (58). The values are of the order of 10^{-4} – $10^{-3} \text{ m}^2 \text{ KW}^{-1}$ near room temperature, which is

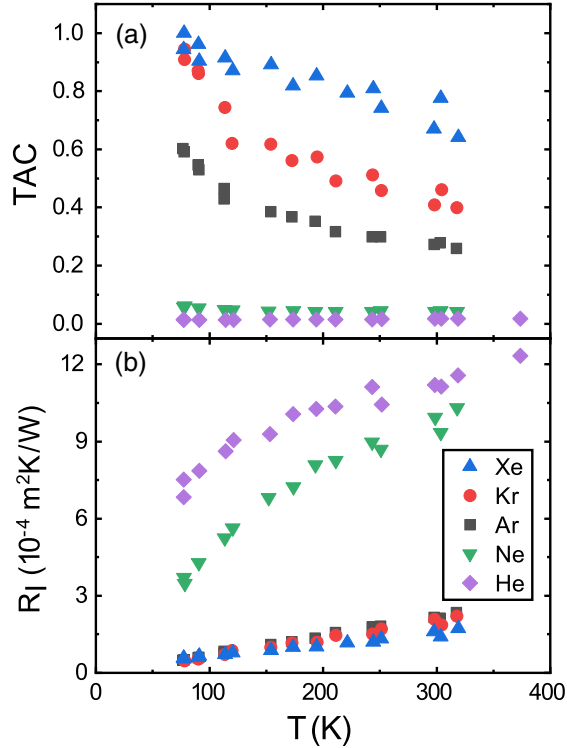


FIG. 27. (a) Measured equilibrium thermal accommodation coefficient (TAC) of the inert gases helium, neon, argon, krypton, and xenon on tungsten. The data are adapted from Thomas (1967) and Kouptsidis and Menzei (1970). (b) ITR of the inert gas-tungsten interface at 1 atm calculated from Eq. (58).

several orders of magnitudes larger than the ITR of the solid-solid and solid-liquid interfaces.

ϵ_{ac} can also be predicted using atomistic simulations such as MD simulations. There are two ways to compute ϵ_{ac} in MD simulations. The direct way is to compute ϵ_{ac} using its definition. In MD simulations, Liang, Evans, and Koblinski (2013) varied the interaction strength between a solid Pr surface and an Ar gas and computed ϵ_{ac} according to Eq. (56) at an imaginary plane 11 Å (the cutoff distance for the solid-gas interaction) away from the solid surface. Their simulation results, which are shown in Fig. 28(a), reveal that with an increase in the solid-gas interaction strength, ϵ_{ac} first increases and then fluctuates around unity in the strong coupling limit. By monitoring the gas atom distribution near the solid surface, they observed in MD simulations limited gas absorption on a solid surface when the interaction strength is weak. When the solid-gas interaction energy is comparable or even higher than the kinetic energy of the gas atoms, the absorption of gas atoms on a solid surface increases exponentially, giving rise to the absorbed gas layer near the solid surface. Multiple absorbed layers can form with a further increase in interaction strength. The formation of the absorbed gas layer on the solid surface facilitates the interfacial heat transfer, as it gives rise to the complete thermalization of a gas atom with a Pr surface at room temperature ($\epsilon_{ac} \rightarrow 1$).

One can also compute ϵ_{ac} indirectly from the ITR based on Eq. (58). The ITR can be obtained using either NEMD simulations with Eq. (2) or EMD simulations with

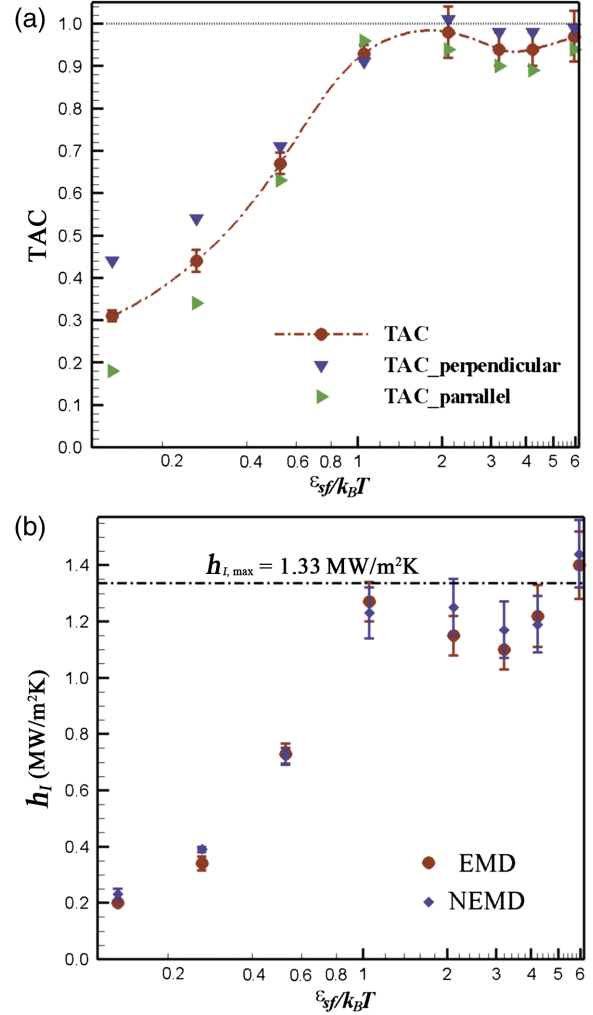


FIG. 28. Numerical calculations of (a) the thermal accommodation coefficient and (b) the ITC of a Pt/Ar interface vs the solid-gas interaction strength ϵ_{sf} from molecular dynamics simulations. From Liang, Evans, and Koblinski, 2013.

Eq. (25). By carefully examining the decay of the interfacial heat flux correlation function, Liang, Evans, and Koblinski (2013) found that when the absorbed gas layer (or multiple layers) is formed, the solid-gas interface in EMD simulations should be defined at a certain distance from the solid surface in order to obtain consistent results between the NEMD and EMD simulations. The separation distance should be larger than the thickness of the outermost absorbed layer. With weak solid-gas interaction strength, the gas absorption on the solid surface is negligible [Fig. 29(a)], so the separation distance can be neglected. With the increase of interaction strength, the separation distance is about 4 Å when one absorbed layer is formed [Fig. 29(b)], and it is about 7 Å when two absorbed layers are formed [Fig. 29(c)]. With such an interface definition, the results of ITC predicted using NEMD and EMD simulations are consistent with each other [Fig. 28(b)], and the indirect prediction of ϵ_{ac} based on Eq. (58) is also consistent with the result directly predicted from Eq. (56). Moreover, the calculated ITC results shown in Fig. 28(b) exhibit a dependence on the solid-gas interaction strength

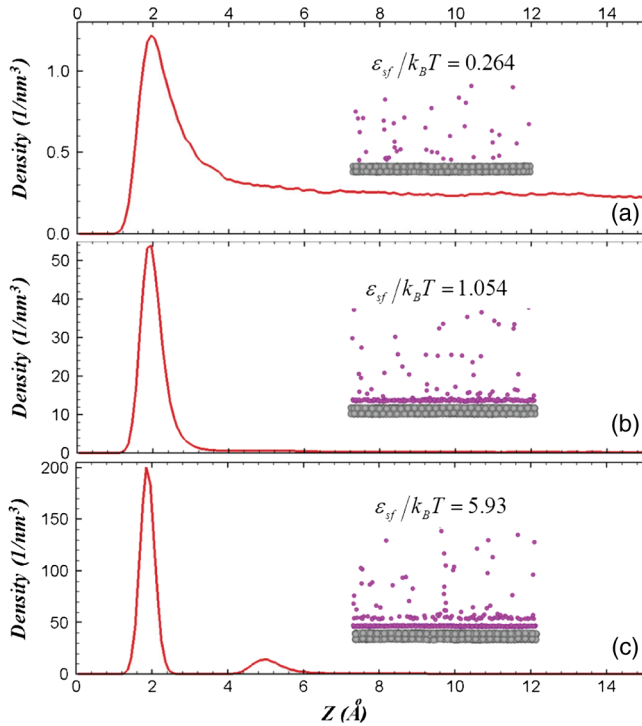


FIG. 29. Density distribution of Ar on Pt surface at 300 K for different solid-gas interaction strength conditions. Insets: corresponding atomic configurations. From Liang, Evans, and Keblinski, 2013.

similar to that of the thermal accommodation coefficient shown in Fig. 28(a).

Using a solid Au slab in contact with Ar or N₂ gas as a model system, Liang and Keblinski (2014b) performed extensive MD simulations to systematically study various parameter effects on ϵ_{ac} , including the solid-gas interaction strength ϵ_{sf} , the gas-solid mass ratio, the temperature, and the solid elasticity. They found that ϵ_{ac} generally increases with an increase in the dimensionless quantity $\epsilon_{sf}/k_B T$, which implies that the interaction strength and T have the opposite effect on ϵ_{ac} when both quantities increase. ϵ_{ac} is found to decrease linearly with the increase of solid elasticity. For a bare solid-gas interface, their simulation results revealed that there is a certain range in which ϵ_{ac} is independent of the gas-solid mass ratio, which differs from Eq. (59). Outside this range, a large mass mismatch between the gas and solid atoms results in a decreased ϵ_{ac} value. Furthermore, when the solid surface is functionalized with the SAM (Liang *et al.*, 2013), their simulation results showed that ϵ_{ac} increases greatly compared to those for a bare surface, which is consistent with the molecular beam experiment (Day and Morris, 2005). For a SAM-functionalized solid surface, there is a maximum ϵ_{ac} when the mass of the monatomic gas has a perfect matching with the mass of the surface atom, while the same phenomenon is absent for the diatomic gas.

Based on the LJ model and the spectral decomposed ITC method (Sääskilähti *et al.*, 2014, 2016), Giri, Braun, and Hopkins (2016) investigated via MD simulations the impact of ϵ_{sf} on the spectral ITC for different polarizations. With the increase of ϵ_{sf} , they found that the number of gas atoms

absorbed on the solid surface increases, and the spectrum of frequencies responsible for the heat flow across the solid-gas interface shifts to a higher frequency. Meanwhile, the relative contribution of the transverse mode to the ITC increases due to the absorbed gas atom on the solid surface, which can effectively couple the transverse mode to the solid. Moreover, the calculated results for the local DOS reveal that the DOS for a solid atom in contact with a gas atom shifts to a lower frequency than the DOS for the bulk solid atom. With weak solid-gas interaction strength, the DOS of the solid atom near the interface mimics that of a free solid surface and remains unchanged with an increase in the solid-gas interaction strength in the absence of gas absorption. With a further increase in the interaction strength, substantial gas absorption on the solid surface takes place, and the DOS of the interfacial solid atom shifts to a higher frequency, caused mainly by a frequency shift of the longitudinal mode.

The thermal accommodation coefficient of the solid-gas interface can also be predicted using theoretical models. Based on the DMM, Giri and Hopkins (2016) developed an analytical model to describe heat transfer across a solid-gas interface. By comparing results from MD simulations, they demonstrated that their analytical model can accurately predict the equilibrium thermal accommodation coefficient of gas atoms on a solid surface at noncryogenic temperatures and with a relatively strong interaction ($\epsilon_{sf} \gtrsim k_B T$). Moreover, Liao *et al.* (2018) constructed a statistical framework of solid-gas collisions by training the Gaussian mixture model with the data obtained from MD simulations. By applying it to the gold-argon and gold-helium interfaces, their trained Gaussian mixture model can predict a thermal accommodation coefficient that is in excellent agreement with the predictions from the MD simulations.

To measure the thermal accommodation coefficient or energy accommodation coefficient ϵ_{ac} , Eq. (56) should be modified as

$$\epsilon_{ac} = \frac{\langle E_f - E_g \rangle}{\langle E_s - E_g \rangle}, \quad (60)$$

where $\langle E_f \rangle$ and $\langle E_g \rangle$ are average molecular gas energies of a scattered gas and an incident gas, respectively. $\langle E_s \rangle$ is defined as $\langle E_s \rangle = c_{g,v} T$ when $T = T_s$. Knudsen designed a classic experiment setup incorporating the Knudsen cell (Fig. 30) to obtain reliable data of the thermal accommodation coefficient

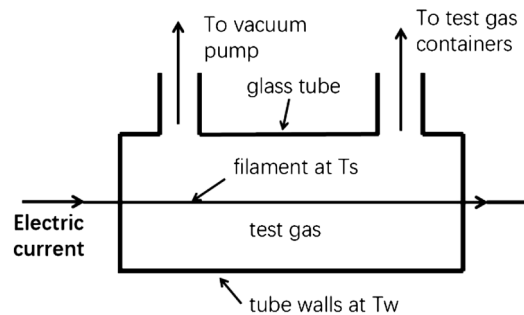


FIG. 30. Schematic of the Knudsen cell. From Goodman, 1980.

(Knudsen, 1911; Goodman, 1980). In the Knudsen cell, the test gas was filled in a cylinder that was equipped with a thin electrically conducting filament whose surface is the test surface. The outer wall of the Knudsen cell was set at temperature T_w . The temperature of filament T_s can be raised above the gas temperature by passing an electric current through the filament. The power loss per unit filament area J is related to the filament current and resistance and can be reliably measured. When the gas pressure P is approximately 0.01–0.1 torr, T_g is equal to T_w , $\langle E_g \rangle = c_{g,v} T_g = c_{g,v} T_w$, and the thermal accommodation coefficient can be obtained.

Other methods for measuring the thermal accommodation coefficient have also been invented and are widely used. The acoustical method presented by Shields and Faughn (1969) was used to infer values of the thermal accommodation coefficient by measuring the speed and absorption of sound in tubes with gas. The experimental data are not good enough as those obtained using the Knudsen cell (Knudsen, 1911), but this method has the advantage of not being restricted to surfaces of the electrically conducting filaments. Lemons and Rosenblatt (1975) used a vibrating-surface method where a solid surface experiences a temperature increase when it vibrates at high frequency in a gas at low pressure. The surface temperature was found to be related to $\varepsilon_{ac}/\varepsilon_{te}$, where ε_{te} is the thermal emissivity of the surface. Compared to the Knudsen cell (Knudsen, 1911), this method has the same advantages and disadvantages as the acoustical method (Shields and Faughn, 1969).

Since the 1990s, studies of thermal transport across a solid-gas interface have been reinvigorated owing to growing interest in technology comprising nanotechnology and lasers. New experimental methods, including the photoacoustical method (Dharmadurai, 1984), the microresonator (Ganta *et al.*, 2011), and MEMS (Grau *et al.*, 2016), were concurrently developed in numerous works. Carbon nanotube aerogels (Schiffres *et al.*, 2012) and parallel plates (Trott *et al.*, 2011) or coaxial cylinders (Yamaguchi *et al.*, 2012) separated by a gas-filled gap were also used as test platforms to measure thermal accommodation coefficient and its pressure dependence.

B. Nanoparticle-gas interface

A recent experiment to measure the chemical composition of gas using the photothermal response of metal nanoparticles in a specific gas was reported (Li, Hong, and Zhang, 2020). The ITR across a nanoparticle-gas interface was considered. The ITR between the nanoparticles and the surrounding gas depends greatly on the diameter of nanoparticles a_{np} . The ratio between the MFP of the gas molecules l_g and a_{np} is the Knudsen number $K_n = l_g/a_{np}$. When $K_n \ll 1$ for a macroscopic interface, the continuum theory is applicable. If the diameter of the nanoparticle is comparable to that of the phonon MFP, the thermal transport of the Knudsen regime ($K_n \sim 1$) should be considered in a different way. Xi *et al.* (2019) found that the ITR between the nanoparticles and the gas can be significantly enhanced when the diameter of the nanoparticles decreases to a few nanometers. The radiation heat transfer must be considered under these circumstances.

VI. SUMMARY AND CHALLENGES

We have reviewed most of the progress achieved in the past 30 years, particularly regarding nanoscale interfaces including two solids, a solid and a liquid, and a solid and a gas. From a theoretical approach, details on the modified acoustic mismatch model, the modified diffuse mismatch model, lattice dynamics, the Green's function, molecular dynamics, etc., have been introduced. From an experimental approach, the pump-probe thermoreflectance technique, the thermal bridge method, the electron-beam self-heating method, etc., have been comprehensively presented. The advantages and bottlenecks of these methods have also been discussed. These methods have been widely used and testified in studying various interfaces and have led to noteworthy achievements. However, the abundant results from experimental measurements and large-scale numerical simulations raised new questions that had not been considered in previous reviews given by Pollack (1969) and Swartz and Pohl (1989).

We have reviewed important factors that can affect the ITR between dissimilar materials. However, such ITR cannot be completely removed, even when two materials are ideally coupled. One strategy to reduce the ITR is to insert between two dissimilar materials an interlayer material that essentially acts as a thermal coupler to bridge the mismatched properties (e.g., the cutoff frequency and acoustic impedance) between dissimilar materials. This concept has attracted significant recent interest in efforts to design an optimized thermal coupler. A homogeneous coupler was first demonstrated to reduce ITR in an abrupt interface for both a 1D atomic chain model (Chen and Zhang, 2015) and a realistic material system (English *et al.*, 2012; Polanco *et al.*, 2017; Ma and Zhang, 2020). Moreover, a design rule for a homogeneous coupler was proposed, and the underlying mechanism for the reduction of ITR was revealed (Chen and Zhang, 2015; Polanco *et al.*, 2017). Later the graded coupler was also demonstrated to more effectively reduce ITR in model systems (Zhou, Zhang, and Hu, 2016; Rastgarkafshgarkolaei *et al.*, 2019; Xiong *et al.*, 2020; Yang *et al.*, 2021). Various types of graded couplers have been proposed, and their efficiencies have been compared (Rastgarkafshgarkolaei *et al.*, 2019; Xiong *et al.*, 2020; Yang *et al.*, 2021). These theoretical studies together with the recent experiments (see Sec. III.A.4) provide valuable insights into the design of a thermal coupler for reducing ITR at realistic interfaces.

Furthermore, we have responded to most questions raised at the beginning of this review including (i) how to define an interface from the ITR point of view; (ii) how to define the temperature near an interface, especially when the interface is in nanoscale; (iii) what the interaction among different heat carriers on the two sides of an interface is; and (iv) what the geometry and size dependence of the ITR is when the area of the interface is in nanoscale. It is not possible to give definitive and final answers to all of these questions. We hope the discussions will attract attention from researchers in different backgrounds. Further study and investigation will advance the research on ITR.

We point out another interesting problem that was not touched on in the main text, since we wrote another specific review about it; see Li *et al.* (2012). Pollack (1969) asked a

question in his review: i.e., whether the ITR is symmetric, namely, whether the heat going from solid to liquid is the same as that going from liquid to solid when the same temperature difference is applied. This question was partially answered in 2004 for a solid-solid interface by Li, Wang, and Casati (2004), who found the thermal rectification phenomenon for two different nonlinear lattices. Later it was found that the rectification was due to asymmetric ITR (Li, Lan, and Wang, 2005). Afterward various proposals for achieving thermal rectification in realistic materials were proposed (Zhang, Hu, and Tang, 2013; Wang *et al.*, 2017; Aiyiti, Zhang *et al.*, 2018; Jiang *et al.*, 2020; Zhang, Ouyang, Chen, and Volz, 2020; Liu, Chen, and Xu, 2021). These findings provide a guide for the realization of phononic thermal control (Li *et al.*, 2012). The discovery of asymmetric ITR in a nonlinear lattice model system has inspired the study of asymmetric acoustic and elastic wave transport; see the recent review on the progress in this field over the past two decades by Nassar *et al.* (2020). Moreover, the phononic thermal rectification has also been extended to asymmetric near field thermal radiation (Li *et al.*, 2021).

Challenges.—Although many achievements have been made in the past 30 years, there are still many challenges and problems. Physicists are always intent on finding a fundamental and general law for the nature phenomena. However, it is difficult to find a universal law for ITR. The reason is that ITR depends sensitively on the details of the interface, such as the exact definition of the interface region, the geometry, physical properties, and even the formation process of an interface. Therefore, it is challenging to formulate a general, let alone a unified, theory to describe the heat transport through an interface.

On the other hand, unlike in the fields of electronics and optics, the available experimental tools for detecting heat flow across the interface are also limited. To explore further details of the underlying physics of thermal transport across the interface, we need to have more advanced techniques to detect temperature, temperature variation, strain, etc. The primary challenge lies in the emergence of nanostructures, which require precise temperature measurement at nanoscale. The pump-probe thermoreflectance technique is successful in measuring the ITR of 2D interfaces but faces severe challenges for the ITR of 1D materials with an interfacial area of approximately tens of square nanometers or even a few square nanometers. The combination of the thermal bridge method and nanoscale thermometry (Kucsko *et al.*, 2013; Idrobo *et al.*, 2018) is probably a solution. A recently developed technique for the direct measurement of local vibrational spectra and phonon dispersion at the interface is capable of detecting detailed information about phonons, and therefore is believed to provide more insight into the ITC (Qi *et al.*, 2021).

The study of interfacial thermal transport provides a theoretical foundation for heat dissipation and the thermal management of modern electronic devices, electronic vehicles, and even future quantum technology, where the preservation of coherence is of the utmost importance.

Our review has provided a comprehensive picture of the fundamental physics of the ITR, but we have not touched upon the applications of ITR, which are key for 5G and 6G electronic devices and electric vehicles, where heat removal

plays a decisive role in making them work properly (Feng *et al.*, 2020; Yue *et al.*, 2021). There are increasing applications of machine learning techniques to the design of thermal interface materials (Ju *et al.*, 2017; Wan *et al.*, 2019; Ouyang *et al.*, 2020, 2021, 2022), but the challenge lies in the shortage of experimental data on the ITR in various materials.

ACKNOWLEDGMENTS

B. L. thanks Dr. Z. X. Cao for the inspiring questions, critical comments, and constructive suggestions. The authors thank J. He, J. Z. Hu, T. Nakayama, Y. L. Ouyang, Q. L. Wang, Q. Xi, and J. X. Zhong for their help. This work was supported partially by the National Natural Science Foundation of China (Grants No. 11890703 and No. 11334007) and the National Key R&D Program of China (Grant No. 2017YFB0406004). J. C. is supported in part by the National Natural Science Foundation of China (Grant No. 12075168) and the Science and Technology Commission of Shanghai Municipality (Grant No. 19ZR1478600). X. X. is supported in part by the National Natural Science Foundation of China (Grant No. 12174286) and the Key-Area Research and Development Program of Guangdong Province (Grant No. 2020B010190004). J. Z. is supported by the Key-Area Research and Development Program of Guangdong Province (Grant No. 2020B0303060001).

REFERENCES

- Acharya, H., N. J. Mozdierz, P. Keblinski, and S. Garde, 2012, *Ind. Eng. Chem. Res.* **51**, 1767.
- Adamenko, I. N., and I. M. Fuks, 1971, *Sov. Phys. JETP* **32**, 1123.
- Adamenko, I. N., and K. E. Nemchenko, 2013, *J. Low Temp. Phys.* **171**, 266.
- Adamenko, I. N., K. E. Nemchenko, and I. V. Tanatarov, 2008, *Phys. Rev. B* **77**, 174510.
- Aiyiti, A., X. Bai, J. Wu, X. F. Xu, and B. Li, 2018, *Sci. Bull.* **63**, 452.
- Aiyiti, A., Z. Zhang, B. Chen, S. Hu, J. Chen, X. Xu, and B. Li, 2018, *Carbon* **140**, 673.
- Aiyiti, A., *et al.*, 2018, *Nanoscale* **10**, 2727.
- Alexeev, D., J. Chen, J. H. Walther, K. P. Giapis, P. Angelikopoulos, and P. Koumoutsakos, 2015, *Nano Lett.* **15**, 5744.
- Alkurdi, A., S. Pailhès, and S. Merabia, 2017, *Appl. Phys. Lett.* **111**, 093101.
- Allen, P. B., 1987, *Phys. Rev. Lett.* **59**, 1460.
- Aller, H. T., X. Yu, A. Wise, R. S. Howell, A. J. Gellman, A. J. H. McGaughey, and J. A. Malen, 2019, *Nano Lett.* **19**, 8533.
- Alvarez, F. X., J. Alvarez-Quintana, D. Jou, and J. R. Viejo, 2010, *J. Appl. Phys.* **107**, 084303.
- Alvarez-Quintana, J., and J. Rodríguez-Viejo, 2008, *J. Appl. Phys.* **104**, 074903.
- Amrit, J., 2010, *Phys. Rev. B* **81**, 054303.
- Amrit, J., 2016, *Low Temp. Phys.* **42**, 617.
- Amrit, J., and M. X. François, 2002, *J. Low Temp. Phys.* **128**, 113.
- Andres, K., and W. O. Sprenger, 1975, in *Proceedings of the 14th International Conference on Low Temperature Physics, Otaniemi, Finland, 1975*, Vol. 1, edited by M. Krusius and M. Vuorio (North-Holland, Amsterdam), p. 123.
- Barragán, L. A., J. I. Artigas, R. Alonso, and F. Villuendas, 2001, *Rev. Sci. Instrum.* **72**, 247.

- Barrat, J.-L., and F. Chiaruttini, 2003, *Mol. Phys.* **101**, 1605.
- Bauer, R., A. Schmid, P. Pavone, and D. Strauch, 1998, *Phys. Rev. B* **57**, 11276.
- Baule, B., 1914, *Ann. Phys. (Berlin)* **349**, 145.
- Beechem, T., J. C. Duda, P. E. Hopkins, and P. M. Norris, 2010, *Appl. Phys. Lett.* **97**, 061907.
- Beechem, T., and P. E. Hopkins, 2009, *J. Appl. Phys.* **106**, 124301.
- Bekarevich, I. L., and I. M. Khalatnikov, 1961, *Sov. Phys. JETP* **12**, 1187.
- Berendsen, H. J. C., J. P. M. Postma, W. F. van Gunsteren, A. DiNola, and J. R. Haak, 1984, *J. Chem. Phys.* **81**, 3684.
- Bezuglyj, A. I., and V. A. Shklovskij, 2016, *Low Temp. Phys.* **42**, 636.
- Braun, J. L., C. M. Rost, M. Lim, A. Giri, D. H. Olson, G. N. Kotsonis, G. Stan, D. W. Brenner, J. P. Maria, and P. E. Hopkins, 2018, *Adv. Mater.* **30**, 1805004.
- Bron, W. E., 1985, *Nonequilibrium Phonon Dynamics* (Plenum Press, New York).
- Brorson, S. D., A. Kazeroonian, J. S. Moodera, D. W. Face, T. K. Cheng, E. P. Ippen, M. S. Dresselhaus, and G. Dresselhaus, 1990, *Phys. Rev. Lett.* **64**, 2172.
- Brown, D. B., W. Shen, X. Li, K. Xiao, D. B. Geohegan, and S. Kumar, 2019, *ACS Appl. Mater. Interfaces* **11**, 14418.
- Budaev, B. V., and D. B. Bogy, 2010a, *J. Phys. A* **43**, 425201.
- Budaev, B. V., and D. B. Bogy, 2010b, *Phys. Lett. A* **374**, 4774.
- Budaev, B. V., and D. B. Bogy, 2010c, *SIAM J. Appl. Math.* **70**, 1691.
- Cahill, D. G., 1990, *Rev. Sci. Instrum.* **61**, 802.
- Cahill, D. G., 2004, *Rev. Sci. Instrum.* **75**, 5119.
- Cahill, D. G., A. Bullen, and S.-M. Lee, 2000, *High Temp. High Press.* **32**, 135.
- Cahill, D. G., W. K. Ford, K. E. Goodson, G. D. Mahan, A. Majumdar, H. J. Maris, R. Merlin, and S. R. Phillpot, 2003, *J. Appl. Phys.* **93**, 793.
- Cahill, D. G., *et al.*, 2014, *Appl. Phys. Rev.* **1**, 011305.
- Cancellieri, C., E. A. Scott, J. Braun, S. W. King, R. Oviedo, C. Jezewski, J. Richards, F. La Mattina, L. P. H. Jeurgens, and P. E. Hopkins, 2020, *J. Appl. Phys.* **128**, 195302.
- Capinski, W. S., and H. J. Maris, 1996, *Rev. Sci. Instrum.* **67**, 2720.
- Capinski, W. S., H. J. Maris, T. Ruf, M. Cardona, K. Ploog, and D. S. Katzer, 1999, *Phys. Rev. B* **59**, 8105.
- Caplan, M. E., A. Giri, and P. E. Hopkins, 2014, *J. Chem. Phys.* **140**, 154701.
- Carlborg, C. F., J. Shiomi, and S. Maruyama, 2008, *Phys. Rev. B* **78**, 205406.
- Casimir, H. B. G., 1938, *Physica (Amsterdam)* **5**, 495.
- Chakraborty, S., C. A. Kleint, A. Heinrich, C. M. Schneider, J. Schumann, M. Falke, and S. Teichert, 2003, *Appl. Phys. Lett.* **83**, 4184.
- Challis, L. J., J. D. N. Cheeke, and L. F. Bates, 1968, *Proc. R. Soc. A* **304**, 479.
- Challis, L. J., K. Dransfeld, and J. Wilks, 1961, *Proc. R. Soc. A* **260**, 31.
- Chang, C. W., A. M. Fennimore, A. Afanasiev, D. Okawa, T. Ikuno, H. Garcia, D. Li, A. Majumdar, and A. Zettl, 2006, *Phys. Rev. Lett.* **97**, 085901.
- Cheaito, R., C. A. Polanco, S. Addamane, J. Zhang, A. W. Ghosh, G. Balakrishnan, and P. E. Hopkins, 2018, *Phys. Rev. B* **97**, 085306.
- Cheaito, R., *et al.*, 2015a, *Phys. Rev. B* **91**, 035432.
- Cheaito, R., *et al.*, 2015b, *Appl. Phys. Lett.* **106**, 093114.
- Chen, B., and L. Zhang, 2015, *J. Phys. Condens. Matter* **27**, 125401.
- Chen, G., 1998, *Phys. Rev. B* **57**, 14958.
- Chen, G., 2021, *Nat. Rev. Phys.* **3**, 555.
- Chen, G., and M. Neagu, 1997, *Appl. Phys. Lett.* **71**, 2761.
- Chen, G., and T. Zeng, 2010, *Microscale Thermophys. Eng.* **5**, 71.
- Chen, J., J. H. Walther, and P. Koumoutsakos, 2014, *Nano Lett.* **14**, 819.
- Chen, J., J. H. Walther, and P. Koumoutsakos, 2015, *Adv. Funct. Mater.* **25**, 7539.
- Chen, J., J. H. Walther, and P. Koumoutsakos, 2016, *Nanotechnology* **27**, 465705.
- Chen, J., G. Zhang, and B. Li, 2010a, *Phys. Lett. A* **374**, 2392.
- Chen, J., G. Zhang, and B. Li, 2010b, *J. Phys. Soc. Jpn.* **79**, 074604.
- Chen, J., G. Zhang, and B. Li, 2010c, *Nano Lett.* **10**, 3978.
- Chen, J., G. Zhang, and B. Li, 2012, *J. Appl. Phys.* **112**, 064319.
- Chen, J. Y., J. Zhu, D. Zhang, D. M. Lattery, M. Li, J. P. Wang, and X. Wang, 2016, *J. Phys. Chem. Lett.* **7**, 2328.
- Chen, L., Z. Huang, and S. Kumar, 2013, *Appl. Phys. Lett.* **103**, 123110.
- Chen, X.-K., M. Pang, T. Chen, D. Du, and K.-Q. Chen, 2020, *ACS Appl. Mater. Interfaces* **12**, 15517.
- Chen, Z., W. Jang, W. Bao, C. N. Lau, and C. Dames, 2009, *Appl. Phys. Lett.* **95**, 161910.
- Cheng, Z., *et al.*, 2020, *Commun. Phys.* **3**, 115.
- Clemens, B. M., G. L. Eesley, and C. A. Paddock, 1988, *Phys. Rev. B* **37**, 1085.
- Collins, K. C., S. Chen, and G. Chen, 2010, *Appl. Phys. Lett.* **97**, 083102.
- Costescu, R. M., M. A. Wall, and D. G. Cahill, 2003, *Phys. Rev. B* **67**, 054302.
- Cousins, D. J., S. N. Fisher, A. M. Guénault, G. R. Pickett, E. N. Smith, and R. P. Turner, 1994, *Phys. Rev. Lett.* **73**, 2583.
- Dahl, J. B., and D. B. Bogy, 2013, *Tribol. Lett.* **52**, 27.
- Dai, J., and Z. Tian, 2020, *Phys. Rev. B* **101**, 041301.
- Daly, B. C., and H. J. Maris, 2002, *Physica (Amsterdam)* **316B–317B**, 247.
- Dames, C., 2013, *Annu. Rev. Heat Transfer* **16**, 7.
- Dames, C., and G. Chen, 2004, *J. Appl. Phys.* **95**, 682.
- Datta, S., 1997, *Electronic Transport in Mesoscopic Systems* (Cambridge University Press, Cambridge, England).
- Day, B. S., and J. R. Morris, 2005, *J. Chem. Phys.* **122**, 234714.
- Dechaumphai, E., D. Lu, J. J. Kan, J. Moon, E. E. Fullerton, Z. Liu, and R. Chen, 2014, *Nano Lett.* **14**, 2448.
- Devonshire, A. F., 1937, *Proc. R. Soc. A* **158**, 269.
- Dhar, A., 2008, *Adv. Phys.* **57**, 457.
- Dharmadurai, G., 1984, *Phys. Status Solidi (a)* **83**, K27.
- Dingus, M., F. Zhong, and H. Meyer, 1985, *Phys. Rev. Lett.* **54**, 2347.
- Dingus, M., F. Zhong, and H. Meyer, 1986a, *J. Low Temp. Phys.* **65**, 213.
- Dingus, M., F. Zhong, and H. Meyer, 1986b, *J. Low Temp. Phys.* **65**, 185.
- Dohm, V., 1985, *Z. Phys. B* **61**, 193.
- Dong, L., Q. Xi, D. Chen, J. Guo, T. Nakayama, Y. Li, Z. Liang, J. Zhou, X. Xu, and B. Li, 2018, *Natl. Sci. Rev.* **5**, 500.
- Dong, L., Q. Xi, J. Zhou, X. Xu, and B. Li, 2020, *Phys. Rev. Applied* **13**, 034019.
- Duda, J. C., T. E. Beechem, J. L. Smoyer, P. M. Norris, and P. E. Hopkins, 2010, *J. Appl. Phys.* **108**, 073515.
- Duda, J. C., and P. E. Hopkins, 2012, *Appl. Phys. Lett.* **100**, 111602.
- Duda, J. C., P. E. Hopkins, T. E. Beechem, J. L. Smoyer, and P. M. Norris, 2010, *Superlattices Microstruct.* **47**, 550.
- Duda, J. C., C. J. Kimmer, W. A. Soffa, X. W. Zhou, R. E. Jones, and P. E. Hopkins, 2012, *J. Appl. Phys.* **112**, 093515.
- Duda, J. C., P. M. Norris, and P. E. Hopkins, 2011, *J. Heat Transfer* **133**, 074501.

- Duda, J. C., C.-Y. P. Yang, B. M. Foley, R. Cheaito, D. L. Medlin, R. E. Jones, and P. E. Hopkins, 2013, *Appl. Phys. Lett.* **102**, 081902.
- Duffy, D. M., and A. M. Rutherford, 2007, *J. Phys. Condens. Matter* **19**, 016207.
- Duncan, R. V., and G. Ahlers, 1991, *Phys. Rev. B* **43**, 7707.
- Duncan, R. V., G. Ahlers, and V. Steinberg, 1987, *Phys. Rev. Lett.* **58**, 377.
- Eesley, G. L., 1983, *Phys. Rev. Lett.* **51**, 2140.
- Eggenkamp, M. E. W., H. Khalil, J. P. Laheurte, J. C. Noiray, and J. P. Romagnan, 1993, *Europhys. Lett.* **21**, 587.
- Elsayed-Ali, H. E., T. B. Norris, M. A. Pessot, and G. A. Mourou, 1987, *Phys. Rev. Lett.* **58**, 1212.
- English, T. S., J. C. Duda, J. L. Smoyer, D. A. Jordan, P. M. Norris, and L. V. Zhigilei, 2012, *Phys. Rev. B* **85**, 035438.
- Esfarjani, K., and H. T. Stokes, 2008, *Phys. Rev. B* **77**, 144112.
- Estrada, D., *et al.*, 2019, *npj 2D Mater. Appl.* **3**, 10.
- Evans, W. J., L. Hu, and P. Koblinski, 2010, *Appl. Phys. Lett.* **96**, 203112.
- Ezawa, H., 1971, *Ann. Phys. (N.Y.)* **67**, 438.
- Fagas, G., A. Kozorezov, C. Lambert, and J. Wigmore, 1999, *Physica (Amsterdam)* **263B–264B**, 739.
- Fagas, G., A. G. Kozorezov, C. J. Lambert, J. K. Wigmore, A. Peacock, A. Poelaert, and R. den Hartog, 1999, *Phys. Rev. B* **60**, 6459.
- Faghri, A., 2012, *J. Heat Transfer* **134**, 123001.
- Fan, G., and J. Manson, 2010, *Chem. Phys.* **370**, 175.
- Feng, T., L. Lindsay, and X. Ruan, 2017, *Phys. Rev. B* **96**, 161201.
- Feng, T., Y. Zhong, J. Shi, and X. Ruan, 2019, *Phys. Rev. B* **99**, 045301.
- Feng, X., D. Ren, X. He, and M. Ouyang, 2020, *Joule* **4**, 743.
- Foley, B. M., S. C. Hernández, J. C. Duda, J. T. Robinson, S. G. Walton, and P. E. Hopkins, 2015, *Nano Lett.* **15**, 4876.
- Fong, S. W., A. Sood, L. Chen, N. Kumari, M. Asheghi, K. E. Goodson, G. A. Gibson, and H.-S. P. Wong, 2016, *J. Appl. Phys.* **120**, 015103.
- Fourier, J. B. J., 1822, *Théorie Analytique de la Chaleur* (Cambridge University Press, Cambridge, England).
- Frank, D., and V. Dohm, 1989, *Phys. Rev. Lett.* **62**, 1864.
- Frank, D., M. Grabinski, V. Dohm, and M. Liu, 1988, *Phys. Rev. Lett.* **60**, 2336.
- Freedman, J. P., X. Yu, R. F. Davis, A. J. Gellman, and J. A. Malen, 2016, *Phys. Rev. B* **93**, 035309.
- Freedy, K. M., A. Giri, B. M. Foley, M. R. Barone, P. E. Hopkins, and S. McDonnell, 2018, *Nanotechnology* **29**, 145201.
- Freedy, K. M., D. H. Olson, P. E. Hopkins, and S. J. McDonnell, 2019, *Phys. Rev. Mater.* **3**, 104001.
- Freedy, K. M., T. Zhu, D. H. Olson, P. M. Litwin, P. E. Hopkins, M. Zebarjadi, and S. J. McDonnell, 2020, *2D Mater.* **7**, 045033.
- Frossati, G., 1978, *J. Phys. (Paris), Colloq.* **39**, C6-1578.
- Frossati, G. H., H. Godfrin, B. Hebral, G. Schumacher, and D. Thoulouze, 1977, in *Proceedings of the International Symposium on Physics at Ultralow Temperatures, Hakone, Japan, 1977*, edited by T. Sugawara and N. G. Shinkōkai (Physical Society of Japan, Tokyo, Japan), p. 205.
- Fu, Y., *et al.*, 2020, *2D Mater.* **7**, 012001.
- Ganta, D., E. B. Dale, J. P. Rezac, and A. T. Rosenberger, 2011, *J. Chem. Phys.* **135**, 084313.
- Gao, F., J. Qu, and M. Yao, 2011, *J. Appl. Phys.* **110**, 124314.
- Garg, J., and G. Chen, 2013, *Phys. Rev. B* **87**, 140302(R).
- Gavoret, V. V., 1965, *Phys. Rev.* **137**, A721.
- Ge, Z., D. G. Cahill, and P. V. Braun, 2004, *J. Phys. Chem. B* **108**, 18870.
- Ge, Z., D. G. Cahill, and P. V. Braun, 2006, *Phys. Rev. Lett.* **96**, 186101.
- Ginzburg, V. L., and A. A. Sobyenin, 1976, *Sov. Phys. Usp.* **19**, 773.
- Giri, A., J. L. Braun, and P. E. Hopkins, 2016, *J. Phys. Chem. C* **120**, 24847.
- Giri, A., R. Cheaito, J. T. Gaskins, T. Mimura, H. J. Brown-Shaklee, D. L. Medlin, J. F. Ihlefeld, and P. E. Hopkins, 2021, *ACS Appl. Mater. Interfaces* **13**, 12541.
- Giri, A., B. M. Foley, and P. E. Hopkins, 2014, *J. Heat Transfer* **136**, 092401.
- Giri, A., J. T. Gaskins, B. F. Donovan, C. Szwejkowski, R. J. Warzoha, M. A. Rodriguez, J. Ihlefeld, and P. E. Hopkins, 2015, *J. Appl. Phys.* **117**, 105105.
- Giri, A., J. T. Gaskins, L. Li, Y.-S. Wang, O. V. Prezhdo, and P. E. Hopkins, 2019, *Phys. Rev. B* **99**, 165139.
- Giri, A., and P. E. Hopkins, 2014, *Appl. Phys. Lett.* **105**, 033106.
- Giri, A., and P. E. Hopkins, 2016, *J. Chem. Phys.* **144**, 084705.
- Giri, A., and P. E. Hopkins, 2017, *Sci. Rep.* **7**, 11011.
- Giri, A., and P. E. Hopkins, 2020, *Adv. Funct. Mater.* **30**, 1903857.
- Giri, A., *et al.*, 2018, *Adv. Mater.* **30**, 1804097.
- Goicochea, J. V., M. Hu, B. Michel, and D. Poulikakos, 2011, *J. Heat Transfer* **133**, 082401.
- Goodman, F. O., 1962, *J. Phys. Chem. Solids* **23**, 1269.
- Goodman, F. O., 1963, *J. Phys. Chem. Solids* **24**, 1451.
- Goodman, F. O., 1967, *Surf. Sci.* **7**, 391.
- Goodman, F. O., 1974, *Prog. Surf. Sci.* **5**, 261.
- Goodman, F. O., 1980, *J. Phys. Chem.* **84**, 1431.
- Goodman, F. O., and J. D. Gillerlain, 1972, *J. Chem. Phys.* **57**, 3645.
- Goodman, F. O., and H. Y. Wachman, 1976, *Dynamics of Gas-Surface Scattering* (Academic Press, New York).
- Gorham, C. S., *et al.*, 2014, *Phys. Rev. B* **90**, 024301.
- Grabinski, M., and M. Liu, 1989, *Phys. Rev. B* **40**, 8720.
- Grau, M., F. Völklein, A. Meier, C. Kunz, J. Heidler, and P. Woias, 2016, *J. Vac. Sci. Technol. A* **34**, 041601.
- Green, B. G., S. M. Budy, S. M. Reed, and M. E. Siemens, 2018, *J. Appl. Phys.* **124**, 144301.
- Groeneveld, R. H., R. Sprik, and A. Lagendijk, 1992, *Phys. Rev. B* **45**, 5079.
- Groeneveld, R. H., R. Sprik, and A. Lagendijk, 1995, *Phys. Rev. B* **51**, 11433.
- Gu, X., X. Li, and R. Yang, 2015, *Phys. Rev. B* **91**, 205313.
- Gundrum, B. C., D. G. Cahill, and R. S. Averback, 2005, *Phys. Rev. B* **72**, 245426.
- Guo, J., Y. Huang, X. Wu, Q. Wang, X. Zhou, X. Xu, and B. Li, 2019, *Phys. Status Solidi RRL* **13**, 1800529.
- Guo, J., F. Yang, M. Xia, X. Xu, and B. Li, 2019, *J. Phys. D* **52**, 385306.
- Guo, L., S. L. Hodson, T. S. Fisher, and X. Xu, 2012, *J. Heat Transfer* **134**, 042402.
- Hahn, K. R., M. Puligheddu, and L. Colombo, 2015, *Phys. Rev. B* **91**, 195313.
- Han, H., S. Merabia, and F. Müller-Plathe, 2017a, *Nanoscale* **9**, 8314.
- Han, H., S. Merabia, and F. Müller-Plathe, 2017b, *J. Phys. Chem. Lett.* **8**, 1946.
- Han, H., *et al.*, 2016, *Nat. Commun.* **7**, 11281.
- Hannah, D. C., J. D. Gezelter, R. D. Schaller, and G. C. Schatz, 2015, *ACS Nano* **9**, 6278.
- Hao, M. L., J. Li, S. Park, S. Moura, and C. Dames, 2018, *Nat. Energy* **3**, 899.

- Harikrishna, H., W. A. Ducker, and S. T. Huxtable, 2013, *Appl. Phys. Lett.* **102**, 251606.
- Harrison, J. P., 1979, *J. Low Temp. Phys.* **37**, 467.
- Harrison, J. P., and D. B. McColl, 1977, *J. Phys. C* **10**, L297.
- Hartland, G. V., 2011, *Chem. Rev.* **111**, 3858.
- Hase, M., K. Ishioka, J. Demsar, K. Ushida, and M. Kitajima, 2005, *Phys. Rev. B* **71**, 184301.
- Haug, H., and K. Weiss, 1972, *Phys. Lett.* **40A**, 19.
- Hochbaum, A. I., R. Chen, R. D. Delgado, W. Liang, E. C. Garnett, M. Najarian, A. Majumdar, and P. Yang, 2008, *Nature (London)* **451**, 163.
- Hohensee, G. T., R. B. Wilson, and D. G. Cahill, 2015, *Nat. Commun.* **6**, 6578.
- Hoover, W. G., 1985, *Phys. Rev. A* **31**, 1695.
- Hopkins, P. E., 2009, *J. Appl. Phys.* **106**, 013528.
- Hopkins, P. E., 2013, *ISRN Mech. Eng.* **2013**, 682586.
- Hopkins, P. E., M. Baraket, E. V. Barnat, T. E. Beechem, S. P. Kearney, J. C. Duda, J. T. Robinson, and S. G. Walton, 2012, *Nano Lett.* **12**, 590.
- Hopkins, P. E., T. Beechem, J. C. Duda, K. Hattar, J. F. Ihlefeld, M. A. Rodriguez, and E. S. Piekos, 2011, *Phys. Rev. B* **84**, 125408.
- Hopkins, P. E., T. E. Beechem, J. C. Duda, J. L. Smoyer, and P. M. Norris, 2010, *Appl. Phys. Lett.* **96**, 011907.
- Hopkins, P. E., J. C. Duda, and P. M. Norris, 2011, *J. Heat Transfer* **133**, 062401.
- Hopkins, P. E., J. C. Duda, C. W. Petz, and J. A. Floro, 2011, *Phys. Rev. B* **84**, 035438.
- Hopkins, P. E., J. L. Kassebaum, and P. M. Norris, 2009, *J. Appl. Phys.* **105**, 023710.
- Hopkins, P. E., and P. M. Norris, 2007a, *Nanoscale Microscale Thermophys. Eng.* **11**, 247.
- Hopkins, P. E., and P. M. Norris, 2007b, *Appl. Surf. Sci.* **253**, 6289.
- Hopkins, P. E., and P. M. Norris, 2009, *J. Heat Transfer* **131**, 022402.
- Hopkins, P. E., P. M. Norris, M. S. Tsegaye, and A. W. Ghosh, 2009, *J. Appl. Phys.* **106**, 063503.
- Hopkins, P. E., L. M. Phinney, J. R. Serrano, and T. E. Beechem, 2010, *Phys. Rev. B* **82**, 085307.
- Hsieh, W.-P., B. Chen, J. Li, P. Keblinski, and D. G. Cahill, 2009, *Phys. Rev. B* **80**, 180302.
- Hsieh, W.-P., A. S. Lyons, E. Pop, P. Keblinski, and D. G. Cahill, 2011, *Phys. Rev. B* **84**, 184107.
- Hu, M., and G. V. Hartland, 2002, *J. Phys. Chem. B* **106**, 7029.
- Hu, M., and G. V. Hartland, 2003, *J. Phys. Chem. B* **107**, 1284.
- Hu, S., Z. Zhang, P. Jiang, J. Chen, S. Volz, M. Nomura, and B. Li, 2018, *J. Phys. Chem. Lett.* **9**, 3959.
- Hu, S., Z. Zhang, P. Jiang, W. Ren, C. Yu, J. Shiomi, and J. Chen, 2019, *Nanoscale* **11**, 11839.
- Hu, Y., G. J. Stecher, T. J. Gramila, and R. C. Richardson, 1996, *Phys. Rev. B* **54**, R9639.
- Hu, Y., L. Zeng, A. J. Minnich, M. S. Dresselhaus, and G. Chen, 2015, *Nat. Nanotechnol.* **10**, 701.
- Hua, C., X. Chen, N. K. Ravichandran, and A. J. Minnich, 2017, *Phys. Rev. B* **95**, 205423.
- Huang, D., R. Ma, T. Zhang, and T. Luo, 2018, *ACS Appl. Mater. Interfaces* **10**, 28159.
- Huang, H. S., V. Varshney, J. L. Wohlwend, and A. K. Roy, 2012, *J. Nanotechnol. Eng. Med.* **3**, 031008.
- Huang, Z., J. Y. Murthy, and T. S. Fisher, 2011, *J. Heat Transfer* **133**, 114502.
- Huberman, M. L., and A. W. Overhauser, 1994, *Phys. Rev. B* **50**, 2865.
- Hung, S.-W., S. Hu, and J. Shiomi, 2019, *ACS Appl. Electron. Mater.* **1**, 2594.
- Huxtable, S. T., *et al.*, 2003, *Nat. Mater.* **2**, 731.
- Idrobo, J. C., A. R. Lupini, T. Feng, R. R. Unocic, F. S. Walden, D. S. Gardiner, T. C. Lovejoy, N. Dellby, S. T. Pantelides, and O. L. Krivanek, 2018, *Phys. Rev. Lett.* **120**, 095901.
- Issa, K. M., and A. A. Mohamad, 2012, *Phys. Rev. E* **85**, 031602.
- Jackson, J. M., and N. F. Mott, 1932, *Proc. R. Soc. A* **137**, 703.
- Jagannadham, K., 2010, *J. Appl. Phys.* **108**, 084905.
- Jeng, M.-S., R. Yang, D. Song, and G. Chen, 2008, *J. Heat Transfer* **130**, 042410.
- Jeong, M., J. P. Freedman, H. J. Liang, C.-M. Chow, V. M. Sokalski, J. A. Bain, and J. A. Malen, 2016, *Phys. Rev. Applied* **5**, 014009.
- Jia, L., S. Ju, X. Liang, and X. Zhang, 2016, *Mater. Res. Express* **3**, 095024.
- Jiang, P., S. Hu, Y. Ouyang, W. Ren, C. Yu, Z. Zhang, and J. Chen, 2020, *J. Appl. Phys.* **127**, 235101.
- Jiang, P., Y. Ouyang, W. Ren, C. Yu, J. He, and J. Chen, 2021, *APL Mater.* **9**, 040703.
- Jiang, P., X. Qian, and R. Yang, 2018, *J. Appl. Phys.* **124**, 161103.
- Jin, Y., C. Shao, J. Kieffer, K. P. Pipe, and M. Shtein, 2012, *J. Appl. Phys.* **112**, 093503.
- Jin, Y., A. Yadav, K. Sun, H. Sun, K. P. Pipe, and M. Shtein, 2011, *Appl. Phys. Lett.* **98**, 093305.
- Johnson, R. C., and W. A. Little, 1963, *Phys. Rev.* **130**, 596.
- Jones, R. E., J. C. Duda, X. W. Zhou, C. J. Kimmer, and P. E. Hopkins, 2013, *Appl. Phys. Lett.* **102**, 183119.
- Ju, S., B. Palpant, and Y. Chalopin, 2017, *J. Phys. Chem. C* **121**, 13474.
- Ju, S., T. Shiga, L. Feng, Z. Hou, K. Tsuda, and J. Shiomi, 2017, *Phys. Rev. X* **7**, 021024.
- Ju, Y., M. T. Hung, and T. Usui, 2006, *J. Heat Transfer* **128**, 919.
- Kaganov, M., E. Lifshitz, and L. Tanatarov, 1957, *Sov. Phys. JETP* **4**, 173.
- Kakodkar, R. R., and J. P. Feser, 2015, *J. Appl. Phys.* **118**, 094301.
- Kane, R. S., P. Deschatelets, and G. M. Whitesides, 2003, *Langmuir* **19**, 2388.
- Kapitza, P. L., 1941, *Zh. Eksp. Teor. Fiz.* **11**, 1 [*J. Phys. (Moscow)* **4**, 181 (1941)].
- Kaur, S., N. Raravikar, B. A. Helms, R. Prasher, and D. F. Ogletree, 2014, *Nat. Commun.* **5**, 3082.
- Kazan, M., 2009, *Appl. Phys. Lett.* **95**, 141904.
- Kazan, M., 2011, *J. Heat Transfer* **133**, 112401.
- Keesom, W. H., and A. P. Keesom, 1936, *Physica (Amsterdam)* **3**, 359.
- Khalatnikov, I., 1952, *Zh. Eksp. Teor. Fiz.* **23**, 169.
- Kim, B. H., A. Beskok, and T. Cagin, 2008, *J. Chem. Phys.* **129**, 174701.
- Kim, E. K., S. I. Kwun, S. M. Lee, H. Seo, and J. G. Yoon, 2000, *Appl. Phys. Lett.* **76**, 3864.
- Kim, P., L. Shi, A. Majumdar, and P. McEuen, 2001, *Phys. Rev. Lett.* **87**, 215502.
- Kim, S. E., *et al.*, 2021, *Nature (London)* **597**, 660.
- Kimling, J., A. Philippi-Kobs, J. Jacobsohn, H. P. Oepen, and D. G. Cahill, 2017, *Phys. Rev. B* **95**, 184305.
- Knudsen, M., 1911, *Ann. Phys. (Berlin)* **339**, 593.
- Koblinger, O., U. Heim, M. Welte, and W. Eisenmenger, 1983, *Phys. Rev. Lett.* **51**, 284.
- Koh, Y. K., M. H. Bae, D. G. Cahill, and E. Pop, 2010, *Nano Lett.* **10**, 4363.
- Koh, Y. K., and D. G. Cahill, 2007, *Phys. Rev. B* **76**, 075207.
- Koh, Y. K., Y. Cao, D. G. Cahill, and D. Jena, 2009, *Adv. Funct. Mater.* **19**, 610.
- Koh, Y. K., A. S. Lyons, M. H. Bae, B. Huang, V. E. Dorgan, D. G. Cahill, and E. Pop, 2016, *Nano Lett.* **16**, 6014.

- Koh, Y. R., *et al.*, 2020, *Phys. Rev. B* **102**, 205304.
- Kosevich, Y. A., 1995, *Phys. Rev. B* **52**, 1017.
- Kosevich, Y. A., L. G. Potyomina, A. N. Darinskii, and I. A. Strelnikov, 2018, *Phys. Rev. B* **97**, 094117.
- Kosevich, Y. A., E. S. Syrkin, and A. M. Kossevich, 1997, *Prog. Surf. Sci.* **55**, 59.
- Kouptsidis, J., and D. Menzei, 1970, *Ber. Bunsen-Ges. Phys. Chem.* **74**, 512.
- Kozorezov, A. G., J. K. Wigmore, C. Erd, A. Peacock, and A. Poelaert, 1998, *Phys. Rev. B* **57**, 7411.
- Kucsko, G., P. C. Maurer, N. Y. Yao, M. Kubo, H. J. Noh, P. K. Lo, H. Park, and M. D. Lukin, 2013, *Nature (London)* **500**, 54.
- Kuehn, K., S. Mehta, H. Fu, E. Genio, D. Murphy, F. Liu, Y. Liu, and G. Ahler, 2002, *Phys. Rev. Lett.* **88**, 095702.
- Kürti, N., B. V. Rollin, and F. Simon, 1936, *Physica (Amsterdam)* **3**, 266.
- Kwang, W.-Y., 1962, *Zh. Eksp. Teor. Fiz.* **42**, 921.
- Landry, E. S., and A. J. H. McGaughey, 2009, *Phys. Rev. B* **80**, 165304.
- Lapin, A. D., 1969, *Akust. Zh.* **15**, 387.
- Latour, B., N. Shulumba, and A. J. Minnich, 2017, *Phys. Rev. B* **96**, 104310.
- Lee, E., T. Zhang, T. Yoo, Z. Guo, and T. Luo, 2016, *ACS Appl. Mater. Interfaces* **8**, 35505.
- Lee, J., A. K. Roy, and B. L. Farmer, 2011, *Phys. Rev. E* **83**, 056706.
- Lee, S., *et al.*, 2015, *Nat. Commun.* **6**, 8573.
- Lee, S. M., and D. G. Cahill, 1997, *J. Appl. Phys.* **81**, 2590.
- Lee, S. M., D. G. Cahill, and R. Venkatasubramanian, 1997, *Appl. Phys. Lett.* **70**, 2957.
- Lemons, R. S., and G. M. Rosenblatt, 1975, *Surf. Sci.* **48**, 432.
- Li, B., J. Lan, and L. Wang, 2005, *Phys. Rev. Lett.* **95**, 104302.
- Li, B., L. Wang, and G. Casati, 2004, *Phys. Rev. Lett.* **93**, 184301.
- Li, C., and Z. Tian, 2019, *Front. Phys.* **7**, 3.
- Li, J., Z. Chi, R. Qin, L. Yan, X. Lin, M. Hu, G. Shan, H. Chen, and Y.-X. Weng, 2020, *J. Phys. Chem. C* **124**, 10306.
- Li, M., Y. Wang, J. Zhou, J. Ren, and B. Li, 2015, *Eur. Phys. J. B* **88**, 149.
- Li, N., J. Ren, L. Wang, G. Zhang, P. Hänggi, and B. Li, 2012, *Rev. Mod. Phys.* **84**, 1045.
- Li, X., J. Hong, and L. Zhang, 2020, *ACS Omega* **5**, 27164.
- Li, X., Y. Yan, L. Dong, J. Guo, A. Aiyiti, X. Xu, and B. Li, 2017, *J. Phys. D* **50**, 104002.
- Li, X., and R. Yang, 2012a, *Phys. Rev. B* **86**, 054305.
- Li, X., and R. Yang, 2012b, *J. Phys. Condens. Matter* **24**, 155302.
- Li, Y., W. Li, T. Han, X. Zheng, J. Li, B. Li, S. Fan, and C.-W. Qiu, 2021, *Nat. Rev. Mater.* **6**, 488.
- Liang, Z., W. Evans, T. Desai, and P. Keblinski, 2013, *Appl. Phys. Lett.* **102**, 061907.
- Liang, Z., W. Evans, and P. Keblinski, 2013, *Phys. Rev. E* **87**, 022119.
- Liang, Z., and M. Hu, 2018, *J. Appl. Phys.* **123**, 191101.
- Liang, Z., and P. Keblinski, 2014a, *Phys. Rev. B* **90**, 075411.
- Liang, Z., and P. Keblinski, 2014b, *Int. J. Heat Mass Transfer* **78**, 161.
- Liang, Z., K. Sasikumar, and P. Keblinski, 2014, *Phys. Rev. Lett.* **113**, 065901.
- Liang, Z., and H.-L. Tsai, 2011, *Phys. Rev. E* **83**, 041602.
- Liao, M., Q.-D. To, C. Léonard, and W. Yang, 2018, *Phys. Rev. E* **98**, 042104.
- Lindsay, L., and D. A. Broido, 2011, *Phys. Rev. B* **84**, 155421.
- Link, S., D. J. Hathcock, B. Nikoobakht, and M. A. El-Sayed, 2003, *Adv. Mater.* **15**, 393.
- Lipa, J. A., and Q. Li, 2007, *J. Low Temp. Phys.* **149**, 1.
- Little, W. A., 1959, *Can. J. Phys.* **37**, 334.
- Liu, B., Y. Chen, and X. Xu, 2021, *Nanoscale* **13**, 13641.
- Liu, D., X. Chen, Y. Zhang, D. Wang, Y. Zhao, H. Peng, Y. Liu, X. Xu, A. T. S. Wee, and D. Wei, 2020, *Adv. Electron. Mater.* **6**, 2000059.
- Liu, D., R. Xie, N. Yang, B. Li, and J. T. L. Thong, 2014, *Nano Lett.* **14**, 806.
- Liu, D., *et al.*, 2019, *Nat. Commun.* **10**, 1188.
- Liu, J., G.-M. Choi, and D. G. Cahill, 2014, *J. Appl. Phys.* **116**, 233107.
- Liu, X., J. Gao, G. Zhang, and Y.-W. Zhang, 2018, *Nanoscale* **10**, 19854.
- Liu, X., G. Zhang, and Y. W. Zhang, 2016, *Nano Lett.* **16**, 4954.
- Loh, G. C., B. K. Tay, and E. H. T. Teo, 2010, *Appl. Phys. Lett.* **97**, 121917.
- Lombard, J., F. Detcheverry, and S. Merabia, 2015, *J. Phys. Condens. Matter* **27**, 015007.
- Losego, M. D., M. E. Grady, N. R. Sottos, D. G. Cahill, and P. V. Braun, 2012, *Nat. Mater.* **11**, 502.
- Lu, L., G. Xiong, Y. Huang, D. Ma, M. Zhong, and L. Zhang, 2020, *J. Phys. Condens. Matter* **32**, 19LT02.
- Lu, S., Y. Ouyang, C. Yu, P. Jiang, J. He, and J. Chen, 2021, *J. Appl. Phys.* **129**, 225106.
- Lu, T., J. Zhou, T. Nakayama, R. Yang, and B. Li, 2016, *Phys. Rev. B* **93**, 085433.
- Lu, T. F., Y. S. Wang, J. A. Tomko, P. E. Hopkins, H. X. Zhang, and O. V. Prezhdo, 2020, *J. Phys. Chem. Lett.* **11**, 1419.
- Lu, Z., T. R. Salamon, S. Narayanan, K. R. Bagnall, D. F. Hanks, D. S. Antao, B. Barabadi, J. Sircar, M. E. Simon, and E. N. Wang, 2019, *IEEE Trans. Compon. Packag. Manuf. Technol.* **9**, 1663.
- Lu, Z., Y. Wang, and X. Ruan, 2016, *Phys. Rev. B* **93**, 064302.
- Luckyanova, M. N., *et al.*, 2012, *Science* **338**, 936.
- Lumpkin, M. E., W. M. Saslow, and W. M. Visscher, 1978, *Phys. Rev. B* **17**, 4295.
- Lyeo, H.-K., and D. G. Cahill, 2006, *Phys. Rev. B* **73**, 144301.
- Ma, D., and L. Zhang, 2020, *J. Phys. Condens. Matter* **32**, 425001.
- Ma, Y., Z. Zhang, J. Chen, K. Sääskilähti, S. Volz, and J. Chen, 2018, *Carbon* **135**, 263.
- Mahan, G. D., 2009, *Phys. Rev. B* **79**, 075408.
- Mahan, G. D., and M. Bartkowiak, 1999, *Appl. Phys. Lett.* **74**, 953.
- Maiti, A., G. D. Mahan, and S. T. Pantelides, 1997, *Solid State Commun.* **102**, 517.
- Majumdar, A., and P. Reddy, 2004, *Appl. Phys. Lett.* **84**, 4768.
- Majumdar, S., J. A. Malen, and A. J. H. McGaughey, 2017, *Nano Lett.* **17**, 220.
- Majumdar, S., J. A. Sierra-Suarez, S. N. Schiffres, W. Ong, C. F. Higgs III, A. J. H. McGaughey, and J. A. Malen, 2015, *Nano Lett.* **15**, 2985.
- Malen, J. A., K. Baheti, T. Tong, Y. Zhao, J. A. Hudgings, and A. Majumdar, 2011, *J. Heat Transfer* **133**, 081601.
- Mao, R., B. D. Kong, C. Gong, S. Xu, T. Jayasekera, K. Cho, and K. W. Kim, 2013, *Phys. Rev. B* **87**, 165410.
- Marconnet, A. M., M. A. Panzer, and K. E. Goodson, 2013, *Rev. Mod. Phys.* **85**, 1295.
- Marx, D., and W. Eisenmenger, 1982, *Z. Phys. B* **48**, 277.
- Matsumoto, D. S., C. L. Reynolds, Jr., and A. C. Anderson, 1977, *Phys. Rev. B* **16**, 3303.
- Maune, H., H. Y. Chiu, and M. Bockrath, 2006, *Appl. Phys. Lett.* **89**, 013109.
- Maxwell, J. C., 1879, *Phil. Trans. R. Soc. London* **170**, 231.
- Mazo, R. M., 1955, Ph.D. thesis (Yale University).
- McGaughey, A. J. H., and J. M. Larkin, 2014, *Annu. Rev. Heat Transfer* **17**, 49.

- Merabia, S., J. Lombard, and A. Alkurdi, 2016, *Int. J. Heat Mass Transfer* **100**, 287.
- Merabia, S., and K. Termentzidis, 2012, *Phys. Rev. B* **86**, 094303.
- Merabia, S., and K. Termentzidis, 2014, *Phys. Rev. B* **89**, 054309.
- Mester, J. C., E. S. Meyer, M. W. Reynolds, T. E. Huber, and I. F. Silvera, 1992, *Phys. Rev. Lett.* **68**, 3068.
- Mingo, N., 2006, *Phys. Rev. B* **74**, 125402.
- Minnich, A. J., J. A. Johnson, A. J. Schmidt, K. Esfarjani, M. S. Dresselhaus, K. A. Nelson, and G. Chen, 2011, *Phys. Rev. Lett.* **107**, 095901.
- Mittal, J., and G. Hummer, 2010, *Faraday Discuss.* **146**, 341.
- Mohamed, M. B., V. Volkov, S. Link, and M. A. El-Sayed, 2000, *Chem. Phys. Lett.* **317**, 517.
- Monachon, C., L. Weber, and C. Dames, 2016, *Annu. Rev. Mater. Res.* **46**, 433.
- Mu, X., T. Zhang, D. B. Go, and T. Luo, 2015, *Carbon* **83**, 208.
- Murad, S., and I. K. Puri, 2008, *Appl. Phys. Lett.* **92**, 133105.
- Nakayama, T., 1977, *J. Phys. C* **10**, 3273.
- Nakayama, T., 1985a, *Phys. Rev. B* **32**, 777.
- Nakayama, T., 1985b, *J. Phys. C* **18**, L667.
- Nakayama, T., 1986, *Phys. Rev. B* **33**, 8664.
- Nakayama, T., 1988, *Phys. Rev. B* **37**, 5958.
- Nakayama, T., 1989, in *Progress in Low Temperature Physics*, Vol. 12, edited by D. F. Brewer (Elsevier, Amsterdam), pp. 115–194.
- Nassar, H., B. Yousefzadeh, R. Fleury, M. Ruzzene, A. Alù, C. Daraio, A. N. Norris, G. Huang, and M. R. Haberman, 2020, *Nat. Rev. Mater.* **5**, 667.
- Neeper, D. A., and J. R. Dillinger, 1964, *Phys. Rev.* **135**, A1028.
- Neumann, C. M., K. L. Okabe, E. Yalon, R. W. Grady, H. S. P. Wong, and E. Pop, 2019, *Appl. Phys. Lett.* **114**, 082103.
- Nishiguchi, N., and T. Nakayama, 1982, *Phys. Rev. B* **25**, 5720.
- Nishiguchi, N., and T. Nakayama, 1983, *Solid State Commun.* **45**, 877.
- Nitsche, F., and B. Schumann, 1980, *J. Low Temp. Phys.* **39**, 119.
- Nosé, S., 1984, *J. Chem. Phys.* **81**, 511.
- O'Brien, P. J., S. Shenogin, J. Liu, P. K. Chow, D. Laurencin, P. H. Mutin, M. Yamaguchi, P. Keblinski, and G. Ramanath, 2013, *Nat. Mater.* **12**, 118.
- Ohnishi, M., and J. Shiomi, 2019, *APL Mater.* **7**, 013102.
- Olafsen, J. S., and R. P. Behringer, 1995, *Phys. Rev. B* **52**, 61.
- Olson, D. H., K. M. Freedy, S. J. McDonnell, and P. E. Hopkins, 2018, *Appl. Phys. Lett.* **112**, 171602.
- Olson, D. H., M. G. Sales, J. A. Tomko, T.-F. Lu, O. V. Prezhdo, S. J. McDonnell, and P. E. Hopkins, 2021, *Appl. Phys. Lett.* **118**, 163503.
- Olson, J. R., and R. O. Pohl, 1994, *J. Low Temp. Phys.* **94**, 539.
- Ong, Z.-Y., 2018a, *Phys. Rev. B* **98**, 195301.
- Ong, Z.-Y., 2018b, *J. Appl. Phys.* **124**, 151101.
- Ong, Z.-Y., M. V. Fischetti, A. Y. Serov, and E. Pop, 2013, *Phys. Rev. B* **87**, 195404.
- Ong, Z.-Y., B. Qiu, S. Xu, X. Ruan, and E. Pop, 2018, *J. Appl. Phys.* **123**, 115107.
- Ong, Z.-Y., and G. Zhang, 2015, *Phys. Rev. B* **91**, 174302.
- Ong, Z.-Y., G. Zhang, and Y.-W. Zhang, 2016, *Phys. Rev. B* **93**, 075406.
- Ordonez-Miranda, J., J. J. Alvarado-Gil, and R. G. Yang, 2011, *J. Appl. Phys.* **109**, 094310.
- Osborne, D. V., 1951, *Proc. Phys. Soc. London Sect. A* **64**, 114.
- Osheroff, D. D., and L. R. Corruccini, 1981, *Phys. Lett.* **82A**, 38.
- Osheroff, D. D., and R. C. Richardson, 1985, *Phys. Rev. Lett.* **54**, 1178.
- Ouyang, Y., C. Yu, J. He, P. Jiang, W. Ren, and J. Chen, 2022, *Phys. Rev. B* **105**, 115202.
- Ouyang, Y., C. Yu, G. Yan, and J. Chen, 2021, *Front. Phys.* **16**, 43200.
- Ouyang, Y., Z. Zhang, C. Yu, J. He, G. Yan, and J. Chen, 2020, *Chin. Phys. Lett.* **37**, 126301.
- Paddock, C. A., and G. L. Eesley, 1986, *J. Appl. Phys.* **60**, 285.
- Papk, B. P., and Y. Narahara, 1971, *J. Phys. Soc. Jpn.* **30**, 760.
- Paranjape, B. V., N. Arimitsu, and E. S. Krebes, 1987, *J. Appl. Phys.* **61**, 888.
- Park, J., J. Huang, W. Wang, C. J. Murphy, and D. G. Cahill, 2012, *J. Phys. Chem. C* **116**, 26335.
- Park, W., T. Kodama, J. Park, J. Cho, A. Sood, M. T. Barako, M. Asheghi, and K. E. Goodson, 2017, *ACS Appl. Mater. Interfaces* **9**, 30100.
- Park, W., A. Sood, J. Park, M. Asheghi, R. Sinclair, and K. E. Goodson, 2017, *Nanoscale Microscale Thermophys. Eng.* **21**, 134.
- Peng, H. B., C. W. Chang, S. Aloni, T. D. Yuzvinsky, and A. Zettl, 2006, *Phys. Rev. Lett.* **97**, 087203.
- Peng, X., P. Jiang, Y. Ouyang, S. Lu, W. Ren, and J. Chen, 2022, *Nanotechnology* **33**, 035707.
- Péraud, J.-P. M., and N. G. Hadjiconstantinou, 2011, *Phys. Rev. B* **84**, 205331.
- Pernot, G., *et al.*, 2010, *Nat. Mater.* **9**, 491.
- Persson, B. N. J., A. I. Volokitin, and H. Ueba, 2011, *J. Phys. Condens. Matter* **23**, 045009.
- Perterson, R. E., and A. C. Anderson, 1972, *Solid State Commun.* **10**, 891.
- Perterson, R. E., and A. C. Anderson, 1973, *J. Low Temp. Phys.* **11**, 639.
- Pettersson, S., and G. D. Mahan, 1990, *Phys. Rev. B* **42**, 7386.
- Pettes, M., I. Jo, Z. Yao, and L. Shi, 2011, *Nano Lett.* **11**, 1195.
- Pham, A., M. Barisik, and B. Kim, 2013, *J. Chem. Phys.* **139**, 244702.
- Phillips, C. L., and P. S. Crozier, 2009, *J. Chem. Phys.* **131**, 074701.
- Pinki, P. Kulkarni, and D. S. Sundaram, 2020, *J. Phys. Chem. C* **124**, 7182.
- Plech, A., V. Kotaidis, S. Grésillon, C. Dahmen, and G. von Plessen, 2004, *Phys. Rev. B* **70**, 195423.
- Poisson, S.-D., 1835, *Théorie Mathématique de la Chaleur* (Bachelier, Paris).
- Polanco, C. A., and L. Lindsay, 2019, *Phys. Rev. B* **99**, 075202.
- Polanco, C. A., R. Rastgarkafshgarkolaei, J. Zhang, N. Q. Le, P. M. Norris, and A. W. Ghosh, 2017, *Phys. Rev. B* **95**, 195303.
- Pollack, G. L., 1969, *Rev. Mod. Phys.* **41**, 48.
- Prasher, R., 2009, *Appl. Phys. Lett.* **94**, 041905.
- Prasher, R. S., and P. E. Phelan, 2001, *J. Heat Transfer* **123**, 105.
- Qi, R., *et al.*, 2021, *Nature (London)* **599**, 399.
- Quimby, R. S., and W. M. Yen, 1981, *J. Appl. Phys.* **52**, 500.
- Ramire, A., J. A. Amrit, and S. Volz, 2012, *J. Phys. Conf. Ser.* **395**, 012110.
- Ramire, A., S. Volz, and J. A. Amrit, 2016, *Nat. Mater.* **15**, 512.
- Ramos-Alvarado, B., and S. Kumar, 2017, *J. Phys. Chem. C* **121**, 11380.
- Ramos-Alvarado, B., S. Kumar, and G. P. Peterson, 2016, *J. Phys. Chem. Lett.* **7**, 3497.
- Ran, X., Y. Guo, Z. Hu, and M. Wang, 2018, *Front. Energy Res.* **6**, 28.
- Ran, X., Y. Guo, and M. Wang, 2018, *Int. J. Heat Mass Transfer* **123**, 616.
- Rastgarkafshgarkolaei, R., J. Zhang, C. A. Polanco, N. Q. Le, A. W. Ghosh, and P. M. Norris, 2019, *Nanoscale* **11**, 6254.
- Ravichandran, J., *et al.*, 2014, *Nat. Mater.* **13**, 168.
- Regner, K. T., S. Majumdar, and J. A. Malen, 2013, *Rev. Sci. Instrum.* **84**, 064901.

- Regner, K. T., D. P. Sellan, Z. H. Su, C. H. Amon, A. J. H. McGaughey, and J. A. Malen, 2013, *Nat. Commun.* **4**, 1640.
- Ren, W., Y. Ouyang, P. Jiang, C. Yu, J. He, and J. Chen, 2021, *Nano Lett.* **21**, 2634.
- Rosencwaig, A., 1982, *Science* **218**, 223.
- Rosencwaig, A., and A. Gersho, 1976, *J. Appl. Phys.* **47**, 64.
- Rosenthal, L. A., 1961, *Rev. Sci. Instrum.* **32**, 1033.
- Sääskilähti, K., J. Oksanen, J. Tulkki, and S. Volz, 2014, *Phys. Rev. B* **90**, 134312.
- Sääskilähti, K., J. Oksanen, J. Tulkki, and S. Volz, 2016, *Phys. Rev. E* **93**, 052141.
- Sääskilähti, K., J. Oksanen, S. Volz, and J. Tulkki, 2015, *Phys. Rev. B* **91**, 115426.
- Sadasivam, S., U. V. Waghmare, and T. S. Fisher, 2015, *J. Appl. Phys.* **117**, 134502.
- Sadasivam, S., U. V. Waghmare, and T. S. Fisher, 2017, *Phys. Rev. B* **96**, 174302.
- Sadasivam, S., N. Ye, J. P. Feser, J. Charles, K. Miao, T. Kubis, and T. S. Fisher, 2017, *Phys. Rev. B* **95**, 085310.
- Sadeghi, M. M., I. Jo, and L. Shi, 2013, *Proc. Natl. Acad. Sci. U.S.A.* **110**, 16321.
- Sahling, S., J. Engert, A. Gladun, and R. Knöner, 1981, *J. Low Temp. Phys.* **45**, 457.
- Sahoo, S., A. P. S. Gaur, M. Ahmadi, M. J. F. Guinel, and R. S. Katiyar, 2013, *J. Phys. Chem. C* **117**, 9042.
- Sánchez, D., and R. López, 2013, *Phys. Rev. Lett.* **110**, 026804.
- Schelling, P. K., S. R. Phillpot, and P. Keblinski, 2002a, *Phys. Rev. B* **65**, 144306.
- Schelling, P. K., S. R. Phillpot, and P. Keblinski, 2002b, *Appl. Phys. Lett.* **80**, 2484.
- Schelling, P. K., S. R. Phillpot, and P. Keblinski, 2004, *J. Appl. Phys.* **95**, 6082.
- Schiffres, S. N., K. H. Kim, L. Hu, A. J. H. McGaughey, M. F. Islam, and J. A. Malen, 2012, *Adv. Funct. Mater.* **22**, 5251.
- Schmidt, A. J., 2008, Ph.D. thesis (Massachusetts Institute of Technology).
- Schmidt, A. J., R. Cheaito, and M. Chiesa, 2009, *Rev. Sci. Instrum.* **80**, 094901.
- Schmidt, A. J., X. Chen, and G. Chen, 2008, *Rev. Sci. Instrum.* **79**, 114902.
- Schmidt, A. J., K. C. Collins, A. J. Minnich, and G. Chen, 2010, *J. Appl. Phys.* **107**, 104907.
- Schmidt, C., and E. Umlauf, 1976, *J. Low Temp. Phys.* **22**, 597.
- Schwab, K., E. Henriksen, J. Worlock, and M. L. Roukes, 2000, *Nature (London)* **404**, 974.
- Sellan, D. P., E. S. Landry, J. E. Turney, A. J. H. McGaughey, and C. H. Amon, 2010, *Phys. Rev. B* **81**, 214305.
- Sergeev, A. V., 1998, *Phys. Rev. B* **58**, R10199.
- Sheard, F. W., and G. A. Toombs, 1972a, *J. Phys. (Paris)*, Colloq. **33**, C4-61.
- Sheard, F. W., and G. A. Toombs, 1972b, *J. Phys. C* **5**, L166.
- Shen, M., W. J. Evans, D. Cahill, and P. Keblinski, 2011, *Phys. Rev. B* **84**, 195432.
- Shenogin, S., P. Keblinski, D. Bedrov, and G. D. Smith, 2006, *J. Chem. Phys.* **124**, 014702.
- Shenogin, S., L. Xue, R. Ozisik, P. Keblinski, and D. G. Cahill, 2004, *J. Appl. Phys.* **95**, 8136.
- Shenogina, N., R. Godawat, P. Keblinski, and S. Garde, 2009, *Phys. Rev. Lett.* **102**, 156101.
- Shi, B., L. Dong, M. Li, B. Liu, K. Kim, X. Xu, J. Zhou, and J. Liu, 2018, *Appl. Phys. Lett.* **113**, 041902.
- Shi, B., X. Tang, T. Lu, T. Nakayama, Y. Li, and J. Zhou, 2018, *Mod. Phys. Lett. B* **32**, 1830004.
- Shi, L., D. Li, C. Yu, W. Jang, D. Kim, Z. Yao, P. Kim, and A. Majumdar, 2003, *J. Heat Transfer* **125**, 881.
- Shibahara, M., and K. Takeuchi, 2009, *J. Phys. Conf. Ser.* **191**, 012008.
- Shields, F. D., and J. Faughn, 1969, *J. Acoust. Soc. Am.* **46**, 158.
- Shiren, N. S., 1981, *Phys. Rev. Lett.* **47**, 1466.
- Simkin, M. V., and G. D. Mahan, 2000, *Phys. Rev. Lett.* **84**, 927.
- Singh, D., X. Guo, A. Alexeenko, J. Y. Murthy, and T. S. Fisher, 2009, *J. Appl. Phys.* **106**, 024314.
- Singh, D., J. Y. Murthy, and T. S. Fisher, 2011, *J. Heat Transfer* **133**, 122401.
- Singh, P., M. Seong, and S. Sinha, 2013, *Appl. Phys. Lett.* **102**, 181906.
- Smoluchowski, M., 1898, *London, Edinburgh Dublin Philos. Mag. J. Sci.* **46**, 192.
- Son, Y., S. K. Pal, T. Borca-Tasciuc, P. M. Ajayan, and R. W. Siegel, 2008, *J. Appl. Phys.* **103**, 024911.
- Sood, A., F. Xiong, S. Chen, R. Cheaito, F. Lian, M. Asheghi, Y. Cui, D. Donadio, K. E. Goodson, and E. Pop, 2019, *Nano Lett.* **19**, 2434.
- Stecher, G. J., Y. Hu, T. J. Gramila, and R. C. Richardson, 1990, *Physica (Amsterdam)* **165B-166B**, 525.
- Steinbrüchel, C., 1976, *Z. Phys. B* **24**, 293.
- Stevens, R. J., A. N. Smith, and P. M. Norris, 2005, *J. Heat Transfer* **127**, 315.
- Stevens, R. J., L. V. Zhigilei, and P. M. Norris, 2007, *Int. J. Heat Mass Transfer* **50**, 3977.
- Stocker, K. M., and J. D. Gezelter, 2013, *J. Phys. Chem. C* **117**, 7605.
- Stocker, K. M., S. M. Neidhart, and J. D. Gezelter, 2016, *J. Appl. Phys.* **119**, 025106.
- Stoner, R. J., and H. J. Maris, 1993, *Phys. Rev. B* **48**, 16373.
- Stoner, R. J., H. J. Maris, T. R. Anthony, and W. F. Banholzer, 1992, *Phys. Rev. Lett.* **68**, 1563.
- Sun, Z., K. Yuan, X. Zhang, and D. Tang, 2019, *Phys. Chem. Chem. Phys.* **21**, 6011.
- Surblyis, D., Y. Kawagoe, M. Shibahara, and T. Ohara, 2019, *J. Chem. Phys.* **150**, 114705.
- Suryavanshi, S. V., A. J. Gabourie, A. B. Farimani, and E. Pop, 2019, *J. Appl. Phys.* **126**, 055107.
- Swartz, E. T., and R. O. Pohl, 1987, *Appl. Phys. Lett.* **51**, 2200.
- Swartz, E. T., and R. O. Pohl, 1989, *Rev. Mod. Phys.* **61**, 605.
- Tam, W. Y., and G. Ahlers, 1986, *Phys. Rev. B* **33**, 183.
- Taube, A., J. Judek, A. Lapińska, and M. Zdrojek, 2015, *ACS Appl. Mater. Interfaces* **7**, 5061.
- Thomas, L. B., 1967, in *Rarefied Gas Dynamics*, Vol. 1, edited by C. L. Brundin (Academic Press, San Diego), p. 155.
- Thomsen, C., J. Strait, Z. Vardeny, H. J. Maris, J. Tauc, and J. J. Hauser, 1984, *Phys. Rev. Lett.* **53**, 989.
- Tian, Z., K. Esfarjani, and G. Chen, 2012, *Phys. Rev. B* **86**, 235304.
- Tian, Z., K. Esfarjani, and G. Chen, 2014, *Phys. Rev. B* **89**, 235307.
- Tian, Z., A. Marconnet, and G. Chen, 2015, *Appl. Phys. Lett.* **106**, 211602.
- Tong, H., F. Lan, Y. J. Liu, L. J. Zhou, X. J. Wang, Q. He, K. Z. Wang, and X. S. Miao, 2017, *J. Phys. D* **50**, 355102.
- Toombs, G. A., F. W. Sheard, and M. J. Rice, 1980, *J. Low Temp. Phys.* **39**, 273.
- Trott, W. M., J. N. Castañeda, J. R. Torczynski, M. A. Gallis, and D. J. Rader, 2011, *Rev. Sci. Instrum.* **82**, 035120.
- van Beelen, H., R. W. A. van der Laar, and A. van der Hoek, 1994, *Physica (Amsterdam)* **194B-196B**, 669.
- Van den Brink, A. M., and H. Dekker, 1996, *Physica (Amsterdam)* **226A**, 64.

- van der Hoek, A., and H. van Beelen, 2001, *Physica (Amsterdam)* **293B**, 297.
- Vardeman, C. F., and J. D. Gezelter, 2008, *J. Phys. Chem. C* **112**, 3283.
- Venkatasubramanian, R., 2000, *Phys. Rev. B* **61**, 3091.
- Vermeersch, B., A. M. S. Mohammed, G. Pernot, Y. R. Koh, and A. Shakouri, 2014, *Phys. Rev. B* **90**, 014306.
- Wagner, F., F. J. Kollarits, and M. Yaqub, 1974, *Phys. Rev. Lett.* **32**, 1117.
- Wagner, F., and M. Yaqub, 1975, *J. Phys. Condens. Matter* **19**, 337.
- Waldrop, M. M., 2016, *Nature (London)* **530**, 144.
- Wan, X., W. Feng, Y. Wang, H. Wang, X. Zhang, C. Deng, and N. Yang, 2019, *Nano Lett.* **19**, 3387.
- Wang, C., J. Guo, L. Dong, A. Aiyiti, X. Xu, and B. Li, 2016, *Sci. Rep.* **6**, 25334.
- Wang, H., S. Hu, K. Takahashi, X. Zhang, H. Takamatsu, and J. Chen, 2017, *Nat. Commun.* **8**, 15843.
- Wang, J., and J.-S. Wang, 2007, *J. Phys. Condens. Matter* **19**, 236211.
- Wang, J., Z. Zhang, R. Shi, B. N. Chandrashekar, N. Shen, H. Song, N. Wang, J. Chen, and C. Cheng, 2020, *Adv. Mater. Interfaces* **7**, 1901582.
- Wang, J.-S., B. K. Agarwalla, H. Li, and J. Thingna, 2014, *Front. Phys.* **9**, 673.
- Wang, J.-S., J. Wang, and J. T. Lü, 2008, *Eur. Phys. J. B* **62**, 381.
- Wang, J.-S., J. Wang, and N. Zeng, 2006, *Phys. Rev. B* **74**, 033408.
- Wang, J.-S., N. Zeng, J. Wang, and C. K. Gan, 2007, *Phys. Rev. E* **75**, 061128.
- Wang, L., and B. Li, 2006, *Phys. Rev. B* **74**, 134204.
- Wang, Q., Y. Chen, A. Aiyiti, M. Zheng, N. Li, and X. Xu, 2020, *Chin. Phys. B* **29**, 084402.
- Wang, Q., X. Liang, B. Liu, Y. Song, G. Gao, and X. Xu, 2020, *Nanoscale* **12**, 1138.
- Wang, W., and D. G. Cahill, 2012, *Phys. Rev. Lett.* **109**, 175503.
- Wang, Y., and P. Keblinski, 2011, *Appl. Phys. Lett.* **99**, 073112.
- Wang, Y., Z. Qin, M. J. Buehler, and Z. Xu, 2016, *Nat. Commun.* **7**, 12854.
- Wang, Y., X. Ruan, and A. K. Roy, 2012, *Phys. Rev. B* **85**, 205311.
- Wang, Z., R. Xie, C. T. Bui, D. Liu, X. Ni, B. Li, and J. T. Thong, 2011, *Nano Lett.* **11**, 113.
- Weber, J., W. Sandman, W. Dietsche, and H. Kinder, 1978, *Phys. Rev. Lett.* **40**, 1469.
- Wehmeyer, G., T. Yabuki, C. Monachon, J. Wu, and C. Dames, 2017, *Appl. Phys. Rev.* **4**, 041304.
- Wei, C., X. Zheng, D. G. Cahill, and J. C. Zhao, 2013, *Rev. Sci. Instrum.* **84**, 071301.
- Wei, X., and T. Luo, 2019, *J. Appl. Phys.* **126**, 015301.
- Wei, X., Y. Wang, Y. Shen, G. Xie, H. Xiao, J. Zhong, and G. Zhang, 2014, *Appl. Phys. Lett.* **105**, 103902.
- Wei, Z., J. Yang, W. Chen, K. Bi, D. Li, and Y. Chen, 2014, *Appl. Phys. Lett.* **104**, 081903.
- Wheatley, J. C., R. E. Rapp, and R. T. Johnson, 1971, *J. Low Temp. Phys.* **4**, 1.
- Wilson, O. M., X. Hu, D. G. Cahill, and P. V. Braun, 2002, *Phys. Rev. B* **66**, 224301.
- Wilson, R. B., B. A. Apgar, W.-P. Hsieh, L. W. Martin, and D. G. Cahill, 2015, *Phys. Rev. B* **91**, 115414.
- Wilson, R. B., B. A. Apgar, L. W. Martin, and D. G. Cahill, 2012, *Opt. Express* **20**, 28829.
- Wilson, R. B., and D. G. Cahill, 2012, *Phys. Rev. Lett.* **108**, 255901.
- Wolfmeyer, M. W., G. T. Fox, and J. R. Dillinger, 1970, *Phys. Lett.* **31A**, 401.
- Wright, O. B., and K. Kawashima, 1992, *Phys. Rev. Lett.* **69**, 1668.
- Wu, X., and T. Luo, 2015, *Europhys. Lett.* **110**, 67004.
- Wu, X., Y. Ni, J. Zhu, N. D. Burrows, C. J. Murphy, T. Dumitrica, and X. Wang, 2016, *ACS Appl. Mater. Interfaces* **8**, 10581.
- Wu, X., Q. Tao, D. Li, Q. Wang, X. Zhang, H. Jin, J. Li, S. Wang, and X. Xu, 2021, *Nano Res.* **14**, 4725.
- Wu, X.-S., W.-T. Tang, and X.-F. Xu, 2020, *Acta Phys. Sin.* **69**, 196602.
- Wyatt, A. F. G., 1992, *Phys. Rev. Lett.* **69**, 1785.
- Wyatt, A. F. G., and G. J. Page, 1978, *J. Phys. C* **11**, 4927.
- Xi, Q., Y. Y. Li, J. Zhou, B. W. Li, and J. Liu, 2019, *Int. J. Mod. Phys. C* **30**, 1950024.
- Xi, Q., J. X. Zhong, J. X. He, X. F. Xu, T. Nakayama, Y. Y. Wang, J. Liu, J. Zhou, and B. Li, 2020, *Chin. Phys. Lett.* **37**, 104401.
- Xiong, G., J.-S. Wang, D. Ma, and L. Zhang, 2020, *Europhys. Lett.* **128**, 54007.
- Xiong, Y., X. Yu, Y. Huang, J. Yang, L. Li, N. Yang, and D. Xu, 2019, *Mater. Today Phys.* **11**, 100139.
- Xu, X., J. Chen, and B. Li, 2016, *J. Phys. Condens. Matter* **28**, 483001.
- Xu, X., *et al.*, 2014, *Nat. Commun.* **5**, 3689.
- Xue, L., P. Keblinski, S. R. Phillpot, S. U. S. Choi, and J. A. Eastman, 2003, *J. Chem. Phys.* **118**, 337.
- Xue, L., P. Keblinski, S. R. Phillpot, S. U. S. Choi, and J. A. Eastman, 2004, *Int. J. Heat Mass Transfer* **47**, 4277.
- Yalamarthy, A. S., H. So, M. M. Rojo, A. J. Suria, X. Xu, E. Pop, and D. G. Senesky, 2018, *Adv. Funct. Mater.* **28**, 1705823.
- Yalon, E., *et al.*, 2017a, *ACS Appl. Mater. Interfaces* **9**, 43013.
- Yalon, E., *et al.*, 2017b, *Nano Lett.* **17**, 3429.
- Yamaguchi, H., K. Kanazawa, Y. Matsuda, T. Niimi, A. Polikarpov, and I. Graur, 2012, *Phys. Fluids* **24**, 062002.
- Yan, R., J. R. Simpson, S. Bertolazzi, J. Brivio, M. Watson, X. Wu, A. Kis, T. Luo, A. R. H. Walker, and H. G. Xing, 2014, *ACS Nano* **8**, 986.
- Yan, Z., L. Chen, M. Yoon, and S. Kumar, 2016, *ACS Appl. Mater. Interfaces* **8**, 33299.
- Yang, B., and G. Chen, 2003, *Phys. Rev. B* **67**, 195311.
- Yang, J., S. Waltermire, Y. Chen, A. A. Zinn, T. T. Xu, and D. Li, 2010, *Appl. Phys. Lett.* **96**, 023109.
- Yang, J., E. Ziade, C. Maragliano, R. Crowder, X. Wang, M. Stefancich, M. Chiesa, A. K. Swan, and A. J. Schmidt, 2014, *J. Appl. Phys.* **116**, 023515.
- Yang, J., E. Ziade, and A. J. Schmidt, 2016, *Rev. Sci. Instrum.* **87**, 014901.
- Yang, J., *et al.*, 2014, *Phys. Rev. Lett.* **112**, 205901.
- Yang, L., B. Latour, and A. J. Minnich, 2018, *Phys. Rev. B* **97**, 205306.
- Yang, L., and A. J. Minnich, 2017, *Sci. Rep.* **7**, 44254.
- Yang, L., X. Wan, D. Ma, Y. Jiang, and N. Yang, 2021, *Phys. Rev. B* **103**, 155305.
- Yasaei, P., *et al.*, 2017, *Adv. Mater. Interfaces* **4**, 1700334.
- Young, D. A., and H. J. Maris, 1989, *Phys. Rev. B* **40**, 3685.
- Yuan, P., J. Y. Wu, D. F. Ogletree, J. J. Urban, C. Dames, and Y. Ma, 2020, *Nano Lett.* **20**, 3019.
- Yue, Q. L., C. X. He, M. C. Wu, and T. S. Zhao, 2021, *Int. J. Heat Mass Transfer* **181**, 121853.
- Zang, Y., *et al.*, 2022, *Adv. Mater.* **34**, e2105778.
- Zhang, C., Y. Chen, and G. P. Peterson, 2014, *Phys. Rev. E* **89**, 062407.
- Zhang, C., W. Zhao, K. Bi, J. Ma, J. Wang, Z. Ni, Z. Ni, and Y. Chen, 2013, *Carbon* **64**, 61.
- Zhang, C., *et al.*, 2017, *Carbon* **115**, 665.
- Zhang, L., P. Keblinski, J.-S. Wang, and B. Li, 2011, *Phys. Rev. B* **83**, 064303.

- Zhang, L., J.-T. Lü, J.-S. Wang, and B. Li, 2013, *J. Phys. Condens. Matter* **25**, 445801.
- Zhang, L., J. Thingna, D. He, J.-S. Wang, and B. Li, 2013, *Europhys. Lett.* **103**, 64002.
- Zhang, T., A. R. Gans-Forrest, E. Lee, X. Zhang, C. Qu, Y. Pang, F. Sun, and T. Luo, 2016, *ACS Appl. Mater. Interfaces* **8**, 33326.
- Zhang, W., T. Fisher, and N. Mingo, 2007a, *Numer. Heat Transfer, Part B* **51**, 333.
- Zhang, W., T. S. Fisher, and N. Mingo, 2007b, *J. Heat Transfer* **129**, 483.
- Zhang, X., M. Hu, and D. Tang, 2013, *J. Appl. Phys.* **113**, 194307.
- Zhang, X., D. Sun, Y. Li, G. H. Lee, X. Cui, D. Chenet, Y. You, T. F. Heinz, and J. C. Hone, 2015, *ACS Appl. Mater. Interfaces* **7**, 25923.
- Zhang, Y., Y. Yan, J. Guo, T. Lu, J. Liu, J. Zhou, and X. Xu, 2020, *ES Energy Environ.* **8**, 42.
- Zhang, Z., Y. Guo, M. Bescond, J. Chen, M. Nomura, and S. Volz, 2021a, *APL Mater.* **9**, 081102.
- Zhang, Z., Y. Guo, M. Bescond, J. Chen, M. Nomura, and S. Volz, 2021b, *Phys. Rev. B* **103**, 184307.
- Zhang, Z., Y. Guo, M. Bescond, J. Chen, M. Nomura, and S. Volz, 2021c, *J. Appl. Phys.* **130**, 084301.
- Zhang, Z., S. Hu, T. Nakayama, J. Chen, and B. Li, 2018, *Carbon* **139**, 289.
- Zhang, Z., S. Hu, Q. Xi, T. Nakayama, S. Volz, J. Chen, and B. Li, 2020, *Phys. Rev. B* **101**, 081402.
- Zhang, Z., Y. Ouyang, J. Chen, and S. Volz, 2020, *Chin. Phys. B* **29**, 124402.
- Zhang, Z., Y. Ouyang, Y. Cheng, J. Chen, N. Li, and G. Zhang, 2020, *Phys. Rep.* **860**, 1.
- Zhao, H., and J. B. Freund, 2005, *J. Appl. Phys.* **97**, 024903.
- Zhao, H., and J. B. Freund, 2009, *J. Appl. Phys.* **105**, 013515.
- Zhao, Y., M. L. Fitzgerald, Y. Tao, Z. Pan, G. Sauti, D. Xu, Y. Q. Xu, and D. Li, 2020, *Nano Lett.* **20**, 7389.
- Zhao, Y., X. Liu, A. Rath, J. Wu, B. Li, W. Zhou, G. Xie, G. Zhang, and J. T. L. Thong, 2020, *Sci. Rep.* **10**, 821.
- Zhao, Y., *et al.*, 2018, *Adv. Mater.* **30**, 1804928.
- Zhong, H. L., and J. R. Lukes, 2006, *Phys. Rev. B* **74**, 125403.
- Zhong, J., Q. Xi, Z. Wang, T. Nakayama, X. Li, J. Liu, and J. Zhou, 2021, *J. Appl. Phys.* **129**, 195102.
- Zhou, H., and G. Zhang, 2018, *Chin. Phys. B* **27**, 034401.
- Zhou, X., M. V. Tokina, J. A. Tomko, J. L. Braun, P. E. Hopkins, and O. V. Prezhdo, 2019, *J. Chem. Phys.* **150**, 184701.
- Zhou, X. W., R. E. Jones, C. J. Kimmer, J. C. Duda, and P. E. Hopkins, 2013, *Phys. Rev. B* **87**, 094303.
- Zhou, Y., and M. Hu, 2015, *Phys. Rev. B* **92**, 195205.
- Zhou, Y., and M. Hu, 2017, *Phys. Rev. B* **95**, 115313.
- Zhou, Y., X. Zhang, and M. Hu, 2016, *Nanoscale* **8**, 1994.
- Zhu, Y., *et al.*, 2019, *Nat. Commun.* **10**, 2067.